UNIVERSITY OF AMSTERDAM

UvA-DARE (Digital Academic Repository)

Neutron stars and the dense matter equation of state

Chatziioannou, Katerina; Cromartie, H. Thankful; Gandolfi, Stefano; Tews, Ingo; Radice, David; Steiner, Andrew W.; Watts, Anna L.

DOI
10.1103/ymsq-cfcw

Publication date
2025

Document Version
Final published version

Published in
Reviews of Modern Physics

License
Article 25fa Dutch Copyright Act (https://www.openaccess.nl/en/policies/open-access-in-dutch-copyright-law-taverne-amendment)

Link to publication

Citation for published version (APA):
Chatziioannou, K., Cromartie, H. T., Gandolfi, S., Tews, I., Radice, D., Steiner, A. W., & Watts, A. L. (2025). Neutron stars and the dense matter equation of state. *Reviews of Modern Physics*, *97*(4), Article 045007. https://doi.org/10.1103/ymsq-cfcw

General rights
It is not permitted to download or to forward/distribute the text or part of it without the consent of the author(s) and/or copyright holder(s), other than for strictly personal, individual use, unless the work is under an open content license (like Creative Commons).

Disclaimer/Complaints regulations
If you believe that digital publication of certain material infringes any of your rights or (privacy) interests, please let the Library know, stating your reasons. In case of a legitimate complaint, the Library will make the material inaccessible and/or remove it from the website. Please Ask the Library: https://uba.uva.nl/en/contact, or a letter to: Library of the University of Amsterdam, Secretariat, P.O. Box 19185, 1000 GD Amsterdam, The Netherlands. You will be contacted as soon as possible.

UvA-DARE is a service provided by the library of the University of Amsterdam (https://dare.uva.nl)

Download date:11 11月 2026

Neutron stars and the dense matter equation of state

Katerina Chatziioannou[*]

Department of Physics, California Institute of Technology, Pasadena, California 91125, USA

H. Thankful Cromartie[†]

National Research Council Postdoctoral Associate, National Academy of Sciences, Washington, DC 20001, USA
and Resident, Naval Research Laboratory, Washington, DC 20375, USA

Stefano Gandolfi[‡] and Ingo Tews[§]

Theoretical Division, Los Alamos National Laboratory, Los Alamos, New Mexico 87545, USA

David Radice[‖]

Institute for Gravitation and the Cosmos, Pennsylvania State University, University Park, Pennsylvania 16802, USA,
Department of Physics, Pennsylvania State University, University Park, Pennsylvania 16802, USA,
and Department of Astronomy and Astrophysics, Pennsylvania State University, University Park, Pennsylvania 16802, USA

Andrew W. Steiner[¶]

Department of Physics and Astronomy, University of Tennessee at Knoxville
and Physics Division, Oak Ridge National Laboratory, Oak Ridge, Tennessee 37831, USA

Anna L. Watts[**]

Anton Pannekoek Institute for Astronomy, University of Amsterdam, Science Park 904, 1090GE Amsterdam, The Netherlands

(published 24 December 2025)

The past two decades have witnessed tremendous progress in understanding the properties of neutron stars, their maximum mass and radii, and the properties of the dense matter in their cores, made possible by electromagnetic observations of neutron stars and the detection of gravitational waves from their mergers. These observations have provided novel constraints on neutron-star structure that are intimately related to the properties of dense neutron-rich matter described by the nuclear equation of state. Nevertheless, constraining the equation of state over the wide range of densities probed by astrophysical observations is still challenging, as the physics involved is broad and the system spans many orders of magnitude in density. Theoretical approaches to calculate and model the neutron-star equation of state in various regimes of densities are reviewed, and the related consequent properties of neutron stars are discussed. How the equation of state at low densities can be calculated from nuclear interactions that are constrained and benchmarked by nuclear experiments is described. Neutron-star observations, with a particular emphasis on information provided by gravitational-wave signals and electromagnetic observations, are reviewed. Finally, future challenges and opportunities in the field are discussed.

DOI: 10.1103/ymsq-cfcw

[*]Contact author: kchatziioannou@caltech.edu
[†]Contact author: thankful.cromartie@nanograv.org
[‡]Contact author: stefano@lanl.gov
[§]Contact author: itews@lanl.gov
[‖]Contact author: david.radice@psu.edu
[¶]Contact author: awsteiner0@protonmail.com
[**]Contact author: A.L.Watts@uva.nl

CONTENTS

I. Introduction 2
II. History of Neutron-Star Observations 3
III. The Equation of State from Nuclear Theory 4
A. Gross properties of the equation of state at nuclear densities 4
B. Low-density neutron matter and the unitary Fermi gas 5
C. Crust equation of state 6
D. Microscopic theory for the equation of state at nuclear densities 8

 © 2025 American Physical Society

1. Nucleon-nucleon and three-body interactions 8
2. Microscopic many-body calculations 10
E. The equation of state in β equilibrium 13
F. Matter at high densities: Quarks, hyperons, pions, and other degrees of freedom 14
G. Matter at high densities: Phenomenological models 15
IV. Constraints from Nuclear Experiments 16
A. Nuclear structure experiments 16
B. Neutron-skin thickness 16
C. Heavy-ion collisions 17
V. From Microphysics to Neutron-Star Structure 17
A. The Tolman-Oppenheimer-Volkoff equation 17
B. Tidal deformability 18
VI. Compact Binary Mergers Involving Neutron Stars 20
A. Compact binary inspirals 20
B. Mass observations 22
C. Late inspiral and tidal deformation 23
D. Merger and postmerger 26
E. The outcome of neutron-star binary mergers 26
1. Prompt black hole formation 28
2. Delayed collapse: Multimessenger constraints 29
3. Long-lived merger remnants 30
F. Neutron-star–black hole binaries 31
VII. Electromagnetic Observations 31
A. Radiation processes 32
B. Radio observations: Masses 32
C. X-ray spectroscopy 34
D. X-ray pulse-profile modeling 35
VIII. Future Theoretical and Experimental and Observational Challenges and Opportunities 38
Acknowledgments 40
References 40

I. INTRODUCTION

Neutron stars are the most compact material objects in the Universe. They represent unique systems of matter under extreme conditions of pressure and density, exhibiting a variety of interesting properties that can be inferred from astronomical observations. The existence of neutron stars was predicted soon after the discovery of the neutron. In 1934 Baade and Zwicky stated, "With all reserve we advance the view that a super-nova represents the transition of an ordinary star into a neutron star, consisting mainly of neutrons" (Baade and Zwicky, 1934). Neutron stars have typical radii around 10 km but masses that can reach 2 times the mass of the Sun. These extreme conditions lead to unique properties of neutron stars: densities in the centers of neutron stars can reach up to 6 to 8 times the nuclear saturation density (Koehn *et al.*, 2024), which is the density in the center of a heavy atomic nucleus. While densities of a few times the nuclear saturation density can be achieved in collisions with heavy nuclei in experiments on Earth, the conditions are much different from those in neutron stars because matter is hot and not neutron rich. Neutron stars, however, are neutron rich and can typically be treated as objects at zero temperature. Theoretical predictions of the properties of this matter can therefore be tested only with astronomical observations.

Despite their name, neutron stars are not composed of neutrons only but instead have a layered and physics-rich structure (Lattimer and Prakash, 2001, 2004; Oertel *et al.*, 2017; Burgio *et al.*, 2021). The crust (the outer 1 km) primarily contains neutron-rich nuclei arranged on a lattice, surrounded by a sea of neutrons. From the outer to the inner part of the crust, the properties of these nuclei change drastically. At low densities their properties resemble ordinary matter, but with increasing density the nuclei become increasingly neutron rich. In principle, these nuclei could be realized in terrestrial experiments, but such neutron-rich nuclei are highly unstable, and their half-lives are short. When densities are sufficiently high, neutrons begin to drip from these nuclei, forming a "sea" of neutrons.

The sea of neutrons that surrounds the nuclei in the inner crust may be in a fermionic superfluid phase (Sedrakian and Clark, 2019; Andersson, 2021) that alters the specific heat and the neutrino emission of the star and plays a crucial role in the star cooling. The superfluid phase is also relevant to sudden observed spin jumps, called glitches, that are likely related to the angular momentum stored in the inner crust. Fermionic superfluids have been studied for decades, but the properties of neutron matter in these regimes are unique. The strong pairing consists of strongly correlated (but unbound) pairs of neutrons that interact at large distances. The existence of this fermionic superfluidity was confirmed by analyzing neutron-star cooling observations (Brown and Cumming, 2009; Page *et al.*, 2011).

Theoretical calculations showed that at even higher densities the extremely neutron-rich nuclei undergo a number of transitions, manifesting in peculiar shapes and deformations in phases known as nuclear pasta (Watanabe, Iida, and Sato, 2000). In these phases protons and neutrons organize themselves in "pasta" geometries such as spaghetti (rods) and lasagna (slabs). Eventually, the system becomes increasingly neutron rich until the homogeneous matter phase, the outer core, is reached.

The outer core of neutron stars consists of matter composed of nucleons, electrons, and muons. Most nucleons are neutrons with a small fraction of protons, and proton fractions are of the order of 5% but grow again with density. The degenerate neutron-rich fluid provides pressure against the gravitational pull and keeps the star from collapsing to a black hole. This pressure is the degeneracy pressure due to the Pauli exclusion principle and low temperatures and is enhanced by repulsive interactions among the nucleons. This region is of particular concern in nuclear physics, as the underlying interactions between nucleons are of great interest and can be tested by comparing predicted properties of dense matter with data from terrestrial experiments and astrophysical observations of neutron stars. In this regime the nucleons are strongly interacting, and sophisticated models describing the correlations among two and three nucleons are necessary for accurate descriptions of not only dense matter but also atomic nuclei.

The inner core of neutron stars is the least understood part of the neutron star. Densities reach their maximum, up to multiple times the saturation density, and it is unclear what degrees of freedom describe this region. There are different hypothetical models. There could be charged mesons, such as pions or kaons, that eventually form a Bose condensate. Other heavier baryons with strangeness, called hyperons, might

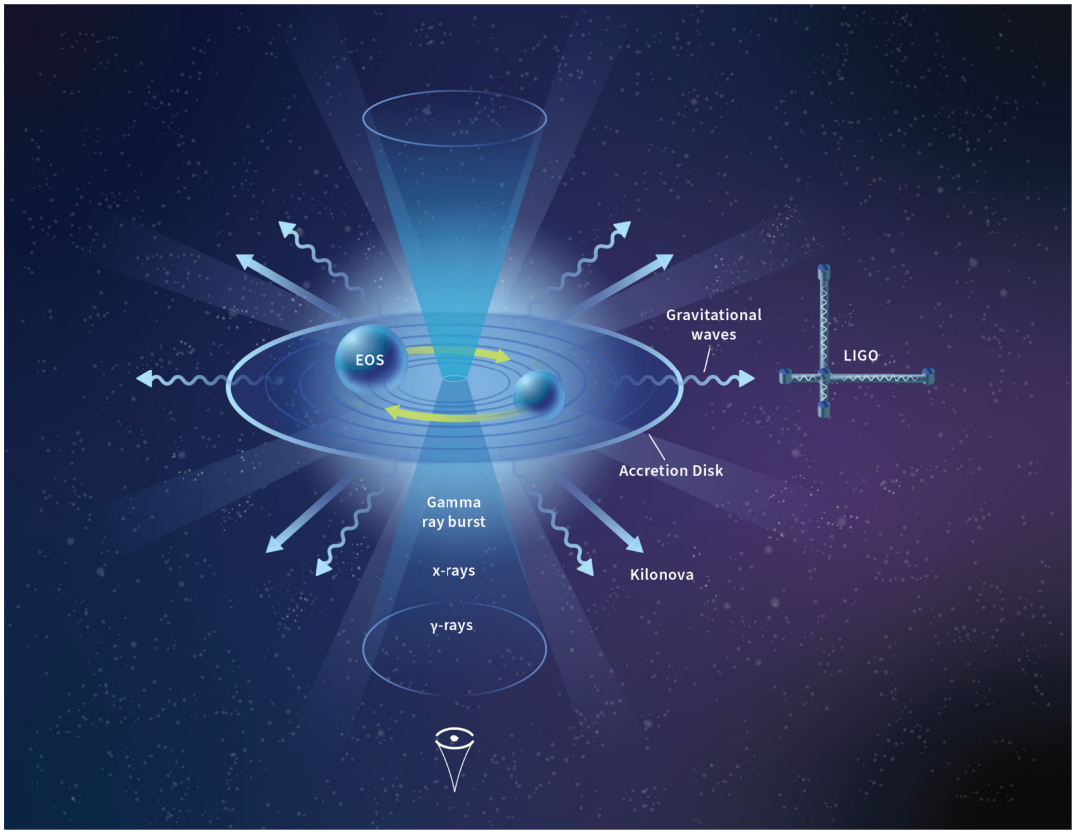

FIG. 1. Schematic of the merger of two neutron stars with the corresponding emissions that can be observed on Earth. Courtesy of P. Ziomek.

form from nucleons through weak processes (Chatterjee and Vidaña, 2016; Tolos and Fabbietti, 2020). Finally, at higher densities hadrons might not be relevant degrees of freedom and quark matter, in which quarks are deconfined, might appear (Alford *et al.*, 2008; Fukushima and Sasaki, 2013; Baym *et al.*, 2018; McLerran and Reddy, 2019; Annala *et al.*, 2020).

The review is structured as follows. In Sec. II we give a history of neutron-star observations. In Sec. III we discuss how to obtain the equation of state (EOS) from nuclear theory. We review general properties of the EOS here, as well as the microscopic theory necessary to describe the EOS. We also discuss possible degrees of freedom describing matter at the highest densities in neutron stars. In Sec. IV we review different experiments that place constraints on the EOS. In Sec. V we explain how to get from the EOS microphysics to neutron-star observables, then discuss how to describe mergers with neutron stars in Sec. VI. In particular, we discuss mass and tidal information that can be extracted from these observations. In Sec. VII we discuss electromagnetic observations of neutron stars, and we end the review in Sec. VIII by considering future opportunities.

II. HISTORY OF NEUTRON-STAR OBSERVATIONS

Neutron stars were discovered in 1967 by Jocelyn Bell Burnell in the form of radio pulsars (Hewish *et al.*, 1968), which still form the majority of the observed neutron-star population (Manchester *et al.*, 2005; Lorimer, 2008).[1] Many rotation-powered pulsars (where emission is powered primarily by the loss of rotational energy) also emit in other wave bands, though most observations are confined to only the lowest (radio $\lesssim$3 GHz) and highest (x-rays and gamma rays) electromagnetic frequencies (Smith *et al.*, 2023). The timing of rotation-powered pulsars in binaries enables precise inferences of neutron-star mass that can be used to constrain the dense matter EOS, with the tightest constraints coming from the measurement of pulsars with masses exceeding $2M_{\odot}$, the first direct measurement of which was reported by Demorest *et al.* (2010); see Sec. VII.B.

The first x-ray satellites led to the discovery of accreting neutron stars in the form of accreting pulsars (Giacconi *et al.*, 1971) and thermonuclear bursters (Belian, Conner, and Evans, 1976; Grindlay *et al.*, 1976). We now know of a few hundred accreting neutron stars in both low- and high-mass x-ray binaries (Bildsten *et al.*, 1997; Galloway *et al.*, 2020; Patruno and Watts, 2021). X-ray observations via ROSAT, Chandra, and XMM had sufficient sensitivity to enable the study of cooling of young isolated neutron stars and accreting neutron stars in quiescence (Walter, Wolk, and Neuhäuser, 1996; Brown, Bildsten, and Rutledge, 1998). Spectral modeling of all of these sources is now used to infer masses and radii; see Sec. VII.C. Meanwhile, the discovery of thermal x-ray

[1]See http://www.atnf.csiro.au/research/pulsar/psrcat.

pulsations from rotation-powered pulsars would eventually open up new techniques for constraining mass and radius (Becker and Trümper, 1993; Pavlov and Zavlin, 1997); see Sec. VII.D.

Compact object mergers involving neutron stars can be detected through gravitational radiation; see Sec. VI. The first indirect detection of gravitational waves was achieved through the decay of the binary pulsar orbit (Hulse and Taylor, 1975). Terrestrial interferometric detectors (Pitkin *et al.*, 2011) enabled the first direct detection of the effect of gravitational waves on Earth in 2016 with the detection of the merger of a black hole binary (Abbott *et al.*, 2016). The signal from the first neutron-star binary merger, GW170817, was detected in 2017 (Abbott *et al.*, 2017a), not only in gravitational waves but also with electromagnetic radiation across the spectrum (Abbott *et al.*, 2017d, 2017e). A second likely neutron-star binary, GW190425, was not accompanied by detection of electromagnetic radiation, likely because of its high mass (Abbott *et al.*, 2020a). The set was completed in 2020 with the detection of mixed neutron-star–black hole binaries (Abbott *et al.*, 2021b). See Fig. 1 for a schematic of the merger of two neutron stars with the corresponding emissions that can be observed on Earth.

III. THE EQUATION OF STATE FROM NUCLEAR THEORY

In this section we give an overview of the nuclear EOS in terms of its general properties, such as the symmetry energy and its slope (Lattimer and Lim, 2013). We discuss other macroscopic properties that are constrained by nuclear experiments. We then give an overview of the various density regimes explored in neutron stars. We discuss low-density constraints on the EOS, the complicated "crustal" regime (including a region where deformed nuclei are surrounded by a superfluid neutron gas), and the EOS at higher densities, where heavier particles like hyperons or resonances might appear. In particular, we focus on a discussion of theoretical approaches to calculate the EOS from microscopic nuclear interactions that include two- and three-body potentials that also reproduce several properties of nuclei. Finally, we discuss additional degrees of freedom, such as strangeness, and their impact on the EOS, including the appearance of phase transitions.

A. Gross properties of the equation of state at nuclear densities

As a first approximation, matter in the core of neutron stars from about one-half up to about twice the nuclear saturation density can be modeled by considering nuclear matter, i.e., an infinite system of matter formed only by neutrons and protons. Properties of symmetric nuclear matter near saturation can be extracted from experiments. On the contrary, neutron-rich matter and matter at densities higher than saturation are difficult to directly constrain from data because those systems cannot be realized in terrestrial experiments. Furthermore, properties of nuclear matter, such as its EOS, can be extracted from theoretical calculations. Here we begin our discussion of the EOS by introducing a generic parametrization that provides a good approximation of various microscopic models and allows us to define the basic physical quantities of interest.

We define the number density of neutrons as n_n, the number density of protons as n_p, the total baryon density $n = n_n + n_p$, and the asymmetry $\beta \equiv (n_n - n_p)/n$. A useful expansion of the EOS is given in terms of the asymmetry,

$$\frac{E}{A}(n,\beta) = \frac{E}{A}(n,0) + S(n)\beta^2 + \cdots, \tag{1}$$

where $E(n,0)/N$ is the energy per nucleon or particle of symmetric nuclear matter, A is the total number of nucleons, and $S(n)$ is called the nuclear symmetry energy. This expansion works well near the saturation density but can fail at higher densities (Steiner, 2006; Wellenhofer, Holt, and Kaiser, 2015; Somasundaram *et al.*, 2021). From this general definition, one can compute the energy density of nuclear matter,

$$\varepsilon(n,\beta) = n\frac{E}{A}(n,\beta), \tag{2}$$

the neutron and proton chemical potentials,

$$\mu_i = \left.\frac{\partial \varepsilon}{\partial n_i}\right|_{n_j}, \tag{3}$$

where i and j denote either neutrons or protons and the pressure

$$P = n^2\frac{\partial(E/A)}{\partial n} = -\varepsilon + \mu_n n_n + \mu_p n_p. \tag{4}$$

The expressions for the energy density and the chemical potentials do not contain the terms for the rest-mass energy density, which we define as $m_n n_n + m_p n_p$, and m_n and m_p are the neutron and proton masses. An important density in nuclear systems is the nuclear saturation density, $n_0 \approx 0.16$ fm^{-3}, which is related to the size of the atomic nuclei. The nuclear saturation density corresponds to a mass density of $\approx 2.7 \times 10^{14}$ g/cm^3. The general expressions for the EOS can be expanded around $\chi = \beta = 0$,

$$\frac{E}{A}(n,\beta) \approx -B + \frac{K}{2}\chi^2 + \left(S + L\chi + \frac{K_{\rm sym}}{2}\chi^2\right)\beta^2, \tag{5}$$

where $\chi = (n - n_0)/3n_0$. This form uses the fact that symmetric nuclear matter saturates at density n_0, implying that the pressure vanishes, $P(n_0) = 0$. More sophisticated EOS also include higher-order terms proportional to χ^3 and β^4 and beyond (Margueron, Hoffmann Casali, and Gulminelli, 2018). Just below the saturation density, isospin-symmetric matter with $n_n = n_p$ ($\beta = 0$) is unstable, as the pressure is negative. This is the mathematical manifestation of the physical reality that nuclear matter prefers to separate into two phases at low density: a dense phase, given by the atomic nuclei, and the vacuum. Such nonhomogeneous matter appears in the crust of neutron stars and is described separately later. Most many-body methods permit one to calculate the EOS of homogeneous matter (in a model-dependent way), which can be described approximately by the aforementioned form, without including the degrees of freedom associated with clustering.

The aforementioned β and χ expansions motivate the definition of several quantities. The saturation density n_0 is the density at which the pressure in symmetric matter ($\beta = 0$) vanishes. The binding energy B of symmetric nuclear matter, $B \approx 16$ MeV, is the energy per particle of symmetric nuclear matter at saturation density n_0, which is intimately connected to the binding energy of nuclei. The nuclear incompressibility (also called the compressibility) is defined for $\beta = 0$ as

$$K = \left.\frac{\partial^2(E/A)}{\partial\chi^2}\right|_{n_0,\beta=0} \tag{6}$$

$$= 9n_0^2\left.\frac{\partial^2(E/A)}{\partial n^2}\right|_{n_0,\beta=0} = 9\left.\frac{\partial P}{\partial n}\right|_{n_0,\beta=0}. \tag{7}$$

The incompressibility can be experimentally constrained by measuring the peak energy of the giant monopole resonance in nuclei (Youngblood, Clark, and Lui, 1999) or from heavy-ion collisions (Le Fèvre *et al.*, 2016). Recent models give $K = 230 \pm 20$ MeV (Huth, Wellenhofer, and Schwenk, 2021).

The symmetry energy $S(n)$ is an especially important quantity. At saturation the parameter $S = S(n_0)$ is related to several nuclear properties. Furthermore, the symmetry energy determines the pressure of neutron matter, and hence it plays an important role for the structure of neutron stars. The symmetry energy $S(n)$ can be defined in two ways. The first definition is given by the difference between the EOS of pure neutron matter and the symmetric nuclear matter,

$$S(n) = \frac{E}{A}(n,1) - \frac{E}{A}(n,0). \tag{8}$$

The second definition is via a second derivative of the energy per particle with respect to the asymmetry,

$$S_2(n) = \frac{1}{2}\left.\frac{\partial^2(E/A)}{\partial\beta^2}\right|_{n_0}. \tag{9}$$

If terms beyond β^2 in Eq. (1) are neglected, the two definitions agree. As this approximation is usually good, the two definitions lead to comparable results. From the symmetry energy, the slope parameter L can be defined by

$$L(n) = 3n_0\left.\frac{\partial S}{\partial n}\right|_{n_0} = \frac{3}{n_0}P(n_0,\beta=1). \tag{10}$$

Note that Eq. (10) directly relates the value of L to the pressure of pure neutron matter at saturation density. The symmetry energy is also related to the neutron and proton chemical potentials. Using

$$\left(\frac{\partial\varepsilon}{\partial\beta}\right)_n = \frac{\partial\varepsilon}{\partial n_n}\left(\frac{\partial n_n}{\partial\beta}\right)_n + \frac{\partial\varepsilon}{\partial n_p}\left(\frac{\partial n_p}{\partial\beta}\right)_n = \frac{n}{2}(\mu_n - \mu_p), \tag{11}$$

we obtain

$$S(n) = \frac{1}{4}\frac{\partial}{\partial\beta}(\mu_n - \mu_p). \tag{12}$$

Similarly, the slope of the symmetry energy can be rewritten as

$$L(n) = \frac{3n}{4}\frac{\partial}{\partial n}\frac{\partial}{\partial\beta}(\mu_n - \mu_p). \tag{13}$$

Alternatively, using

$$\left(\frac{\partial\varepsilon}{\partial n}\right)_\beta = \frac{\partial\varepsilon}{\partial n_n}\left(\frac{\partial n_n}{\partial n}\right)_\beta + \frac{\partial\varepsilon}{\partial n_p}\left(\frac{\partial n_p}{\partial n}\right)_\beta = \frac{1}{2}(\mu_n + \mu_p), \tag{14}$$

L can be rewritten as

$$L(n,\beta) = 3n\left[\frac{-1}{2n^2}\frac{\partial^2\varepsilon}{\partial\beta^2} + \frac{1}{4n}\frac{\partial^2}{\partial\beta^2}(\mu_n + \mu_p)\right]$$
$$= \frac{3}{4}\frac{\partial^2}{\partial\beta^2}(\mu_n + \mu_p) - 3S(n). \tag{15}$$

Reasonable ranges for S, L, and K are $29\ \text{MeV} < S < 36\ \text{MeV}$, $30\ \text{MeV} < L < 70\ \text{MeV}$, and $220\ \text{MeV} < L < 260\ \text{MeV}$, respectively (Steiner *et al.*, 2015; Huth, Wellenhofer, and Schwenk, 2021); see Steiner and Gandolfi (2012). Properties of infinite nuclear and neutron matter cannot be directly measured, but several properties, such as the saturation density, the incompressibility, and the symmetry energy, are related to nuclear properties that can be measured.

B. Low-density neutron matter and the unitary Fermi gas

At very low densities, i.e., $n \lesssim 10^{-2}n_0$, properties of homogeneous neutron matter are similar to those of ultracold Fermi gases of atomic nuclei, despite the differences between those two systems, i.e., the much different length scales involved, and the details regarding their interparticle interaction of atoms with respect to neutrons (Gandolfi, Gezerlis, and Carlson, 2015). This similarity arises because the neutron-neutron interaction is peculiar: its scattering length is large and the effective range is small. Under these conditions several properties of the system are universal, meaning that they do not depend on the explicit details of the interactions among the particles. Thus, systems that are much different in nature have similar properties. The great advantage of using ultracold atomic gases is that they can be experimentally controlled precisely and then used to "simulate" neutron matter. This provides valuable information because the latter cannot be directly realized and/or observed in experiments.

These systems are unique because they exhibit the largest superfluid pairing gap in fermionic systems. Other examples of fermionic superfluids include atomic liquid ^{3}He and high-T_C superconductors, and their pairing gap is of the order of $10^{-4}E_{\rm FG}$–$10^{-2}E_{\rm FG}$, where $E_{\rm FG}$ is the Fermi gas energy. Ultracold atomic gases and low-density neutron matter have a pairing gap of the order of $E_{\rm FG}$, and this aspect has dramatic consequences on their dynamical properties. The superfluid gap of neutron matter has important consequences for the cooling and other properties of neutron stars (Page *et al.*, 2011; Potekhin, Pons, and Page, 2015).

Ultracold Fermi gases have been extensively studied both experimentally and theoretically; for a review, see Giorgini,

Pitaevskii, and Stringari (2008). Of particular relevance for understanding neutron matter is a gas made by two species of same-mass fermions in two states: one with spin-up and one with spin-down. Because of the universality of these systems, with properties independent of the interactions, one can conveniently describe these systems via a model where particles interact in the S wave, i.e., with $l = 0$, where l is the relative angular momentum, and the physics of the many-body system is mainly governed by the two-body scattering length a. For spin unpolarized systems, a pair of atoms can be in the spin-singlet and spin-triplet states, and the S wave is the dominant channel at low density. Since the effective range r_e of the interaction is small compared to the interparticle separation r_0, the Fermi momentum k_F of the system is the only relevant scale; i.e., the system is in a dilute regime where $r_e \ll r_0 \ll a$. Then, in the dilute limit, the system's properties are determined only by the natural (unitless) quantity ak_F. The energy and other quantities, like the pressure and temperature, can be conveniently measured in units of k_F or of the Fermi gas energy $E_{\rm FG}$. Of particular interest is the extreme limit where $a \to \infty$ and $r_e \to 0$. This is called the unitary limit. In this case the energy is often indicated through the so-called Bertsch parameter, $\xi = E/E_{\rm FG}$, and its value is independent of the detail of the interaction between particles (Giorgini, Pitaevskii, and Stringari, 2008). The most accurate calculations give $\xi = 0.372(5)$ (Carlson *et al.*, 2011), which is in excellent agreement with the experimental value $\xi = 0.376(4)$ (Ku *et al.*, 2012).

In the weakly interacting limit of $ak_F \ll 1$, the EOS of ultracold Fermi gases can be described via the perturbative expansion (Lenz, 1929; Lee and Yang, 1957)

$$\frac{E}{E_{\rm FG}} = 1 + \frac{10}{9\pi} ak_F + \frac{4}{21\pi^2}(11 - 2\ln 2)(ak_F)^2 + \cdots. \quad (16)$$

When the strength of the interaction increases, the system becomes highly correlated, and nonperturbative methods have to be used to solve for the EOS. Among other techniques quantum Monte Carlo methods have been employed to investigate properties of these systems spanning the weakly to the strongly interacting regime (Carlson *et al.*, 2003, 2011; Bulgac, Drut, and Magierski, 2006; Forbes, Gandolfi, and Gezerlis, 2011; Gandolfi, Schmidt, and Carlson, 2011). For small and negative values of ak_F, the two-body system is unbound, the system is weakly interacting, and atoms in different spin states form Cooper (or BCS) pairs. This is the regime where these atomic gases resemble low-density neutron matter.

At very low momenta (densities), the neutron-neutron interaction is dominated by the S-wave component, and other partial waves are negligible; see Gandolfi, Gezerlis, and Carlson (2015). Given that the neutron-neutron effective range extracted from scattering data is $r_e \approx 2.7$ fm and the scattering length is $a \approx -18.5$ fm, there is a density regime where $r_e < r_0 < a$, and the properties of neutron matter can be compared to ultracold atomic Fermi gases. The energy of cold atoms as a function of ak_F has been used to extrapolate the EOS of neutron matter (Carlson, Gandolfi, and Gezerlis, 2012). In Fig. 2 we show the EOS of cold atoms (the solid blue line) compared to that of neutron matter (the red and green symbols). For cold atoms the interaction was short range, and the results were obtained in the limit of $r_e \to 0$ (Forbes, Gandolfi, and Gezerlis, 2012). The EOS of neutron matter has been calculated by considering the S-wave part of a realistic neutron-neutron interaction (the red symbols in Fig. 2) (Gezerlis and Carlson, 2008), and also by including the contribution of P waves, i.e., with $l = 1$ (the green symbols in Fig. 2) (Gezerlis and Carlson, 2010). As we see, the properties of homogeneous neutron matter can be well extrapolated from cold atom calculations in the dilute regime ($|ak_F|$ is not too large). This has been important for benchmarking theoretical calculations with experimental constraints. A similar benchmark was used for the superfluid pairing gap, and theoretical calculations are in good agreement with experimental measurements (Carlson and Reddy, 2005).

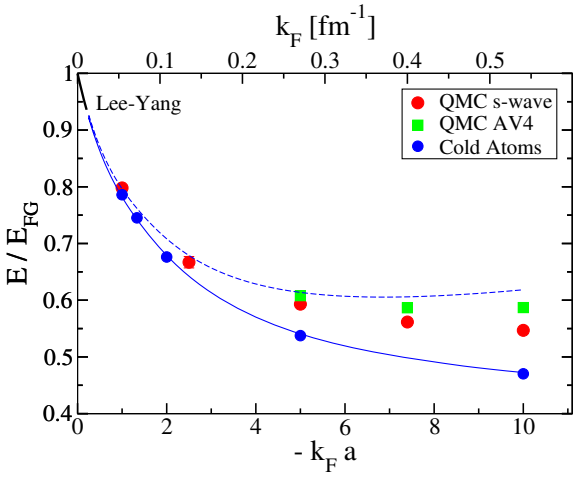

FIG. 2. The EOS of cold atoms compared to that of neutron matter. The solid blue line corresponds to cold atoms in the limit of the zero effective range, while the dashed line corresponds to an interaction with the same effective range of the neutron-neutron interaction. The red circles were obtained by considering the S-wave part of a realistic neutron-neutron interaction, and the green squares include the effect of the P-wave ($l = 1$) channel using the Argonne AV4′ interaction. From Gezerlis and Carlson, 2010, and Carlson, Gandolfi, and Gezerlis, 2012.

The EOS and the superfluid pairing gap have been calculated for realistic nuclear interactions in neutron matter. See Sedrakian and Clark (2019) for a review and Gandolfi *et al.* (2022) for some results.

C. Crust equation of state

The neutron-star crust is the outer region of the neutron star that lies between the "ocean" and the "core" and is composed of a Coulomb lattice of nuclei. The ocean is the region (from centimeters to hundreds of meters, depending on the temperature) at the surface that is sufficiently hot and tenuous to remain in a fluid phase because the ambient temperature is larger than the melting temperature of the crystal. (Note that in the review we also use the term atmosphere, which refers to the region where the temperature drops precipitously and sets the emergent x-ray spectrum. The precise ordering of these

regions depends on the neutron star's temperature and accretion state.) The ocean (Page *et al.*, 2014) does not contain sufficient mass to impact the global neutron-star structure ($0.01M_\odot$–$0.1M_\odot$, depending on the temperature). At the lowest densities, the crust is composed of atoms in a crystal and the electron wave functions are localized near their respective nuclei. At a mass density near $\rho \sim 6 \times 10^{-7}$ MeV/fm^3 (10^6 g/cm^3) the density becomes large enough that the electrons become degenerate and form a nearly uniform background. This region is referred to as the *outer crust*; see Oyamatsu and Iida (2007) and Roca-Maza and Piekarewicz (2008). In isolated neutron stars, it becomes energetically favorable for some of the neutrons to leave their nuclei at a mass density of $\rho \sim 0.2$ MeV/fm^3 (4×10^{11} g/cm^3). [This threshold density may increase by about a factor of 2 in accreting neutron stars (Steiner, 2012)]. This begins the *inner crust*, which survives up to a mass density of about $\rho \sim 60$ MeV/fm^3 (10^{14} g/cm^3), or about half the nuclear saturation density.

In cold ($T \ll 1$ MeV) isolated neutron stars that have achieved nuclear statistical equilibrium (matter in this state is sometimes referred to as cold catalyzed), the EOS is determined by the mass of the equilibrium nucleus, the electron EOS, and small corrections due to the Coulomb lattice. The temperature is small enough to render the electrons degenerate but not small enough to make the nuclei degenerate. The energy density of matter ε can thus be approximately written as a function of the baryon density n (in the case of $T = 0$), as

$$\varepsilon(n) = n_{(Z,N)} m_{(Z,N)} + \varepsilon(n_e) + \varepsilon_{\text{lattice}}, \tag{17}$$

where $n_{(Z,N)}$ is the number density and $m_{(Z,N)}$ is the total mass of the nucleus with proton number Z and neutron number N. The last quantity, $\varepsilon_{\text{lattice}}$, is the lattice binding energy associated with a one-component body-centered-cubic Coulomb lattice. (Note that the nucleon rest masses are sometimes not included in the EOS, but we choose to include them here because it simplifies the discussion of β equilibrium). The ideal-gas contribution to the energy per nucleon from the nondegenerate nuclei is small compared to the rest-mass contribution, so we include only the latter. By charge neutrality the electron density is fixed to $n_e = Z n_{(Z,N)}$. The equilibrium nucleus is determined by minimizing the energy density with respect to Z and N at any fixed baryon density, $n = (Z + N) n_{(Z,N)}$. Because the nuclear binding energy per nucleon is maximized near ^{56}Fe, this nucleus is expected to dominate the composition of the lowest densities in the outer crust in cold isolated neutron stars.

The neutron and proton number densities can be written as $n_n = N n_{(Z,N)}$ and $n_p = Z n_{(Z,N)}$, respectively. One can compute the neutron and proton chemical potentials, $\mu_i = (\partial\varepsilon)/(\partial n_i)$. As the density increases, the electron chemical potential rises more quickly than that of the nucleons because the nuclei are nondegenerate and the electrons are degenerate. This fact, when combined with the β-equilibrium condition, $\mu_n = \mu_p + \mu_e$ (see also the description of β equilibrium in Sec. III.E), means that nuclei must become more neutron rich as the density increases. At the largest densities in the outer crust, the relevant nuclei are near the neutron drip line. There is thus still a small uncertainty in the EOS owing to the experimental uncertainties in the nuclear masses at the highest densities in the outer crust near ^{118}Kr (which has $N = 82$). The uncertainty in the EOS in the outer crust for isolated neutron stars is not important for the global structure of the neutron star.

In accreting neutron stars, material in the outer crust is not necessarily in nuclear statistical equilibrium, and thus the EOS is also determined by the unknown nuclear composition. Stellar evolution suggests that most of the material accreted onto the neutron-star surface comes from the outer layers of white dwarfs or main-sequence stars. In either case this matter likely consists of light nuclei, from hydrogen to oxygen. This accreted matter can become unstable to a thermonuclear explosion, and this is the origin of x-ray bursts [triggered by unstable burning of hydrogen or helium and lasting 10–100 s; see the review by Galloway *et al.* (2020)] or superbursts [longer, rarer, and more energetic events triggered by the unstable burning of carbon; see the recent paper by Alizai *et al.* (2023). X-ray bursts and superbursts lead to the creation of nuclei up to the $A \sim 107$ region (Schatz *et al.*, 2001). Thus, the average nuclear mass number ranges from 1 near the surface to ~100 at the transition between the outer and inner crusts (Haensel and Zdunik, 2003). The ashes of these x-ray bursts are pushed to higher densities by subsequent accretion and then undergo a further set of nuclear reactions that lead to heating. This process is referred to as *deep crustal heating* (Brown, Bildsten, and Rutledge, 1998) As with isolated neutron stars, the EOS variation in the outer crust does not impact the global structure of the neutron star (Suleiman, Zdunik, and Haensel, 2024). However, it can be important for the interpretation and analysis of x-ray bursts and superbursts.

The neutron-star inner crust is one of the most complicated many-body quantum systems in the Universe. There are two basic types of physics input: (i) the EOS of low-density neutron matter (described in Sec. III.B) and (ii) the structure of neutron-rich nuclei beyond the neutron drip line. In addition, the competition between the Coulomb and nuclear surface energy leads to strongly deformed nuclear shapes, often called the *nuclear pasta* (Ravenhall, Pethick, and Wilson, 1983; Watanabe *et al.*, 2009; Schneider *et al.*, 2013; Caplan and Horowitz, 2017). Note that this deformation is often qualitatively different from the deformation experienced by laboratory nuclei, which is strongly connected to nuclear shell effects; see Mayer (1964). The nuclear pasta would exist in the neutron-star inner crust even if nuclear shell effects could be ignored. There is a measurable amount of mass in the inner crust, on the order of $0.1M_\odot$. Thus, the uncertainty in the EOS can potentially have an impact on the global neutron-star structure.

Theoretical models of the nuclei in the inner crust typically take one of two forms: either phenomenological models based on liquid drop (or droplet) models or mean-field Hartree (or Hartree-Fock) calculations [pioneered by Negele and Vautherin (1973)] (Bender, Heenen, and Reinhard, 2003). The uncertainties in the EOS of the inner crust thus originate in (i) our imperfect knowledge of the nucleon-nucleon interaction (Oyamatsu and Iida, 2007) and (ii) our imperfect

ability to perform quantum many-body calculations of nuclei. These nuclear structure calculations can be combined with the Wigner-Seitz (Wigner and Seitz, 1933) approximation for the Coulomb lattice to form a model of the inner crust. The basic idea is that each nucleus resides at the center of a nearly spherical volume [a "Wigner-Seitz (WS) cell"] and that these cells are then arranged in a lattice. The radius of a spherical WS cell is fixed by two constraints: (i) the constraint that the total electric charge inside the cell is zero and (ii) the constraint that all baryons exist in WS cells (i.e., there are no baryons "outside"). In an accreting star, where the crust may contain an ensemble of nuclear species at every density, each nuclear species has its own type of Wigner-Seitz cell with a distinct radius.

The Wigner-Seitz approximation breaks down at the highest densities in the crust because the nuclear size and the WS cell size are nearly equal. This means that the calculation of the Coulomb energy is nontrivial. Molecular dynamics methods have been used to tackle this issue (Horowitz, Perez-Garcia, and Piekarewicz, 2004), but a complete exploration of the crust with all of the concomitant uncertainties is not yet possible.

Finally, the neutrons that are outside nuclei are expected to be superfluid, with a pairing gap on the order of a MeV (Gandolfi, Gezerlis, and Carlson, 2015; Gandolfi *et al.*, 2022). Unlike in condensed matter systems, for example, low-temperature superconductors, where the lattice phonons are critical in order to provide an attractive interaction between the participating fermions, the long-range interaction between neutrons is attractive (coming from one-pion exchange). The neutron Cooper pairs at this density are likely to be arranged in a singlet configuration, where the spins of the neutrons are oppositely aligned.

The neutron-star crust is observable in several different ways [see the review by Caplan and Horowitz (2017)]: (i) it may impact the neutrino signal emitted from a core-collapse supernova that can be measured in a galactic supernova, (ii) the crust may be important for pulsar glitches, (iii) the crust may be observable in the cooling of transiently accreting neutron stars (Brown and Cumming, 2009), and (iv) the crust may impact the oscillations observed in magnetar flares (Sotani, Iida, and Oyamatsu, 2019).

Neutron-star mergers are also a potentially important source of information about the neutron-star crust. Low-mass neutron stars are not expected to merge as frequently as those near $1.4M_{\odot}$. However, the tidal deformability increases strongly with decreasing neutron-star mass. Even though low-mass mergers are rare, information about the tidal deformability is dominated by low-mass neutron stars (Kedia *et al.*, 2024). Low-mass neutron stars in turn have a more significant contribution from the neutron-star crust. This means that the accuracy of the crust equation of state is becoming relevant for future gravitational-wave (GW) observatories (Piekarewicz and Fattoyev, 2019; Suleiman *et al.*, 2021).

There are still significant uncertainties with regard to the nature of the inner crust and the nuclear pasta. The frontier is dominated by two different classes of calculations: (i) fully three-dimensional Hartree-Fock calculations of nuclei embedded in a sea of nucleons [pioneered by Newton and Stone (2009)] and (ii) molecular dynamics calculations of tens of thousands of nucleons with potential energies that approximate nuclear forces [pioneered by Horowitz, Perez-Garcia, and Piekarewicz (2004)]. A full accounting of the uncertainties from the nucleon-nucleon interaction and the approximation to the quantum many-body problem has not yet been performed.

D. Microscopic theory for the equation of state at nuclear densities

1. Nucleon-nucleon and three-body interactions

At densities $n \gtrsim 10^{-2} n_0$, neutron matter cannot be described by S-wave interactions only, and higher partial waves have to be included; see Fig. 2. In the figure we see the EOS of neutron matter obtained with S-wave interactions only and when perturbatively including P-wave contributions start to differ at higher densities.

The nucleon-nucleon interaction depends on spin, isospin, and relative angular momentum of the nucleons, and it is convenient to make an expansion in terms of partial waves. A large amount of empirical information about the nucleon-nucleon scattering problem has been accumulated. In 1993 the Nijmegen group analyzed all nucleon-nucleon scattering data below 350 MeV published in physics journals between 1955 and 1992 (Stoks *et al.*, 1993). Older nucleon-nucleon interaction models that fit the Nijmegen database with a $\chi^2/N_{\rm data} \sim 1$ are called *phenomenological* and accurately fit the experimental data. Examples of these interactions are the Nijmegen models (Nijm93, Nijm I, Nijm II, and Reid-93) (Stoks *et al.*, 1994), the Argonne models (Wiringa, Stoks, and Schiavilla, 1995; Wiringa and Pieper, 2002), and the charge-dependent–Bonn potential (Machleidt, 2001).

Although two-nucleon interactions can accurately describe nucleon-nucleon scattering data and the properties of the deuteron, they fail to describe the binding energies of nuclei with $A \geq 2$ (Pieper *et al.*, 2001); see Hammer, Nogga, and Schwenk (2013). Furthermore, several calculations suggest that by considering nuclear Hamiltonians that include only two-body interactions, the EOS of symmetric nuclear matter saturates at too high of a density with energy that is too low; see results for the Argonne AV18 interactions (Akmal, Pandharipande, and Ravenhall, 1998), older variational calculations (Pandharipande and Wiringa, 1979), Brueckner calculations (Day and Wiringa, 1985; Baldo *et al.*, 2012), and other recent calculations using Hamiltonians from chiral effective field theory (EFT) (Hebeler *et al.*, 2011; Carbone, Polls, and Rios, 2013). The missing ingredient in these calculations are three-nucleon interactions.

While nucleon-nucleon scattering data have been precisely measured, there are no experiments to constrain solely three-body interactions that reach similar accuracies. Typically, three-body interactions are constrained by fitting calculations to reproduce properties of light nuclei, i.e., binding energies, radii, or other matrix elements of tritium or helium nuclei. Phenomenological interactions, such as the Argonne AV18 and AV8′ potentials, have been combined with three-body interactions to describe properties of light nuclei. In particular, the Urbana IX (UIX) three-body interaction has been

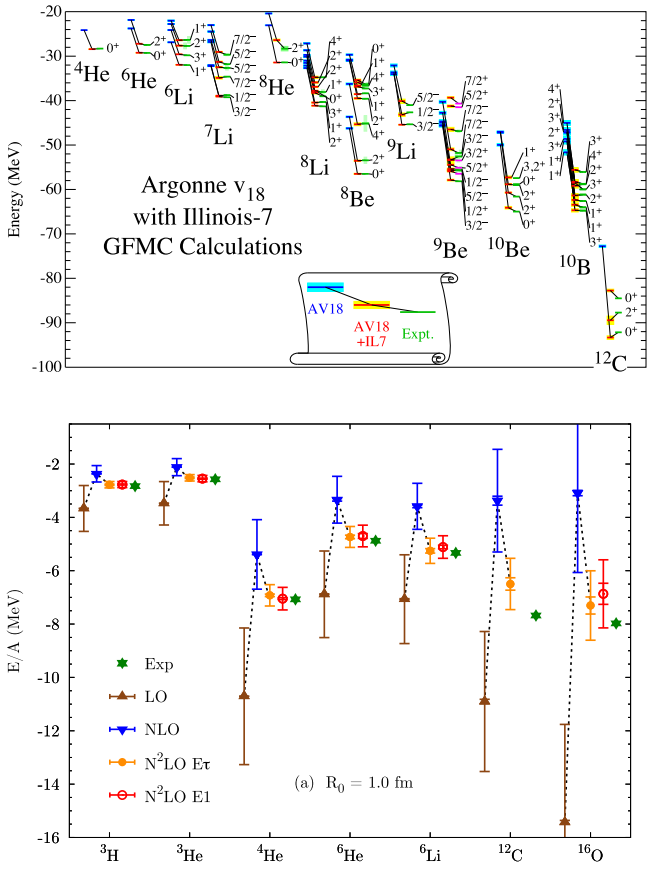

FIG. 3. Top panel: energy of several ground and excited states of light nuclei calculated using Argonne and Illinois Hamiltonians compared to experiments. For each level the green symbol at the right represents the experimental measurement, the blue symbol at the left is the result when including only two-body interactions in the nuclear Hamiltonian, and the red symbol in the middle is the prediction when three-body interactions are included. From Carlson *et al.*, 2015. Bottom panel: ground-state energy of selected nuclei obtained with chiral EFT Hamiltonians with a cutoff of $R_0 = 1.0$. From Lonardoni, Gandolfi *et al.*, 2018.

constrained to reproduce the saturation of nuclear matter and the ground state of ^{4}He (Pudliner *et al.*, 1995). However, the UIX slightly underbinds light nuclei (Pudliner *et al.*, 1997), and the Illinois models of three-nucleon interactions were later constructed to reproduce better properties of *p*-shell nuclei (Pieper *et al.*, 2001). They give an excellent description of several properties of light nuclei, including ground and excited states, matrix elements, scattering, and response functions (Carlson *et al.*, 2015). As an example, we show in the top panel of Fig. 3 the energy spectrum of several ground and excited states of nuclei up to ^{12}C. In the figure the Argonne AV18 two-body interaction and the Illinois 7 three-body interaction were used, but similar results have been obtained using different Hamiltonians. Predictions including only two-body interactions systematically underbind all the nuclei, while the inclusion of three-body potentials add the additional repulsion necessary for agreement with the experimental data.

Several calculations of the EOS of homogeneous nuclear and neutron matter using the UIX three-nucleon interaction have been performed. The corresponding EOS predicted the existence of $2M_\odot$ neutron stars (see Sec. VI.B) well before their discovery (Wiringa, Fiks, and Fabrocini, 1988; Akmal, Pandharipande, and Ravenhall, 1998). In contrast, even though the Illinois three-nucleon interactions accurately describe properties of nuclei, they produce soft EOSs of neutron-rich matter that do not reproduce even qualitatively the observed maximum mass of neutron stars (Sarsa *et al.*, 2003; Maris *et al.*, 2013).

The aforementioned phenomenological approaches do not provide a systematic scheme of improving two-nucleon interactions, and they also do not provide a means to derive consistent three-nucleon interactions. A solution to these shortcomings was provided by the modern approach to nuclear interactions within the framework of chiral EFT (Epelbaum, Hammer, and Meißner, 2009; Machleidt and Entem, 2011). In chiral EFT the interactions between nucleons and pions are expanded in powers of momenta Q over a breakdown scale Λ_b and Q/Λ_b. Here Q are the typical momenta of nucleons of the order of the pion mass, 140 MeV, and Λ_b is the breakdown scale, i.e., the scale where the chiral EFT expansion is expected to break down. The breakdown scale has been estimated to be of the order of 500–600 MeV (Drischler *et al.*, 2020). The different interaction terms are then systematically organized according to a power-counting scheme that determines which terms appear at leading order, next-to-leading order, etc. The most common power-counting scheme was introduced by Weinberg (1990, 1991) and is based on naive dimensional analysis, but alternative power-counting schemes have been proposed; see Kaplan, Savage, and Wise (1998a, 1998b) and Long and Yang (2012). One great advantage of the chiral EFT framework is that interactions can be systematically improved. Another advantage is that all the couplings between nucleons (or Δ degrees of freedom) and pions are fully determined by pion-nucleon scattering data (Hoferichter *et al.*, 2016). The parameters associated with nucleon contact terms, which encode missing high-momentum physics, are obtained by fitting to nucleon-nucleon scattering data. The separation into long-range parts of nuclear interactions, described by pion physics, and short-range parts, described by contact interactions, depends on the so-called regulator. The regulator is a function that multiplies the Hamiltonian to remove divergencies that appear when the quantum many-body problems are solved. For example, the one-pion exchange diverges when the two-particle separation r goes to 0. The regulator cuts off this divergence and, as a consequence, the short-range contact terms then absorb part of this physics. In coordinate space it defines at which r the transition between long- and short-range physics happens, and in coordinate space it determines a corresponding momentum scale. The scale that determines where this cut happens is called the cutoff. For a low cutoff, interactions are called *soft* and do not probe strong high-momentum (short-range) physics. For a large cutoff, interactions are called *hard* and short-range physics is much stronger. For more details on these interactions, see Epelbaum, Hammer, and Meißner (2009), Machleidt and Entem (2011), Piarulli and Tews (2020), and Tews *et al.* (2020).

The breakdown of chiral EFT signalizes that a systematic description of nuclear interactions in terms of nucleons and

pions is valid only at low energies. Hence, their applicability to study dense neutron matter in the core of neutron stars is limited. This also applies to phenomenological potentials, which are, however, typically fit to scattering data up to higher momenta than chiral EFT interactions. With a simple qualitative analysis, the momentum of two neutrons is related to the laboratory energy in a nucleon-nucleon collision with $k \approx \sqrt{E_{\rm lab} m/2}$, where $E_{\rm lab}$ is the energy of the nucleon-nucleon scattering in the laboratory frame. By equating the momentum k with the Fermi momentum, we can estimate the density at which these momenta are important, $n \approx (E_{\rm lab} m/2)^{3/2}/3\pi^2$. For a lab energy of 500 (600) MeV, this leads to a density estimate of 3 (4) times the nuclear saturation density.

Several families of two-body interactions have been derived within the chiral EFT framework (Entem and Machleidt, 2003; Epelbaum, Glockle, and Meissner, 2005; Gezerlis *et al.*, 2013, 2014; Ekström *et al.*, 2015; Piarulli *et al.*, 2015; Entem, Machleidt, and Nosyk, 2017; Somasundaram *et al.*, 2024). For calculations of neutron matter, potentials at next-to-next-to-leading order (N^2LO) (Lynn *et al.*, 2016; Tews *et al.*, 2018) and next-to-next-to-next-to-leading order (N^3LO) (Hebeler and Schwenk, 2010; Tews *et al.*, 2013; Drischler, Hebeler, and Schwenk, 2019; Keller, Hebeler, and Schwenk, 2023) have been employed. The most sophisticated chiral EFT interactions have been developed at next-to-next-to-next-to-next-to-leading order (N^4LO) (Entem, Machleidt, and Nosyk, 2017; Reinert, Krebs, and Epelbaum, 2018), and they reproduce nucleon-nucleon scattering data up to high energies well. Finally, interactions with explicit Δ degrees of freedom in the chiral expansion have been explored (Piarulli *et al.*, 2015; Jiang *et al.*, 2020).

Within chiral EFT three-body interactions are naturally predicted to appear at N^2LO (van Kolck, 1994) and come with two low-energy couplings, c_D and c_E. Given the fact that two-body interactions are constructed from nucleon-nucleon scattering data, the two extra parameters entering the chiral three-body potentials are typically fitted to properties of light nuclei with $A = 3$ and 4. Often, the two parameters are constrained by reproducing the experimental binding energies and/or charge radii of these systems (Navratil, 2007). Similarly, c_D can be constrained using the Gamow-Teller matrix elements related to the β decay of $A = 3$ nuclei (Marcucci *et al.*, 2012). It also has been suggested to constrain both the two- and three-body interactions at N^2LO by reproducing selected observable of scattering data and many-body systems simultaneously (Ekström *et al.*, 2013, 2015). The resulting interaction reproduced the properties of medium-mass nuclei and the equation of state of symmetric nuclear matter well but has a worse description of scattering data and neutron-rich dense matter. Three-body terms at N^3LO do not have new parameters (Bernard *et al.*, 2008, 2011), but, because of a complicated structure that involves many diagrams, they have been employed thus far mostly in calculations of nucleonic matter (Krüger *et al.*, 2013; Tews *et al.*, 2013; Drischler, Hebeler, and Schwenk, 2019).

The main advantages of interactions obtained within chiral EFT are that (i) they can be systematically improved and, more importantly, (ii) it is possible to estimate the theoretical uncertainty due to the truncation of the series expansion (Epelbaum, Krebs, and Meißner, 2015b; Drischler *et al.*, 2020). The easiest way to estimate these uncertainties was provided by Epelbaum, Krebs, and Meißner (2015b). Using this approach, the uncertainty associated with an observable X at N^2LO is given by

$$\Delta X^{\rm N^2LO} = \max(Q^4|X^{\rm LO}|, Q^2|X^{\rm NLO} - X^{\rm LO}|, Q|X^{\rm N^2LO} - X^{\rm NLO}|), \tag{18}$$

where order-by-order calculations of X are used and the scale Q is given by

$$Q = \max\left(\frac{p}{\Lambda_b}, \frac{m_\pi}{\Lambda_b}\right). \tag{19}$$

For homogeneous matter it is reasonable to take $p = k_F$ and $\Lambda_b \sim 500$ MeV as the breakdown scale. More sophisticated approaches using Gaussian processes have also been introduced (Drischler *et al.*, 2020), but they assume uncertainties to be Gaussian. However, the two approaches usually give similar uncertainty estimates (Keller, Hebeler, and Schwenk, 2023).

2. Microscopic many-body calculations

The EOS of nuclear matter is obtained by solving of the Schrödinger equation for many-body systems and finding its energy as a function of the density. The nuclear Hamiltonian is in general nonperturbative, and hence advanced numerical methods are required in order to calculate, for example, the dense matter EOS. Several works have been devoted to calculate the EOS of nuclear and neutron matter by starting from nuclear Hamiltonians that include two- and three-body interactions. The general form of the Hamiltonian is

$$H = -\frac{\hbar^2}{2m}\sum_i \nabla_i^2 + \sum_{i<j} v_{ij} + \sum_{i<j<k} V_{ijk} + \cdots, \tag{20}$$

which includes the kinetic energy operator, a two-nucleon interaction v_{ij}, and a three-nucleon interaction V_{ijk}, as previously discussed.

The various methods to calculate the EOS can be essentially divided into two different groups. The first group contains several methods that modify the Hamiltonian in such a way that the many-body problem is easier to solve. Examples of these methods include the well-known Brueckner-Hartree-Fock (BHF) (Vidaña *et al.*, 2000), and perturbative calculations (Drischler, Holt, and Wellenhofer, 2021). The BHF method essentially recasts the Hamiltonian into a one-body operator, and the residual part is evaluated by solving the Brueckner-Bethe-Goldstone (BBG) equation. The accuracy of the results obtained within the BBG approach depends on the expansion level adopted. The perturbative expansion of BBG is not convergent, but the cluster diagrams can be grouped with the number of independent hole lines (Pandharipande and Wiringa, 1979). Several attempts to study the convergence of hole-line expansion has been explored, but they are difficult to implement (Song *et al.*, 1998), and systematic uncertainties

cannot be quantified. See Vidaña, Margueron, and Schulze (2024) and references therein for recent work. Methods based on perturbation theory require the use of soft Hamiltonians, i.e., Hamiltonians without a strong repulsion at short distances (Hoppe *et al.*, 2017; Drischler, Holt, and Wellenhofer, 2021). This is generally achieved using techniques like the $V_{\mathrm{low\,k}}$ (Schwenk, Brown, and Friman, 2002; Bogner, Kuo, and Schwenk, 2003; Schwenk, Friman, and Brown, 2003) or similarity renormalization group (SRG) approaches (Bogner, Furnstahl, and Perry, 2007; Hebeler *et al.*, 2015); the latter approach has been dominant in recent years. With softened interactions the convergence in the perturbative order is much faster, but residual induced SRG three- and many-body interactions are difficult to include. Other methods in this group that have been used to investigate properties of neutron matter include the self-consistent Green's function (Carbone *et al.*, 2013; Carbone, Rios, and Polls, 2014) and coupled-cluster approaches (Baardsen *et al.*, 2013; Hagen *et al.*, 2014; Ekström *et al.*, 2018). They also rely on the use of soft interactions in order to achieve good convergence. The inclusion of three-body interactions is not straightforward when these methods are used. A density-dependent reduction or a normal ordering approximation are used to reduce the three-body interaction to a density-dependent two-body one that can be naturally included in addition to the original nucleon-nucleon interaction (Hebeler and Schwenk, 2010; Carbone *et al.*, 2013).

The second group of many-body methods make use of correlated wave functions where short-range two- and many-body correlations are explicitly included. This makes the wave function much more accurate, particularly when the system is strongly correlated. Such methods are generally more difficult to implement because in most cases high-dimensional integrals have to be solved, which requires numerical techniques based on Monte Carlo integrations to be invoked (Carlson *et al.*, 2015). Most of the results presented here have been obtained using the auxiliary field diffusion Monte Carlo method (which has proved to be an accurate method to calculate properties of nuclei; see the bottom panel of Fig. 3) and the nuclear and neutron-matter EOS (Schmidt and Fantoni, 1999; Gandolfi, Lovato *et al.*, 2014; Lonardoni, Carlson *et al.*, 2018; Lonardoni, Gandolfi *et al.*, 2018; Lonardoni *et al.*, 2020).

A completely different approach to calculating the EOS of dense matter is based on effective interactions that are constructed in the framework of the mean-field Hartree-Fock approximation. Since the original work by Skyrme in the 1950s (Skyrme, 1958), Skyrme interactions have become popular because they have an easy analytical form, and their energy density functionals provide a good description of several properties of nuclei and infinite nuclear matter. They also serve as the basis for the metamodeling approach of Margueron, Hoffmann Casali, and Gulminelli (2018). Skyrme interactions are basically contact interactions between nucleons, and they describe correlations at very low momenta, but they do not account for long-range nuclear correlations. This contact interaction is used to obtain a density-dependent three-body force (and thus the Skyrme force is not fully microscopic and cannot describe nucleon-nucleon scattering data). A great advantage of the Skyrme interactions is that they can be written in terms of a density functional, and an explicit analytical expression for nuclear matter can be derived. Given their relatively simple form, they do not (and are not intended to) accurately describe nucleon-nucleon phase shifts and properties of light nuclei. However, since the calculations of nuclear states within the Hartree-Fock approximation are relatively simple, the Skyrme models are common for investigating properties of medium and heavy nuclei.

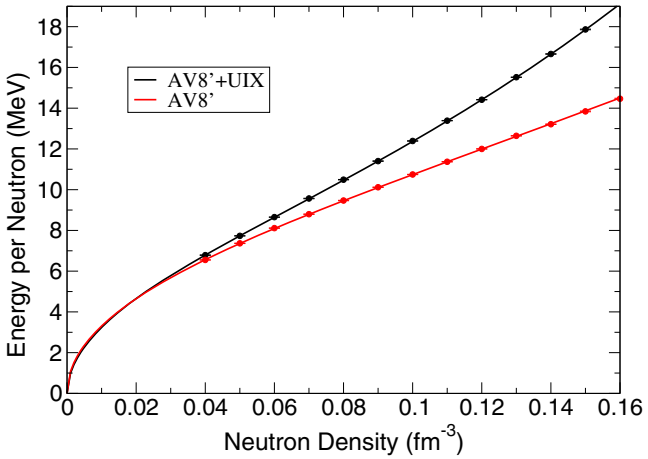

FIG. 4. The EOS of pure neutron matter calculated using the Argonne AV8′ two-body interaction (lower red symbols and line) and by also including the Urbana IX three-body interaction (upper black symbols and line). From Gandolfi, Carlson, and Reddy, 2012, and Gandolfi, Carlson *et al.*, 2014).

The EOS of nuclear and neutron-matter around saturation density has been extensively studied using different methods and Hamiltonians. As discussed, the general properties of the EOS of symmetric nuclear matter can be inferred via different experiments. In particular, the saturation point, the energy, and the compressibility are well constrained. However, the situation for pure neutron matter, which is more relevant for the physics of neutron stars, is much more complicated. As discussed, the pure neutron-matter EOS is related to the symmetric-matter EOS via the symmetry energy. Alternatively, calculations based on realistic nuclear Hamiltonians, which include precise information on two- and three-nucleon interactions, have been useful in predicting the EOSs of pure neutron matter.

We first focus on the role of three-body interactions. They are typically repulsive in pure neutron matter. This fact is dramatically important for the EOS, and hence for neutron stars. In Fig. 4 we show as an example the EOSs of pure neutron matter calculated with and without a three-body interaction. The two-body interaction is the Argonne AV8′, and the three-body interaction is the Urbana IX model. This nuclear Hamiltonian gives a good, although not perfect, description of light nuclei, and it has been extensively used in nuclear and neutron-matter calculations. However, the key point here is the role of three-neutron interactions. The three-neutron interactions are repulsive overall, and their role becomes increasingly important as the density increases.

More recent results for the EOS of pure neutron matter have been obtained using previously described chiral EFT Hamiltonians. In this case it is possible to estimate the

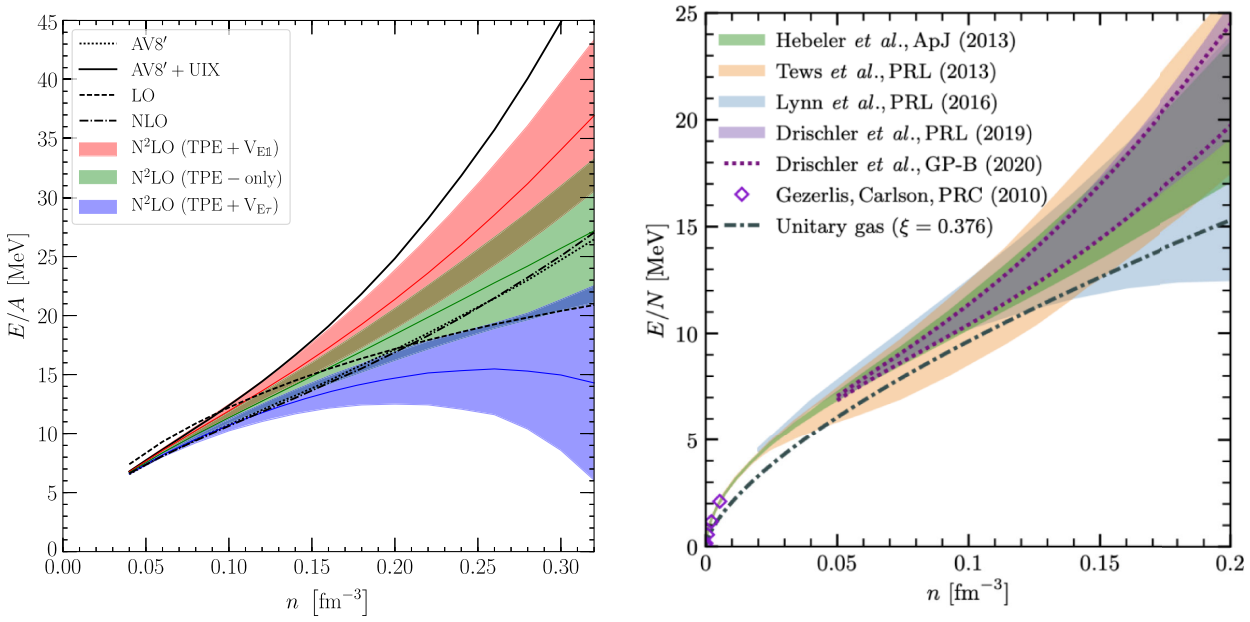

FIG. 5. The EOSs of pure neutron matter calculated using chiral Hamiltonians. Left panel: uncertainties shown only at N^{2}LO. The description of the various results is provided in the text. Adapted from Tews *et al.*, 2018. Right: comparison of results from Hebeler and Schwenk (2010), Tews *et al.* (2013), Lynn *et al.* (2016), Drischler, Hebeler, and Schwenk (2019), and Drischler *et al.* (2020). In addition, we show the low-density results of Gezerlis and Carlson (2010) and the unitary-gas bound of Tews *et al.* (2017). TPE, two-pion exchange. From Huth, Wellenhofer, and Schwenk, 2021.

systematic error due to the truncation in the chiral expansion as previously discussed. The results are shown in Fig. 5 for various orders in the EFT expansion and are compared to the results of Fig. 4. In the left panel, the uncertainties are shown only at N^{2}LO. Each uncertainty band reflects the truncation of the chiral EFT expansion, whereas the three different bands (colors) are obtained from taking into account regulator artifacts for three-nucleon forces for local chiral EFT interactions; see Dyhdalo *et al.* (2016), Lynn *et al.* (2016), and Huth *et al.* (2017). Although the three choices should be equivalent within EFT, this prediction is compromised by finite-range regulators, and the results for the EOSs differ using this approach to the EOSs. This leads to the uncertainty band becoming sizable at higher densities. In particular, the blue band is not physical, as neutron matter would become unstable at densities above saturation. However, these regulator artifacts vanish for large cutoffs, i.e., hard interactions, and show that the two upper bands (green and red) provide a reliable EOS that includes uncertainties (Tews *et al.*, 2024). For other many-body approaches, the magnitude of regulator artifacts can be different. In the right panel of Fig. 5, we compare the results for different chiral EFT interactions and many-body approaches, including quantum Monte Carlo and many-body perturbation theory results. While these calculations make much different assumptions and approximations and employ different models for three-nucleon interactions, the results are consistent.

Generally, the energy of pure neutron matter as a function of the density can be parametrized as

$$\frac{E}{A}(n) = a\left(\frac{n}{n_0}\right)^{\alpha} + b\left(\frac{n}{n_0}\right)^{\beta}, \tag{21}$$

where a, α, b, and β are the fitting parameters. When this form is used, the value of the symmetry energy and its slope at saturation density are given by

$$S = a + b + 16,$$
$$L = 3(a\alpha + b\beta). \tag{22}$$

The parametrizations of the EOSs shown in Fig. 4 are reported in Table I together with the corresponding symmetry energy and slope.

TABLE I. Fitting parameters for the neutron-matter EOS defined in Eq. (21) using different nuclear Hamiltonians. The AV8′ and AV8′ + UIX results are from Gandolfi, Carlson *et al.* (2014). For chiral interactions the fits are obtained from the central values (solid lines) of each band reported by Lonardoni *et al.* (2020). We have omitted the unphysical results.

Hamiltonian	S (MeV)	L (MeV)	a (MeV)	α	b (MeV)	β
AV8′	30.5	31.3	12.7	0.49	1.78	2.26
AV8′ + UIX	35.1	63.6	13.4	0.514	5.62	2.436
N^{2}LO (TPE + V_{E1})	33.3	46.4	13.2	0.503	4.07	2.17
N^{2}LO (TPE only)	31.6	33.8	11.0	0.426	4.59	1.44

Within Skyrme models the EOS is expressed as the energy per particle,

$$\frac{E}{A}=\frac{3\hbar^2}{10m}\left(\frac{3\pi^2}{2}\right)^{2/3}n^{2/3}H_{5/3}+\frac{t_0}{8}n[2(x_0+2)-(2x_0+1)H_2]+\frac{1}{48}\sum_{i=1}^{3}t_{3i}n^{\sigma_i+1}[2(x_{3i}+2)-(2x_{3i}+1)H_2]+\frac{3}{40}\left(\frac{3\pi^2}{2}\right)^{2/3}n^{5/3}(aH_{5/3}+bH_{8/3}), \tag{23}$$

with

$$\begin{aligned} a &= t_1(x_1+2)+t_2(x_2+2),\\ b &= \tfrac{1}{2}[t_2(2x_2+1)-t_1(2x_1+1)],\\ H_n(x) &= 2^{n-1}[x^n+(1-x)^n], \end{aligned} \tag{24}$$

where $x=n_p/n$ is the proton fraction. All the various parameters entering in the Skyrme functional are typically fit to reproduce selected properties of atomic nuclei and the properties of the known quantities of nuclear and neutron matter, like binding energy and charge radii of nuclei, saturation density and the energy and nuclear compressibility of symmetric nuclear matter, symmetry energy, etc. From Eq. (24) it is possible to derive the formula for the pressure, compressibility, symmetry energy, effective mass, etc. A few representative Skyrme parametrizations are presented in Table II.

E. The equation of state in β equilibrium

Thus far, we have mainly discussed the EOS of pure neutron matter around saturation density. However, as the chemical potential of neutrons in neutron stars is sufficiently high, it is energetically more favorable to have a finite fraction of protons and negatively charged leptons. Several neutron-star properties, such as the mass and radius, can be calculated in a good approximation directly starting with the pure neutron-matter EOS, but such an approximation misses the effects of the neutron-star crust and the remaining protons. A more realistic EOS should include these effects, which can be estimated from the pure neutron-matter EOS and information on the saturation point of symmetric nuclear matter. Here we describe how to include the effects of protons in the EOS by starting with a few assumptions. We then discuss how to calculate neutron-star properties in Sec. V.

By starting with Eqs. (1) and (2), we can solve for $\beta(\rho)$ by imposing β equilibrium between neutrons, protons, electrons, and muons. This can be done by imposing the conservation of the total chemical potential. We rewrite Eq. (1) in terms of the proton fraction,

$$x=\frac{n_p}{n}, \tag{25}$$

and consider the total energy density of the system,

$$\varepsilon = n\left[\frac{E}{A}(n,x)+m_n(1-x)+m_p x\right], \tag{26}$$

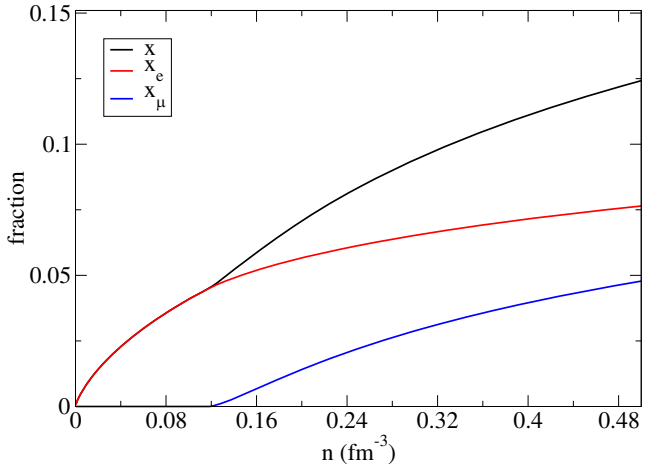

FIG. 6. Proton and lepton fractions obtained from the auxiliary field diffusion Monte Carlo EOS defined in Table I using the AV8' + UIX parametrization. Adapted from Gandolfi *et al.*, 2019.

where m_n and m_p are the neutron and proton rest mass. The difference between the neutron and proton chemical potentials is given by

$$\mu_n-\mu_p=4(1-2x)S(n), \tag{27}$$

where $S(n)$ can be calculated from the EOS as in Eqs. (8) and (9). β decay requires

$$\mu_n-\mu_p=\mu_e=\mu_\mu. \tag{28}$$

A good approximation is to consider electrons and muons as noninteracting particles.

The electron chemical potential for relativistic and degenerate electrons is given by

$$\mu_e=(m_e^2+\hbar^2k_F^2)^{1/2}=[m_e^2+\hbar^2(3\pi^2nx_e)^{2/3}]^{1/2}, \tag{29}$$

where x_e is the electron fraction defined in a manner similar to the proton fraction and n is the total density of the system. Since the mass of the muons is much larger, they can be treated as a nonrelativistic free Fermi gas. Their chemical potential is given by

$$\mu_\mu=[m_\mu^2+\hbar^2(3\pi^2nx_\mu)^{2/3}]^{1/2}. \tag{30}$$

The fractions x, x_e, and x_μ can all be calculated by imposing charge neutrality and using the relations for the chemical potentials as before,

$$x=x_e+x_\mu. \tag{31}$$

As an example, we show the proton and lepton fractions for the EOS in Table I using the AV8′ + UIX parametrization of Fig. 6. Protons and electrons have finite fractions starting at very low densities because the symmetry energy $S(n)$ is finite at any density. The muons instead appear at larger densities,

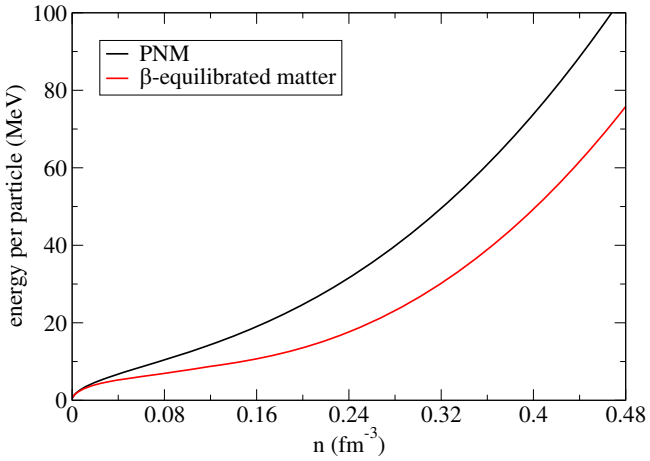

FIG. 7. The EOS of pure neutron matter compared to the β-equilibrated one using the AV8′ + UIX nuclear Hamiltonian.

around $n \approx 0.12$ fm^{-3}, because of their larger mass compared to the electrons.

The EOS for pure neutron matter is compared to the β-equilibrated one in Fig. 7. When protons and leptons are included, the EOS is softened. The EOS of homogeneous matter in β equilibrium is a valid model for high densities starting at the outer core of neutron stars, where nuclei are no longer present.

F. Matter at high densities: Quarks, hyperons, pions, and other degrees of freedom

At higher densities degrees of freedom other than nucleons and electrons may appear, and a reasonable first step is to presume that matter may consist of degrees of freedom that we have observed in the laboratory, for example, exotic mesons and baryons. Because QCD is asymptotically free, quarks may also become deconfined. Finally, the relevant degrees of freedom in neutron stars may be qualitatively new degrees of freedom that we have not yet otherwise observed.

We expect the baryon number to be approximately conserved and the electric charge to be exactly conserved. Thus, the degrees of freedom can be organized according to the chemical potential for baryon number μ_B and charge μ_Q,

$$\mu_i = B_i \mu_B + Q_i \mu_Q, \tag{32}$$

where B_i is the baryon number of particle i and Q_i is the charge of particle i (keeping in mind that the chemical potentials of each particle include the contribution from the rest mass). We do not include an additional term for strangeness in Eq. (32), because it is not conserved except for very short times in core-collapse supernovae and neutron-star mergers.

Most of the work in dense matter is done in the mean-field approximation. In addition, the dispersion relations (the relationship between energy and momentum) of the relevant degrees of freedom are often assumed to be similar to their noninteracting counterparts, except that the mass and chemical potential are modified by the mean field. In the mean-field approximation at $T = 0$, exotic fermions appear if their chemical potential is greater than their mass (keeping in mind that both the chemical potential and the mass may be modified by the dense medium). The maximum baryon chemical potential in neutron-star interiors is typically less than about 2 GeV, and thus the quark chemical potential is less than 700 MeV, which rules out τ leptons and hadrons containing charm, bottom, or top quarks (but strange quarks may occur). At $T = 0$ bosons appear when they form a Bose condensate, i.e., when their chemical potential is equal to their mass. An early model of Bose condensation based on a chirally symmetric Lagrangian comes from Kaplan and Nelson (1986). At lower densities pions can be described using EFTs similar to the previously discussed ones without explicit pion degrees of freedom. According to Eq. (32), negatively charged pions and muons have the same chemical potential. Because pions and muons have similar masses, one would naively expect pions and muons to be in similar conditions in dense matter. However, strong interactions involving pions strongly modify the in-medium values of the mass and the chemical potential (Fore and Reddy, 2020)

Models of hyperons in dense matter [see the reviews by Chatterjee and Vidaña (2016) and Tolos and Fabbietti (2020)] typically take one of two forms: extensions of relativistic mean-field theories (Horowitz and Serot, 1981) to include hyperon degrees of freedom (Reinhard, 1989) or applications of Brueckner-Hartree-Fock theory (Vidaña *et al.*, 2000). These models can be constrained by the increasing amount of data on hypernuclei; see the quantum Monte Carlo results of Lonardoni, Gandolfi, and Pederiva (2013) and Lonardoni, Pederiva, and Gandolfi (2014). For example, the binding energy of the Λ hyperon in isospin-symmetric nuclear matter is approximately −28 MeV. There is also an increasing amount of information on hyperon-nucleon interactions from lattice QCD (Beane *et al.*, 2007). Adding degrees of freedom to a system of degenerate fermions tends to lower the pressure; thus, hyperons tend to lower the maximum mass of a cold neutron star (Glendenning and Moszkowski, 1991). Hyperonic models sometimes need to be supplanted by quark models at higher densities in order to increase the pressure enough to explain the existence of $2M_\odot$ neutron stars.

TABLE II. Parameters of Skyrme EOSs for selected models. The following units are used: MeV fm^3 for t_0, MeV fm^5 for t_1 and t_2, and MeV fm$^{3(1+\alpha)}$ for t_{3i}. The other parameters are dimensionless.

Skyrme	t_0	t_1	t_2	t_3	x_0	x_1	x_2	x_3	α	Reference
NRAPR	−2719.7	417.64	−66.687	15 042	0.161 54	−0.047 986	0.027 170	0.136 11	0.144 16	Steiner *et al.* (2005)
SV-min	−2112.2	295.78	142.27	13 989	0.243 89	−1.4349	−2.6259	0.258 07	0.255 37	Klüpfel *et al.* (2009)
UNEDF2	−1735.5	262.81	1183.31	12 293	0.172 25	−3.7669	−1.3835	0.052 864	0.351 46	Kortelainen *et al.* (2014)

Descriptions of deconfined quark matter typically take one of four forms: (i) purely phenomenological models similar to the "MIT bag" model; (ii) models related to the Nambu–Jona-Lasinio model, where quarks are described with a nonrenormalizable Lagrangian with chiral symmetry (Klevansky, 1992; Hatsuda and Kunihiro, 1994); (iii) high-density effective theories (Hong, 2000); or (iv) calculations from perturbative QCD (Komoltsev and Kurkela, 2022; Gorda, Komoltsev, and Kurkela, 2023; Komoltsev *et al.*, 2024). In addition, the relevant degrees of freedom in the core of neutron stars may be different than those encountered in vacuum; for an example, see Jeong, McLerran, and Sen (2020). Finally, quarks could also appear in a quarkyonic phase at intermediate densities where quarks and nucleons form a common Fermi sea (McLerran and Reddy, 2019).

G. Matter at high densities: Phenomenological models

In lieu of these more complex models of dense matter, which are specialized to a particular class of degrees of freedom, more generic phenomenological models have been used. These more generic models can express all possible EOSs in a form that is easy to evaluate. These kinds of models are often useful in the analysis of neutron-star observational data to obtain an EOS of $T = 0$ matter in β equilibrium. In these models, above a density n_t that is usually chosen as $n_0 < n_t < 2n_0$, the EOS is phenomenologically modeled.

One possible approach is to use polytropes, i.e.,

$$P_i(\varepsilon) = K_i \varepsilon^{1+1/n_i}, \tag{33}$$

where P is the pressure as a function of the energy density ε and K_i and n_i are parameters that can change the soft stiffness of the EOS. Several polytropes can be used in such a way that the EOS can have more freedom, and they also include eventual phase transitions. The different polytropes are used to model the EOS in different density regimes (Read *et al.*, 2009). For example,

$$P(\varepsilon) = \begin{cases} K_1 \varepsilon^{1+1/n_1} & n_t < n < n_{t1}, \\ K_2 \varepsilon^{1+1/n_2} & n_{t1} < n < n_{t2}, \\ K_3 \varepsilon^{1+1/n_3} & n_{t2} < n < n_{t3}. \end{cases} \tag{34}$$

In this case, given the transition densities n_t, n_{t1}, n_{t2}, and n_{t3}, the parameters must be chosen in order to ensure that the pressure monotonically increases across a finite number of jumps in energy density (which correspond to phase transitions).

Another parametrization for the high-density EOS is in terms of the speed of sound c_s (Tews *et al.*, 2018; Greif *et al.*, 2019). The speed of sound can be obtained in different ways, for example,

$$c_s^2 = \frac{\partial P(\varepsilon)}{\partial \varepsilon}. \tag{35}$$

Causality imposes the constraint that c_s cannot exceed the speed of light, and mechanical stability requires that the speed of sound be positive. At a sufficiently high density, $c_s^2/c^2 \to 1/3$ since quarks at high momenta are asymptotically free. In the regime where the EOS is dominated by neutron matter (as previously discussed), the value of c_s can be directly obtained from the calculated EOS; the speed of sound can be obtained from selected Hamiltonians presented previously and is shown in Fig. 8. We find that c_s grows with the density for different Hamiltonians. At higher densities c_S can have different possible behaviors. In Fig. 9 we schematically show two possible curves for c_S^2, one exceeding the limit of $1/3$ at intermediate densities and another where this limit is valid. Exceeding the limit of $1/3$ implies the existence of strongly correlated matter in the core of neutron stars.

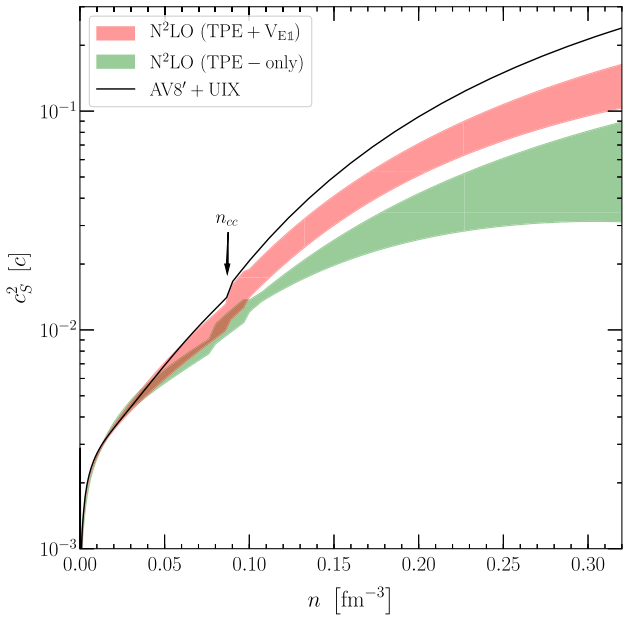

FIG. 8. Speed of sound squared as a function of density for neutron-star matter based on selected EOSs that were presented in Fig. 5. In this case an EOS for the crust has been included for densities lower than $n_{cc} \approx n_0/2$. From Tews *et al.*, 2018.

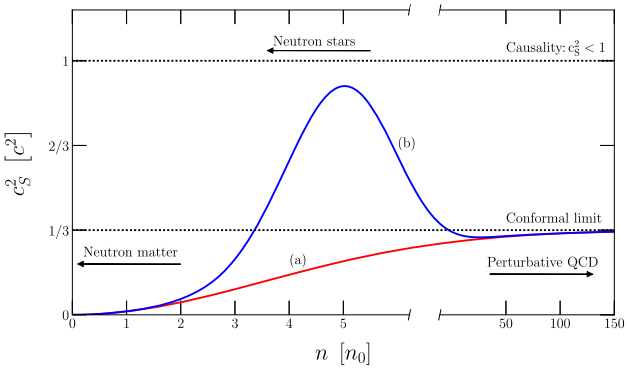

FIG. 9. (a),(b) Examples of two possible scenarios for the evolution of the speed of sound in dense matter; see Tews *et al.* (2018) for details.

IV. CONSTRAINTS FROM NUCLEAR EXPERIMENTS

We now give an overview of experimental constraints to the EOS. We describe how nuclear observables—binding energies, radii, etc.—are used to construct nuclear interactions. Then we focus on experimental data that are commonly used to constrain the EOS, in particular, on measurements of the neutron-skin thickness and its connection to macroscopic properties like symmetry energy and its derivatives. This section also describes the connection between the neutron-star EOS and heavy-ion collisions. We expect that in the near future gravitational-wave observations will provide a significant amount of information about the EOS. However, heavy-ion collisions provide two important constraints. First, they potentially constrain neutron-star matter between the nuclear saturation density (where the momenta are sufficiently small that chiral effective theory provides an accurate description of neutron-star matter) and higher densities that will be constrained by future GW observations. Second, they potentially constrain the in-medium nucleon single-particle potentials, information that is difficult to access via GW observations.

A. Nuclear structure experiments

As described, the nuclear EOS can generally be calculated by starting with nuclear Hamiltonians that include two-, three-, and many-body interactions. These interactions contain free parameters that need to be constrained by available experiments.

Nuclear Hamiltonians have been derived in a phenomenological way or based on chiral effective field theory. Although several parameters can be extracted from nuclear experiments, for example, π-nucleon couplings, many other parameters have to be indirectly constrained by other types of experiments that need to solve the nuclear two- and many-body problems, for example, the binding energy and other properties of light nuclei. The parameters entering the two-body interactions are commonly fit in order to reproduce nucleon-nucleon scattering data; see Wiringa, Stoks, and Schiavilla (1995), Entem and Machleidt (2003), and Epelbaum, Glockle, and Meissner (2005).

The fitting of free parameters entering the three-body interaction requires a different approach. The most precisely measured nuclear observables include the binding energy (or nuclear masses) and charge radii, which are provided by experimental electron scattering off nuclei that are under good control. Typically, three-body interactions are constrained by calculating properties of very light nuclei, where exact calculations of the nuclear ground state are available. Observables that are commonly chosen include the binding energy and/or charge radii of light nuclei such as ^{3}H, ^{3}He, and ^{4}He (Navratil *et al.*, 2007; Hebeler *et al.*, 2011; Somà *et al.*, 2020) and neutron-α scattering; see Lynn *et al.* (2016). Other observables of such light systems can also be used, for example, neutron-deuteron scattering. Free parameters entering the nuclear Hamiltonians have also been constrained to reproduce the saturation density and energy of symmetric nuclear matter and/or properties of medium-mass nuclei (Ekström *et al.*, 2015). However, the latter approach relies on many-body calculations of such systems that are not as accurate as calculations of few-body systems. Within chiral effective field theory, nuclear β decays can also be included in the fit. This is because the electroweak operators that describe the interactions between nucleons with an external lepton and neutrino are related to three-body interactions (Gazit, Quaglioni, and Navratil, 2009; Baroni *et al.*, 2018).

Density functionals and/or models based on the mean-field approximation, such as Skyrme interactions, are typically constrained by considering only binding energies and charge radii and distributions of medium and heavy nuclei.

B. Neutron-skin thickness

Heavy atomic nuclei typically have an excess of neutrons over protons, with proton fractions on the order of 40%. As the densities inside the atomic nucleus are limited because of nuclear saturation, the additional neutrons are not located in the center of the nucleus. Instead, the radius of protons in the nucleus, as measured by the point proton radius R_p, is usually smaller than the radius of the neutrons measured by the point neutron radius R_n. The neutron-skin thickness is defined as their difference, $R_{\rm skin} = R_n - R_p$ (Thiel *et al.*, 2019). It describes the thickness of the neutron layer at the surface of the atomic nucleus. Qualitatively, the neutron-skin thickness is proportional to the pressure among neutrons, as a larger pressure leads to the neutrons occupying a larger volume. Therefore, the neutron-skin thickness is an important observable for learning about the behavior of the neutron-matter EOS. Usually, the neutron-skin thickness is used to constrain the slope of the symmetry energy L introduced earlier because L is proportional to the pressure of pure neutron matter at nuclear saturation density. Indeed, it has been found that $R_{\rm skin}$ and L are correlated (Horowitz and Piekarewicz, 2001; Typel and Brown, 2001; Carriere, Horowitz, and Piekarewicz, 2003; Klüpfel *et al.*, 2009; Viñas *et al.*, 2014; Mondal *et al.*, 2016; Reinhard and Nazarewicz, 2016). More skin implies a larger value of L, and hence a larger pressure of pure neutron matter at saturation density.

In recent years several experiments have aimed at measuring the neutron-skin thickness to constrain the EOS of neutron matter. These experiments include measurements of the neutron-skin thickness in ^{208}Pb via the dipole polarizability (Tamii *et al.*, 2011; Roca-Maza *et al.*, 2015; Birkhan *et al.*, 2017) or via parity violating electron scattering in the PREX-II experiment (Adhikari *et al.*, 2021). Analogously to the latter, the skin was also measured in ^{48}Ca in the CREX experiment (Adhikari *et al.*, 2022). These experiments were also discussed by Reinhard, Roca-Maza, and Nazarewicz (2021) and Lattimer (2023).

The impact of these measurements on the EOS was recently analyzed by Essick, Landry *et al.*, 2021; Essick, Tews *et al.*, 2021; Reed *et al.*, 2021; Koehn *et al.*, 2024). Figure 10 shows the resulting posterior for the symmetry energy and its slope at n_0 extracted from the CREX, PREX-II, and dipole-polarizability measurements of Koehn *et al.* (2024). The CREX and PREX experiments both give posteriors that have only modest overlap (Miyatsu *et al.*, 2023; Reed *et al.*, 2024). This might point to the need for improved theoretical modeling to reduce systematic uncertainties in both measurements. In addition to

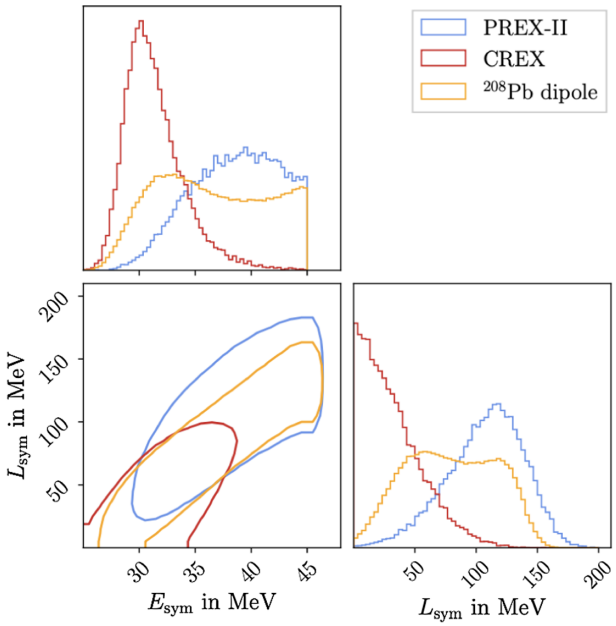

FIG. 10. Posteriors of the symmetry energy $E_{\rm sym}$ and its slope $L_{\rm sym}$ at saturation density inferred from the PREX-II (blue lines), CREX (red lines), and lead dipole-polarizability (orange lines) experiments of Koehn *et al.*. The contours denote the 95% credibility intervals. From Koehn *et al.*, 2024.

these experiments, Essick, Landry *et al.* (2021) analyzed the impact of measurements of the dipole polarizability of ^{208}Pb and found them to be in good agreement with predictions from chiral EFT and CREX (Tamii *et al.*, 2011; Roca-Maza *et al.*, 2013, 2015). Finally, microscopic calculations in the framework of chiral EFT have also promoted the study of correlations between neutron skins and the EOS (Hu *et al.*, 2022).

C. Heavy-ion collisions

Intermediate-energy heavy-ion collisions (HICs) have the promise to provide novel constraints on the EOS of dense matter because they probe matter above the nuclear saturation density.[2] However, this is not without complications: during the time when high-densities are obtained, the temperatures are still large and matter is not in equilibrium. In addition, at these energies nucleons are still often clustered into light nuclei. Finally, the particles that are observed in HICs (nuclei, nucleons, pions, etc.) are not necessarily connected in a model-independent way to the hot and dense matter achieved in the collision itself. Thus, complicated modeling is required to convert information obtained from intermediate-energy HIC observables to quantitative constraints on the nature of hot and dense matter in thermodynamic equilibrium.

There are several methods for analyzing intermediate-energy HIC data. The most popular are based on the Boltzmann-Uehling-Uhlenbeck (BUU) equation (Danielewicz and Bertsch, 1991; Li and Gross, 1993) and quantum molecular dynamics (QMD) (Zhang and Li, 2006). The BUU equation describes a semiclassical formalism that describes the spacetime evolution of the particle distribution functions in terms of collision integrals, which encode the information about reactions between the associated degrees of freedom. In QMD nucleons are represented by Gaussian wave packets that interact with each other and with the background mean field. QMD is particularly adept at treating clusters of nucleons, which are more difficult to describe in the BUU formalism.

Despite these challenges, HICs provide vital information for hot and dense matter; see Li, Chen, and Ko (2008), Tsang *et al.* (2009), Huth *et al.* (2022), and Sorensen *et al.* (2024). One common application of HICs is to provide constraints on the slope of the nuclear symmetry energy, L; see Sec. III.A. This parameter has been constrained to values between 40 and 110 MeV (see Li, Chen, and Ko (2008) and Tsang *et al.* (2009). These constraints are not fully model independent. In addition, HICs are the only constraint on the nature of isospin-symmetric matter at high densities [pioneered by Danielewicz, Lacey, and Lynch (2002). Finally, they have demonstrated that the simple dispersion relation for nucleons, which is quadratic only in the momentum, is likely not appropriate for all densities and temperatures (Aichelin *et al.*, 1987). The latter point may be particularly important for the proper modeling of neutron-star mergers. A particularly important frontier on the theory side is the systematic calibration of various numerical methods used to analyze HIC data (Xu *et al.*, 2016)

V. FROM MICROPHYSICS TO NEUTRON-STAR STRUCTURE

Gravitational waves and electromagnetic observations can be used to infer macroscopic properties of neutron stars, in particular, their masses, radii, and tidal deformabilities. While these measurements are agnostic to the microphysics, nuclear theory is needed for their interpretation. This section reviews how the microphysical description on dense nuclear matter impacts the macroscopic properties of neutron stars. We review the general-relativistic equations of stellar structure, the Tolman-Oppenheimer-Volkoff (TOV) equations, in Sec. V.A and discuss how they directly determine the mass and radius. Tidal properties of neutron stars and the tidal deformability parameter are discussed in Sec. V.B. Unless otherwise stated, we work in geometric units where Newton's constant and the speed of line are $G = c = 1$.

A. The Tolman-Oppenheimer-Volkoff equation

Neutron stars are the most compact material objects we know of, with compactness $C \equiv M/R \sim 0.2$.[3] This suggests that general-relativistic effects meaningfully impact their macroscopic appearance. Spherically symmetric solutions in general relativity are simple: Birkhoff's theorem states that vacuum spherically symmetric solutions are also static and asymptotically flat, which implies that the spacetime outside a nonrotating neutron star is equal to the well-known Schwarzschild spacetime. The interior solution must match

[2]Higher-energy heavy-ion collisions achieve higher temperatures but lower densities than intermediate-energy collisions.

[3]Black holes are the only objects that are more compact ($C = 1/2$), but they are not made of matter.

to the Schwarzschild one on the star surface and satisfy the nonvacuum Einstein equations.

The most simple interacting fluid is the perfect fluid, with no heat conduction or viscosity. It can be fully characterized by its isotropic pressure P and its energy density ε. These conditions lead to a diagonal stress-energy tensor,

$$T_{\mu\nu} = (\varepsilon + P)u_\mu u_\nu + P g_{\mu\nu}, \tag{36}$$

where u_μ is the fluid four-velocity and $g_{\mu\nu}$ is the spacetime metric. The time-time component of the Einstein equations is

$$\frac{dm(r)}{dr} = 4\pi r^2 \varepsilon(r), \tag{37}$$

where r is the radial coordinate and $m(r)$ is a function that parametrizes the time-time component of the metric. Matching to the Schwarzschild solution allows us to identify $m(R) = M$, the neutron-star mass as measured by a distant observer.[4] Therefore, $m(r)$ is the enclosed mass, and local flatness at the star center imposes $m(r = 0) = 0$.

The momentum-energy conservation, $T^{\mu\nu}_{;\nu} = 0$, and the r-r component of the Einstein equations yields the TOV equation (Oppenheimer and Volkoff, 1939; Tolman, 1939), the general-relativistic equation of the hydrostatic equilibrium between the outward pressure and the inward gravitational attraction,

$$\frac{dP}{dr} = -[\varepsilon(r) + P(r)]\left[\frac{m(r)}{r^2} + 4\pi r P(r)\right]\left[1 - \frac{2m(r)}{r}\right]^{-1}. \tag{38}$$

This is the special and general-relativistic generalization of the Newtonian equation of hydrostatic equilibrium, to which it reduces for $P(r) \ll \varepsilon(r)$ and $m(r) \ll r$. In each set of square brackets, the second term provides corrections beyond Newtonian physics: the first two are special relativistic, while the third is a general-relativistic correction. The last term justifies the use of $C = M/R$ as a measure of how important general-relativistic corrections are. Notably, all three corrections increase the effect of gravitational attraction.

Finally, the pressure P appears on both the left-hand and right-hand sides of Eq. (38). The former is pressure's usual role: the pressure gradient provides an outward force stabilizing the star. The latter is novel. In general relativity all forms of energy contribute to gravity, and therefore pressure contributes to the gravitational pull as well. This suggests that, regardless of how much pressure nuclear physics can create, there is a limit to how massive neutron stars can become before the pressure derivative diverges and the star collapses.

Equations (37) and (38) form a system of two equations for three unknowns: $m(r)$, $P(r)$, and $\varepsilon(r)$. The system is closed by a third external equation, the neutron-star EOS

$$P = P(\varepsilon). \tag{39}$$

[4]This is not the density integrated over the star volume, with the difference being the negative gravitational binding energy.

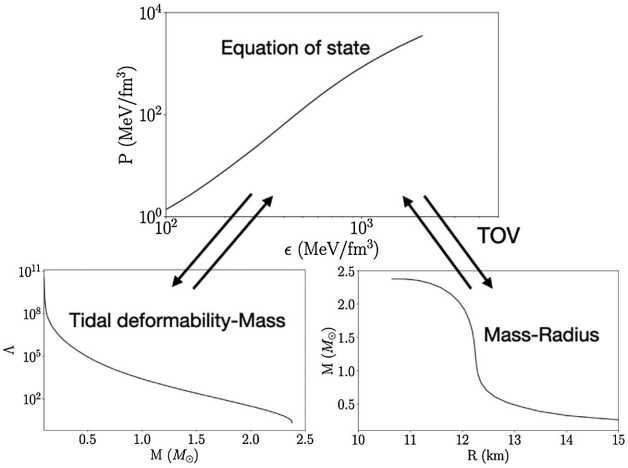

FIG. 11. Schematic showing the link between microscopic and macroscopic neutron-star properties. A nuclear EOS for the pressure P as a function of the energy density ε (top panel) completes the equations of stellar structure, Eqs. (37) and (38), and leads to a unique curve on the mass M and radius R plane (bottom right panel) for static, spherically symmetric neutron stars. Perturbed neutron stars are deformed away from equilibrium. The $\ell = 2$ perturbation is characterized by the dimensionless tidal deformability Λ as a function of the mass (bottom left panel) [Eq. (47)], which again depends on the EOS.

This system of three equations for three unknowns defines a sequence of neutron stars as a function of mass M or, equivalently, central density ε_c or pressure $P_c = P(\varepsilon_c)$, see Silbar and Reddy (2004). For a given central pressure, Eqs. (37) and (38) can be integrated outward with boundary conditions $m(r = 0) = 0$ and $P(r = 0) = P_c$. The star's surface is reached when $P(r = R) = 0$, at which point $M = m(r = R)$ is the star's mass. Repeating this process for different values of P_c "converts" an EOS $P(\varepsilon)$ to a stellar sequence $M(R)$, as shown in Fig. 11. The mapping is one to one and invertible (Lindblom, 1992).

B. Tidal deformability

The TOV equations describe the equilibrium configuration of a static, spherically symmetric neutron star. Nonrotating neutron stars in binaries will, however, be perturbed away from spherical symmetry owing to the gravitational impact of their companion. An external gravitational field that is spatially inhomogeneous will result in a varying spacetime curvature throughout the star's ∼25-km-wide body. This tidal interaction is conceptually similar to Newtonian tidal forces (Poisson and Will, 2014), though now the phenomenon needs to be described in terms of quantities derived from the spacetime metric, rather than forces.

In a binary the external tidal field created by the companion varies in the orbital timescale given by Kepler's law,

$$\tau_{\rm orb} \sim \frac{1}{\omega_{\rm orb}} \sim \sqrt{\frac{r^3}{M_T}}, \tag{40}$$

where $\omega_{\rm orb}$ is the orbital frequency, r is the binary separation, and M_T is the binary total mass. Responding to this, the neutron star adjusts to a new nonsperical equilibrium configuration at a timescale characteristic of its internal oscillation modes, the fundamental of which is dominant,

$$\tau_{\rm resp} \sim \frac{1}{f_2} \sim \sqrt{\frac{R^3}{M}}, \tag{41}$$

where f_2 is the fundamental mode frequency, R is the perturbed neutron-star radius, and M is its mass. For sufficiently widely separated binaries,

$$\frac{\tau_{\rm resp}}{\tau_{\rm orb}} \sim \left(\frac{R}{r}\right)^{3/2} \ll 1, \tag{42}$$

implying that the perturbation is static and the neutron star instantaneously adjusts the location of the induced tidal bulge to turn toward and away from its companion. Physically, the companion tidal field acts as a nonresonant driving force on the star's fundamental modes.

In general relativity the tidal deformation manifests in the asymptotic behavior of the spacetime metric at large distances from the star. In the asymptotic Cartesian rest frame of the neutron star whose origin coincides with its center of mass, the time-time component of the metric g_{tt} can be expressed via a multipolar expansion (Thorne, 1980, 1998),

$$\frac{1-g_{tt}}{2} = -\frac{M}{r} - \frac{3Q_{ij}}{2r^3}\left(n^i n^j - \frac{1}{3}\delta^{ij}\right) + \mathcal{O}(r^{-4}) + \frac{1}{2}\mathcal{E}_{ij} r^2 n^i n^j + \mathcal{O}(r^3), \tag{43}$$

where r is the distance from the neutron star, n_i are unit vectors pointing along the coordinates, and δ^{ij} is the Kronecker δ. The first line in Eq. (43) represents a multipolar expansion of the field sourced by the neutron star. The M/r term represents the standard monopolar term. The $\sim 1/r^2$ term vanishes identically since the neutron star is placed at the origin of the coordinate frame. The $\sim 1/r^3$ term represents the quadrupolar correction, with the coefficient Q_{ij} defining the tidally induced quadrupole moment. Higher-multipolar corrections are represented by $\mathcal{O}(r^{-4})$. The second line in Eq. (43) is the contribution of the external field, with the $\sim r^2$ term representing the quadrupolar tidal field defined as $\mathcal{E}_{ij}$. Higher-order corrections are included in $\mathcal{O}(r^3)$. In Newtonian gravity Q_{ij} would be given by integrating density perturbations over the star, while $\mathcal{E}_{ij}$ would be given by spatial derivatives of the companion's field (Poisson and Will, 2014). In general relativity both quantities are defined via Eq. (43).

Though their definitions and calculations differ, in both Newtonian and relativistic gravity and under static perturbations, the tidally induced quadrupole moment is proportional to the perturbing field, with the constant of proportionality defining the tidal deformability

$$\lambda \equiv -\frac{Q_{ij}}{\mathcal{E}_{ij}}. \tag{44}$$

Given an external perturbation $\mathcal{E}_{ij}$, the tidal deformability λ quantifies how much the star is deformed. Intuitively, a larger star should be more deformable; therefore, λ should increase with the neutron-star radius R. Moreover, dimensional analysis based on Eq. (43) suggests that $Q_{ij} \sim [\mathrm{L}]^3$, while $\mathcal{E}_{ij} \sim [\mathrm{L}]^{-2}$, suggesting that $\lambda \sim [\mathrm{L}]^5$. Indeed, λ is related to the dimensionless tidal Love number k_2 as

$$\lambda = \tfrac{2}{3} k_2 R^5. \tag{45}$$

In the context of gravitational-wave observations (Sec. VI), tidal effects are imprinted on the signal through the dimensionless tidal deformability,

$$\Lambda \equiv \frac{\lambda}{M^5} = \frac{2}{3} k_2 \frac{R^5}{M^5} = \frac{2}{3} k_2 C^{-5}. \tag{46}$$

For a neutron star of a given mass, both k_2 and R depend on the neutron-star EOS and thus offer complementary information. Typical values lie in the range $k_2 \sim 0.05$–0.1 (Hinderer *et al.*, 2010), while Λ is typically $\mathcal{O}(10^2$–$10^3)$. For a given EOS, Λ is a steep function of the mass. For $m \gtrsim 1M_\odot$, $k_2 \sim M^{-1}$ (Zhao and Lattimer, 2018), bringing the total dependence to $\Lambda \sim M^{-6}$. Indeed, $\Lambda \sim \mathcal{O}(10^4)$ for $M = 1M_\odot$ and drops to $\Lambda \sim \mathcal{O}(10)$ for $m = 2M_\odot$ (see Fig. 11), suggesting that the measurability of the tidal deformability is a sensitive function of the binary mass. The tidal deformability of a black hole is zero (Binnington and Poisson, 2009; Chia, 2021).

Calculating λ for a given neutron star amounts to introducing a static $\ell = 2$ perturbation to the Einstein equations and computing the metric asymptotically (Thorne and Campolattaro, 1967), extracting the appropriate terms by comparison to Eq. (43), and taking their ratio. Continuity of the metric and its derivatives across the neutron-star surface results in

$$\lambda = \lambda(C, y), \tag{47}$$

where C is the neutron-star compactness and y expresses a metric quantity and its derivative at R. It can be obtained by numerically integrating a second-order ordinary differential equation from the neutron-star center to its surface (Hinderer, 2008; Guerra Chaves and Hinderer, 2019).

Beyond the leading-order adiabatic quadrupolar tidal deformability, higher-order terms take into account higher-multipolar electric-type and magnetic-type corrections in Eq. (43) (Binnington and Poisson, 2009; Damour and Nagar, 2009; Guerra Chaves and Hinderer, 2019), spin-tidal couplings to the neutron-star rotation (Landry and Poisson, 2015; Pani, Gualtieri, and Ferrari, 2015; Pani *et al.*, 2015; Landry, 2017; Abdelsalhin, Gualtieri, and Pani, 2018), and dynamical tides (Hinderer *et al.*, 2016; Steinhoff *et al.*, 2016; Schmidt and Hinderer, 2019; Pratten, Schmidt, and Hinderer, 2020; Gamba and Bernuzzi, 2023). Though these effects are partially (or fully, in some cases) included during analyses of gravitational-wave data, their influence is expected to be subdominant to λ for current-generation detectors.

VI. COMPACT BINARY MERGERS INVOLVING NEUTRON STARS

Neutron stars in compact binaries around other neutron stars or black holes can be observed through their gravitational-wave signal by the ground-based LIGO (Aasi *et al.*, 2015) and Virgo detectors (Acernese *et al.*, 2015) and electromagnetic emission. To date, the coalescence of two neutron-star binaries (Abbott *et al.*, 2017b, 2020a), three-neutron-star–black hole binaries (Abbott *et al.*, 2021b; Abac *et al.*, 2024) and further sub-$5M_\odot$ objects of interest (Abbott *et al.*, 2020b, 2023a) have been observed in gravitational waves. These observations have the potential to inform about the nuclear EOS.

Compact objects in binaries inspiral around each other, slowly emitting their binding energy in gravitational radiation. This long inspiral phase, observed for minutes, offers information about the neutron-star masses and spins. During the late stages of the coalescence and depending on the exact binary parameters, the neutron star gets tidally distorted owing to the tidal field of its companion. The degree of tidal deformation quantified through the tidal deformability depends on the EOS. Immediately after the merger of two neutron stars, the final remnant is not spherically symmetric, and thus it keeps emitting high-frequency gravitational radiation. The signal's properties depend on the nature of the remnant, which in turn depends on the binary parameters and the EOS. Figure 12 shows the gravitational-wave spectrum from neutron-star binary coalescences with different EOSs. In this section we discuss the phenomenology, physics, and observational signatures of compact binary coalescences in both gravitational and electromagnetic radiation. For a more in-depth discussion of the qualitative and quantitative features of compact binary mergers, see Baiotti and Rezzolla (2017), Shibata and Hotokezaka (2019), Radice, Bernuzzi, and Perego (2020), and Kyutoku, Shibata, and Taniguchi (2021).

A. Compact binary inspirals

Compact binaries consisting of neutron stars and/or black holes emit their binding energy in gravitational waves and inspiral toward each other until their eventual merger. Sourced to leading order by the time-varying orbital quadrupole moment (Peters and Mathews, 1963; Peters, 1964; Blanchet, 2014), the rate of emission increases rapidly as the compact objects inspiral and speed up, leading to a runaway process. Current ground-based detectors are sensitive to signals above a gravitational-wave frequency of ∼20 Hz, corresponding to the end of the inspiral and merger of compact objects with masses $\lesssim \mathcal{O}(10^2)M_\odot$.

During the inspiral stage, the compact object velocities u are low compared to the speed of light. The post-Newtonian (PN) description, therefore, expands all quantities in powers of u. Terms proportional to u^{2N} compared to the leading-order term are labeled as NPN corrections. In the frequency domain and under the stationary phase approximation (Droz *et al.*, 1999), the gravitational-wave signal $\tilde{h}(f)$ from a compact binary with masses $M_1 > M_2$ and spins $\vec{\chi}_1$ and $\vec{\chi}_2$ is

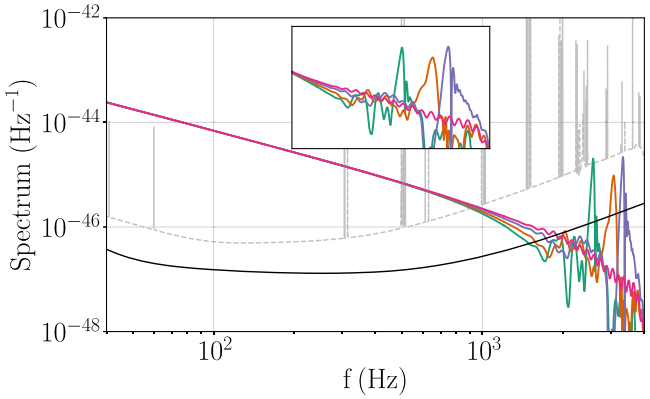

FIG. 12. Spectrum of neutron-star binary signals for different EOSs (colored lines). Binaries enter the LIGO or Virgo frequency band at a gravitational-wave frequency of ∼20 Hz at ∼1000 km apart. Over the ensuing 2 to 3 min they emit their binding energy in gravitational radiation and inspiral. Tidal deformation speeds up the inspiral and imprints the EOS in the waveform in frequencies $\gtrsim$300 Hz. The neutron stars merge at around 1000–1500 Hz, after which postmerger emission is dominated by a spectral peak whose frequency is a strong function of the EOS (Sec. VI.D). Inspiral data were created with `IMRPhenomD_NRTidalv2` (Dietrich *et al.*, 2019), while merger and postmerger data correspond to numerical simulations from Torres-Rivas *et al.* (2019). The GW170817 (Abbott *et al.*, 2021a) and design sensitivity (Abbott *et al.*, 2018a) power spectral density for LIGO Livingston (Aasi *et al.*, 2015) are shown in dashed gray and solid black lines, respectively. Inset: the high-frequency portion of the four signals.

$$\tilde{h}(f) = \mathcal{A}\frac{(\mathcal{M}f)^{5/6}f^{-2}}{D_L}e^{i\Psi(f)}, \tag{48}$$

where $\mathcal{A}$ is a constant that depends on the binary orientation, $\mathcal{M}$ is the binary chirp mass, f is the frequency, D_L is the luminosity distance to the binary, and $\Psi(f)$ is its phase. The signal phase can be obtained through energy balance: the loss in binary binding energy is carried away by gravitational waves. Then the derivative of the binary orbital frequency F is (in the time domain)

$$\frac{dF}{dt} = \frac{dE}{dt}\frac{dF}{dE}, \tag{49}$$

where dE/dt is the rate of energy emission, which can be obtained through the quadrupole formula, and $1/(dE/dF)$ is the binding energy derivative with respect to frequency, which corresponds to Kepler's law.

Calculating the gravitational-wave phase for high PN order and transforming to the frequency domain yields (Buonanno *et al.*, 2009; Blanchet, 2014)

$$\Psi(f) = 2\pi f t_c + \phi_c - \frac{\pi}{4} + \frac{3}{128\eta u^5}\{1 + f(\eta)u^2 + (4\beta - 16\pi)u^3 + [g(\eta) + \sigma]u^4 + \cdots\}. \tag{50}$$

In Eq. (50) $u \equiv (\pi M_T f)^{1/3}$, $M_T = M_1 + M_2$ is the total mass, $\eta = M_1M_2/M_T^2$ is the symmetric mass ratio, t_c is the time of

coalescence, and ϕ_c is the phase of coalescence. The coefficients β and σ denote terms proportional to the spin and spin squared, respectively. The leading-order term in Eq. (50) dominates the overall signal evolution, especially for low-mass compact binaries such as those involving neutron stars. Its form leads to the definition of the chirp mass $\mathcal{M} \equiv M_T \eta^{3/5}$.

The leading-order inspiral evolution and Kepler's law allow us to obtain some first estimates of the phenomenology of the signal. When observed from a frequency f_0, the inspiral lasts for

$$T_{\rm ins} = \frac{5}{256}\mathcal{M}^{-5/3}(\pi f_0)^{-8/3}, \tag{51}$$

suggesting that it is a strong function of the binary mass. For example, a $1.4 + 1.4M_\odot$ binary lasts for 1000(157)[53] s from 10(20)[30] Hz, while a $10 + 10M_\odot$ binary lasts for 38(6)[2] s with the same frequencies. Therefore, the long signal duration is the first indication of the detection of a low-mass, potentially neutron-star binary.

The signal phase and Eq. (50) prescribe to an excellent approximation which binary properties are measurable and how. As mentioned, the leading-order term depends on the binary chirp mass $\mathcal{M}$, whose statistical relative measurement accuracy reached $\mathcal{O}(10^{-4})$ for GW170817 at the frame of the detector (Abbott *et al.*, 2017b). Uncertainty in the source-frame binary chirp mass is instead dominated by the uncertainty in the distance or redshift used to convert between the two frames (Abbott *et al.*, 2019a).

A second mass parameter is needed in order to extract the individual component masses. The 1PN term in Eq. (50) introduces the binary symmetric mass ratio η. The equivalent mass ratio[5] $q \equiv M_2/M_1 < 1$ is measured to be significantly worse than the chirp mass at $\sim$(0.5–1) for GW170817 (Abbott *et al.*, 2019a). Further complicating the picture are the 1.5PN and 2PN terms, which introduce spin-orbit β and spin-spin σ terms that correlate the measurement of the mass ratio and spins. The latter is typically expressed through the effective spin

$$\chi_{\rm eff} = \frac{m_1\vec{\chi}_1 \cdot \hat{L} + m_2\vec{\chi}_2 \cdot \hat{L}}{m_1 + m_2}, \tag{52}$$

where $\hat{L}$ is the direction of the Newtonian orbital angular momentum. The effective spin is related to β in the equal-mass limit and conserved at the 2PN order (Racine, 2008). The mass-spin correlation means that an inference of the binary mass ratio and the component spins depends on assumptions about the neutron-star spins, as shown in Fig. 13 for GW170817 (Abbott *et al.*, 2019a). Imposing a low spin $\chi < 0.05$ motivated by Galactic neutron-star binary observations (Tauris *et al.*, 2017) leads to $m_1 \sim (1.36, 1.60)M_\odot$ and $m_2 \sim (1.16, 1.36)M_\odot$ at the 90% credible level (Abbott *et al.*, 2019a). An agnostic spin prior that extends to $\chi < 0.89$ instead leads to larger uncertainties: $m_1 \sim (1.36, 1.89)M_\odot$ and $m_2 \sim (1.00, 1.36)M_\odot$ at the 90% credible level.

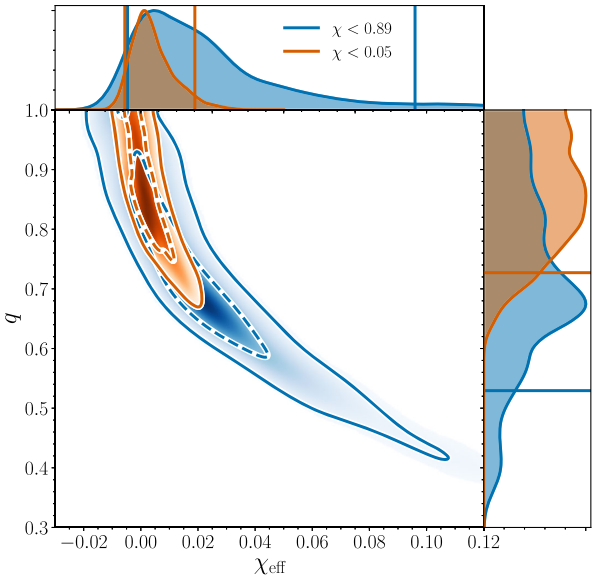

FIG. 13. Marginalized posterior for the mass ratio and effective spin of GW170817 showcasing the inherent mass-spin correlation of gravitational-wave inspiral measurements. Assuming that GW170817 shares spin properties similar to the Galactic neutron-star binaries restricts the spin to $\chi < 0.05$ and leads to improved mass ratio and component mass inference. For reference, a dimensionless spin of $\chi \sim 0.4$ approximately corresponds to a 1 ms neutron star. From Abbott *et al.*, 2019a.

Though GW170817 is consistent with the Galactic neutron-star binary population, the dependence on spin assumptions creates an inherent ambiguity, especially for binaries such as GW190425 (Abbott *et al.*, 2020a). At a total mass of $M \sim 3.4M_\odot$, GW190425 is more massive than GW170817 and Galactic observations whose total masses cluster around $\sim 2.7M_\odot$. Similar considerations apply to neutron-star–black hole observations regarding the appropriate spin assumptions for the neutron-star binary component and their impact on the inferred binary mass ratio. The expected spins of neutron-star binaries or neutron-star–black hole binaries are uncertain, and it is not clear whether they are representative of the low spins of Galactic binaries.

Absent from the leading-order phase terms is a strong imprint of the neutron-star EOS. Modulo resonant excitations of the neutron-star matter, the inspiral signal is dominated by the binary masses and spins.[6] Therefore, the signals emitted by two neutron stars is indistinguishable from the signal emitted by two black holes with the same mass and spin. Figure 12 shows that the signal spectrum for neutron-star binaries is

[5]This mass-ratio definition breaks the labeling degeneracy between the two neutron stars by identifying neutron star 1 as the most massive one.

[6]Spin induces a quadrupole moment on the neutron star that depends on the EOS and enters that gravitational-wave phase through the 2PN σ term (Poisson, 1998; Bohé *et al.*, 2015). However, since the term is proportional to the neutron-star spin squared and has a small numerical prefactor, it is in general considered to be negligible unless the neutron star has a large spin (Harry and Hinderer, 2018; Samajdar and Dietrich, 2020). Nonetheless, it is included in compact binary analyses and inference (Yagi and Yunes, 2013).

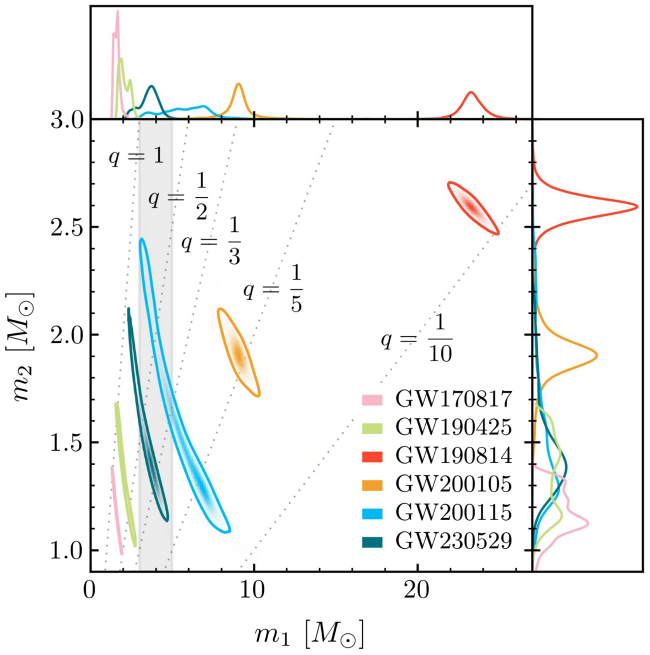

FIG. 14. Marginalized mass posteriors for the confident sub-$3M_\odot$ gravitational-wave detections. The dashed lines denote a constant mass ratio, and the shaded region corresponds to $m_1 \in [3, 5]M_\odot$, the purported mass gap between neutron stars and black holes. All analyses allow for large spins and hence represent agnostic results. Adapted from Abac *et al.*, 2024.

identical up to gravitational-wave frequencies of ∼200 Hz for different EOSs. A similar conclusion holds for the gravitational-wave phase and neutron-star–black hole binaries.

B. Mass observations

Mass measurements of sub-$3M_\odot$ compact objects in binaries are possible using gravitational-wave information. Figure 14 shows the one- and two-dimensional marginalized posteriors for the masses of confidently detected relevant events. Figure 14 and the following discussion remain agnostic about the neutron-star spins, so they are conservative. Quoted intervals correspond to 90% credibility.

- At a total mass of $2.77^{+0.22}_{-0.05}M_\odot$, GW170817 (Abbott *et al.*, 2017b) is consistent with the Galactic neutron-star binary population (Tauris *et al.*, 2017). GW170817 is also the only event on this list with informative tidal constraints.
- The second likely neutron-star binary, GW190425 (Abbott *et al.*, 2020a), has a total mass of $3.4^{+0.3}_{-0.1}M_\odot$. It is thus more massive than the Galactic neutron-star binary population. Though the components of GW190425 are individually consistent with neutron stars, their combination in a neutron-star binary is novel and shows that such massive neutron stars form compact binaries and merge.
- The secondary component of GW190814 (Abbott *et al.*, 2020b) at $2.59^{+0.08}_{-0.09}M_\odot$ is the most massive neutron star or the least massive black hole known (Essick and Landry, 2020; Fattoyev *et al.*, 2020; Li, Sedrakian, and Weber, 2020; Sedrakian, Weber, and Li, 2020; Tan, Noronha-Hostler, and Yunes, 2020; Bombaci *et al.*, 2021; Dexheimer *et al.*, 2021; Tews *et al.*, 2021).
- GW200105 and GW200115 (Abbott *et al.*, 2021b) were the first mixed neutron-star–black hole binaries identified. The secondary components at $1.9^{+0.3}_{-0.2}M_\odot$ and $1.5^{+0.7}_{-0.3}M_\odot$, respectively, are consistent with Galactic neutron-star masses (Alsing, Silva, and Berti, 2018) and nuclear physics expectations.
- GW230529 (Abac *et al.*, 2024) originates from the merger of a likely neutron-star secondary with a $2.5M_\odot$–$4.5M_\odot$ primary compact object. This mass range corresponds to the observational low-mass gap between neutron stars and black holes, which is denoted by the shaded vertical band in Fig. 14. Depending on astrophysical assumptions, GW230529 could be a neutron-star–black hole binary with a nonspinning $\sim 4M_\odot$ primary or a heavy neutron-star binary with a spin that is negatively aligned with the orbit.

The gravitational-wave data alone guarantee that the detected objects are compact neutron stars or black holes and primarily constrain the compact object masses. However, a definitive determination of the nature of the compact objects would require detection of tidal effects, i.e., a lower limit on Λ. Since Λ rapidly decreases for more massive neutron stars or more asymmetric binaries, lower limits on the tides from $\gtrsim 1.6M_\odot$ objects are not expected with current or near-future detectors (Yang, East, and Lehner, 2018; Chen *et al.*, 2020; Brown, Capano, and Krishnan, 2022). In the absence of a definitive classification from gravitational-wave data for $\gtrsim 1.6M_\odot$ compact objects, external input about the maximum neutron-star mass is required. The most basic classification hinges on the fact that causality limits neutron-star masses to $\lesssim 3M_\odot$ (Rhoades and Ruffini, 1974; Kalogera and Baym, 1996).

The first option is comparing masses inferred from gravitational-wave data to the inferred maximum mass from galactic pulsars $\gtrsim 2M_\odot$ (Antoniadis *et al.*, 2016; Alsing, Silva, and Berti, 2018; Farr and Chatziioannou, 2020), though such analyses are based on a heterogeneous set of the observed pulsars with mass measurements and unquantified selection effects that depend on how each system was discovered and chosen for follow-up observations. Even then, galactic neutron-star masses are not representative of gravitational-wave observations. Galactic neutron-star binaries are clustered around $1.4M_\odot$ (Tauris *et al.*, 2017), while the entire pulsar mass distribution has a sharp peak at $1.4M_\odot$ and a secondary peak at $\sim 1.7M_\odot$ (Antoniadis *et al.*, 2016). The mass distribution of neutron stars observed with gravitational waves is more broad, with no evidence at the moment of a strong peak at any value (Chatziioannou and Farr, 2020; Landry and Read, 2021; Abbott *et al.*, 2023b).

The second option is comparing masses inferred from gravitational-wave data to the maximum TOV mass, which is again $\sim 2M_\odot$–$2.5M_\odot$ (Legred *et al.*, 2021; Miller *et al.*, 2021; Raaijmakers *et al.*, 2021; Koehn *et al.*, 2024). Inference of the TOV mass is based on a multitude of astronomical data and nuclear experiment and/or calculations that inform the neutron-star EOS at various densities. Since the maximum TOV mass depends primarily on the highest neutron-star

densities $\sim 5n_0$–$6n_0$, an EOS model is required to effectively translate constraints across scales, introducing a model dependence due to intradensity correlations in the models (Legred *et al.*, 2022). Moreover, such a comparison implicitly assumes that neutron stars up to the maximum mass allowed by nuclear physics are astrophysically produced (Essick and Landry, 2020), which is unclear.

These arguments hinge on neutron stars and black holes having nonoverlapping mass distributions. If low-mass black holes of potential primordial origin (Carr and Hawking, 1974) exist, the overlapping neutron-star and black hole populations could be distinguished based on their tidal properties (Chen and Chatziioannou, 2020). Searches for sub-$1M_\odot$ compact objects have not yielded confident detections (Abbott *et al.*, 2019c, 2023c; Nitz and Wang, 2022), but if such compact objects and binaries exist, the large expected tidal deformability of neutron stars in this mass range would make their classification more straightforward (Golomb *et al.*, 2024).

Finally, beyond considerations about tidal inference and nuclear physics input, the mass distribution of all objects in compact binaries $\lesssim 10M_\odot$ is not smooth (Fishbach, Essick, and Holz, 2020; Farah *et al.*, 2022; Abbott *et al.*, 2023b). The rate of $\lesssim 2M_\odot$ compact objects is more steep as a function of mass than the rate of $\gtrsim 5M_\odot$ compact objects, with an underdensity between them starting at $\sim 2.4M_\odot$. Under the assumption of nonoverlapping neutron-star and black hole distributions, such a feature could signal the transition between the two populations. Though its location also roughly corresponds to the neutron-star–black hole mass gap at $3M_\odot$–$5M_\odot$, the gravitational-wave rate is more consistent with an underdensity than a completely empty gap (Abbott *et al.*, 2023b).

C. Late inspiral and tidal deformation

Once energy loss in gravitational waves brings the compact objects close enough, tidal interactions become important. A neutron-star component will be tidally deformed by the external field created by its companion. In a neutron-star binary, this process acts twice, once on each neutron star, while in a neutron-star–black hole binary, only the neutron star is deformed. The leading-order deformation is the adiabatic, quadrupole effect described in Sec. V.B. In this case the deformation is coherent with the binary in the sense that the tidal bulge raised on the deformed neutron star faces its companion and the tidally induced quadrupole moment adds to the dominant orbital quadrupole moment that sources the radiation. In what follows we consider the tidal effect on a neutron star with mass M_1 and tidal deformability λ_1 by its companion with mass M_2. If the companion is a neutron star as well, its impact is additive with $1 \leftrightarrow 2$.

Physically, the tidal deformation results in two effects, both of which remove energy from the system and accelerate its inspiral. First, the energy required to deform an initially spherically symmetric star is removed from the binary binding energy. Overall,

$$E(F) = E_{\rm PP}(F) + E_{\rm tide}(F), \tag{53}$$

where

$$E_{\rm PP}(F) = -\tfrac{1}{2} M_T \eta v^2 [1 + \mathcal{O}(v^2)] \tag{54}$$

is the point-particle binding energy (Buonanno *et al.*, 2009; Blanchet, 2014), with $v = (2\pi M_T F)^{1/3}$. The tidal contribution is (Flanagan and Hinderer, 2008; Hinderer *et al.*, 2010)

$$E_{\rm tide}(F) \sim Q_{ij}\mathcal{E}_{ij} = -\frac{1}{2} M_T \eta v^2 \left[-9 \frac{M_2}{M_1} \frac{\lambda_1}{M_T^5} v^{10} + \mathcal{O}(v^{11}) \right], \tag{55}$$

which lowers (in absolute value) the total energy. Second, gravitational-wave emission is sourced by time-varying quadrupole moments. Though the orbital quadrupole dominates the emission (Buonanno *et al.*, 2009; Blanchet, 2014),

$$\dot{E}_{\rm PP}(F) = -\tfrac{32}{5} \eta^2 v^{10} [1 + \mathcal{O}(v^2)], \tag{56}$$

the tidally induced quadrupole causes additional coherent energy emission (Flanagan and Hinderer, 2008; Hinderer *et al.*, 2010)

$$\dot{E}_{\rm tide}(F) \sim \dot{\mathcal{Q}}_{ij}^2 = -\frac{32}{5} \eta^2 v^{10} \left[6 \frac{M_1 + 3M_2}{M_1} \frac{\lambda_1}{M_T^5} v^{10} + \mathcal{O}(v^{11}) \right], \tag{57}$$

such that the total energy emission is enhanced

$$\dot{E}(F) = \dot{E}_{\rm PP}(F) + \dot{E}_{\rm tide}(F). \tag{58}$$

The tidally updated energy [Eq. (53)] and energy emission [Eq. (58)] together with Eq. (49) result in a 5PN (u^{10} relative to the leading-order term) additive tidal phase term in Eq. (50),

$$\Psi_\Lambda(f) = \frac{3}{128\eta u^5} \left(-\frac{39}{2} \tilde{\Lambda} u^{10} \right), \tag{59}$$

where (Favata, 2014)

$$\tilde{\Lambda} \equiv \frac{16}{3} \frac{(M_1 + 12M_2) M_1^4 \Lambda_1}{(M_1 + M_2)^5} = \frac{16}{3} \frac{(M_1 + 12M_2)}{(M_1 + M_2)^5} \frac{\lambda_1}{M_1} \tag{60}$$

is the leading-order and best-measured tidal term in the phase. Numerically, for a neutron-star binary, the energy effect in Eq. (53) is a factor of 2:1 (equal masses) to 3:1 (unequal masses) larger than the energy emission effect in Eq. (58). This discussion neglects a number of point-particle and finite-size terms that are included in modern waveform models (Vines, Flanagan, and Hinderer, 2011; Bernuzzi *et al.*, 2015; Hinderer *et al.*, 2016; Hotokezaka *et al.*, 2016; Dietrich, Bernuzzi, and Tichy, 2017; Nagar *et al.*, 2018; Dietrich *et al.*, 2019; Dietrich, Samajdar *et al.*, 2019; Matas *et al.*, 2020; Thompson *et al.*, 2020; Gamba, Bernuzzi, and Nagar, 2021; Steinhoff *et al.*, 2021; Gamba *et al.*, 2023; Gonzalez *et al.*, 2023; Abac, Dietrich *et al.*, 2024); see Dietrich, Hinderer, and Samajdar (2021) for a review. In addition, these calculations assume that the external tidal field varies slowly compared to the internal dynamical time of the perturbed neutron star (static tide as opposed to dynamical tides) and neglect any

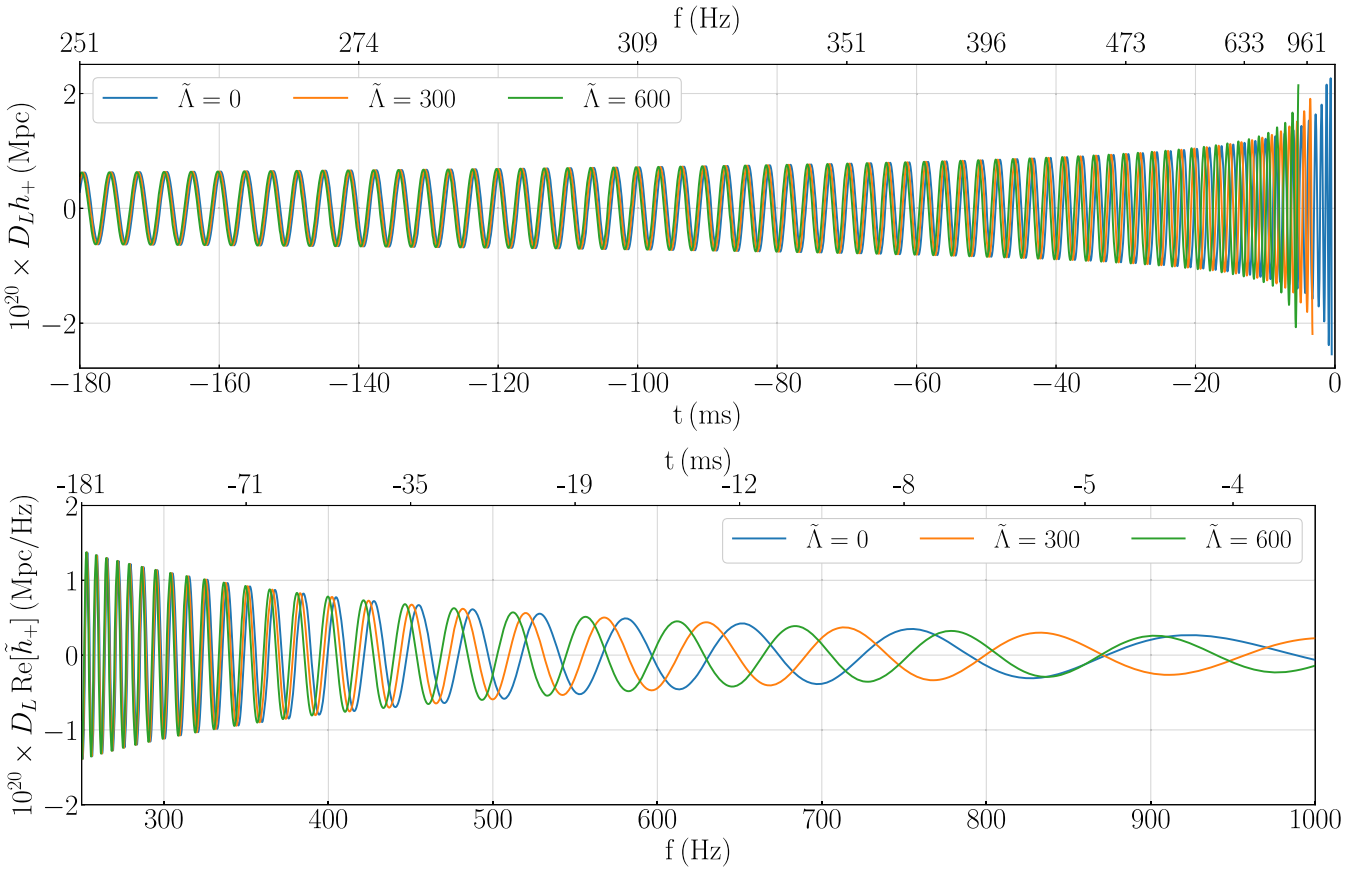

FIG. 15. Final inspiral stages of a neutron-star binary for different values of the tidal deformability. The waveform is plotted using `IMRPhenomD_NRTidalv2` (Dietrich *et al.*, 2019) for equal-mass, nonspinning neutron stars up to merger (the peak of the strain in the time domain) in the time domain (top panel) and frequency domain (bottom panel). The upper x axis denotes the corresponding frequency (top panel) and time (bottom panel) for the $\tilde{\Lambda} = 0$ binary. Tidal deformation speeds up the binary evolution. Adapted from Chatziioannou, 2020.

nonadiabatic or nonlinear effects (Pratten, Schmidt, and Hinderer, 2020).

The sign of the phase term in Eq. (59) again suggests that tides speed up the binary inspiral and that the binary accumulates fewer radians before merger. Figure 15 shows the final dozens of cycles of the late inspiral of equal-mass, nonspinning neutron-star binaries with different values of the tidal deformability in the time and in the frequency domain. Tides affect the gravitational-wave phase evolution only during the last ∼100 ms before merger and for frequencies above ∼300 Hz, as expected from a high-PN-order term. A larger value of the tidal deformability causes the phase evolution to speed up and the binary to reach merger earlier. This phase difference is the main tidal observable for neutron-star binary signals. For a typical binary, with $\tilde{\Lambda} \sim 500$ the accumulated dephasing with respect to the point-particle limit up to the contact frequency is ∼10 rad.

In principle, the tidal contribution to the phase can be added to any point-particle post-Newtonian waveform model using Eq. (59). In practice, there are conceptual and practical issues. In this context, numerical relativity simulations (Baumgarte and Shapiro, 2021) play an important role for two reasons. First, they are needed to calibrate and validate the baseline point-particle waveform model. To this aim vacuum simulations are used since they can achieve high precision, with effective dephasing at merger well below 1 rad (Nagar *et al.*, 2018; Boyle *et al.*, 2019; Matas *et al.*, 2020). Second, simulations are needed to understand to what extent matter effects can truly be absorbed into $\tilde{\Lambda}$ (Steinhoff *et al.*, 2016; Kuan and Kokkotas, 2023). For example, various recent studies have studied the possible role of dynamical tides in neutron-star mergers, but it is unclear that current simulations are sufficiently accurate to reliably extract these effects (Steinhoff *et al.*, 2021; Gamba and Bernuzzi, 2023). Figure 16 shows a comparison between various analytical waveforms from the `TEOBResumS` family (Nagar *et al.*, 2018) and numerical relativity data. While excellent agreement is found over most of the inspiral, waveforms start to deviate from the numerical prediction in the last gravitational-wave cycle. However, this is precisely the phase of the dynamics in which matter effects are the strongest (Damour, Nagar, and Villain, 2012). The estimated numerical error, shown as a gray band in Fig. 16, is also large at this point.

Numerical simulations of tidally interacting neutron stars in binaries employ eccentricity reduced initial data, high-order numerical schemes, and high resolutions (Bernuzzi *et al.*, 2012; Radice, Rezzolla, and Galeazzi, 2014; Bernuzzi and

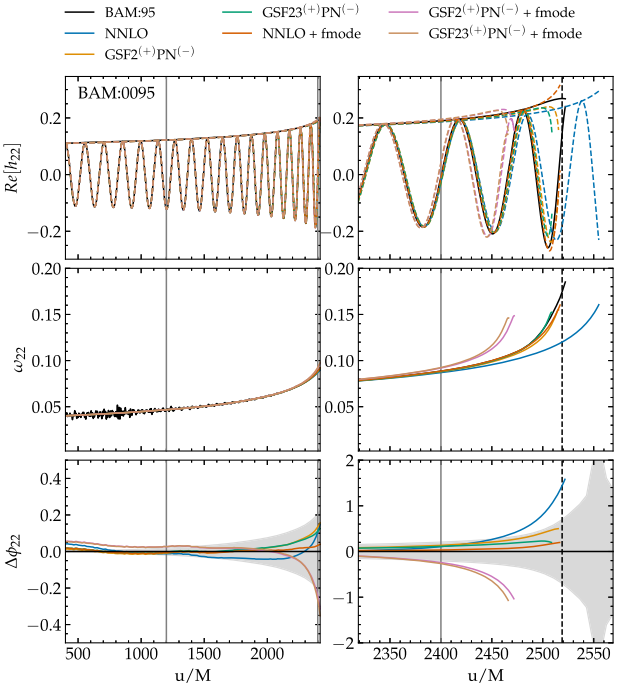

FIG. 16. Comparison of different analytical gravitational waveforms within the `TEOBResumS` family with numerical relativity data of inspiraling neutron stars. From top to bottom, the panels show the real part of the strain $\mathrm{Re}[h_{22}]$ (corresponding to the plus polarization), the instantaneous frequency of the signal ω_{22}, and the dephasing $\Delta\phi_{22}$ of different models compared to the numerical relativity simulation "`BAM:95`. All quantities are shown for the $(\ell = 2, m = 2)$ mode as a function of the retarded time u/M. From Gamba and Bernuzzi, 2023.

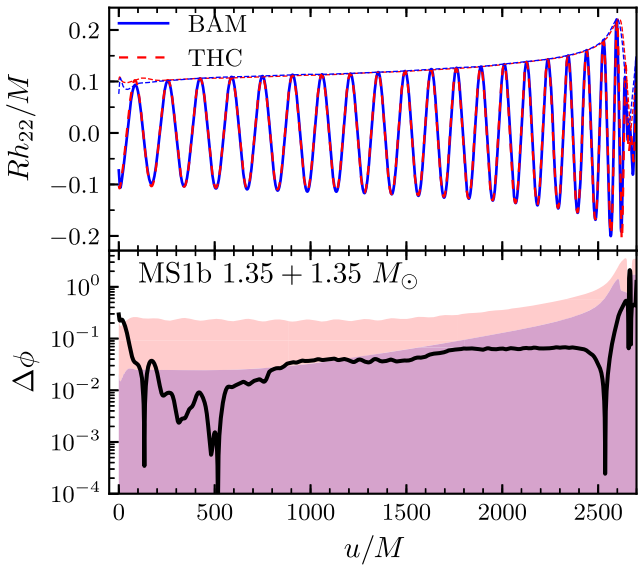

FIG. 17. Cross validation of the `BAM` and `THC` numerical relativity codes for binary neutron-star merger simulations. Top panel: real part of the strain Rh_{22}/M (corresponding to the plus polarization). Bottom panel: dephasing $\Delta\phi$ between the `THC` and `BAM` codes (black line) as well as the uncertainty bands independently estimated for the two simulations (colored bands). All quantities are shown for the $(\ell = 2, m = 2)$ mode as a function of the retarded time u/M. From Nagar *et al.*, 2018.

Dietrich, 2016; Dietrich, Bernuzzi, and Tichy, 2017; Kiuchi *et al.*, 2017; Doulis *et al.*, 2022). Neutron-star merger simulations are now routinely performed with temperature- and composition-dependent EOS, starting with initial conditions corresponding to two cold β-equilibrated stars (Sekiguchi *et al.*, 2011). However, interpolation errors for tabulated EOSs are too large for high-precision models of tidally interacting neutron stars, so simplified zero-temperature EOS models are typically employed. This is justified because thermal effects are expected to be negligible in the inspiral (Lai, 1994). Moreover, smoothness of density and pressure profiles in the stars are necessary for the codes to achieve high accuracy (Foucart, Duez *et al.*, 2019; Knight *et al.*, 2024). For these reasons matter is described using smooth, barotropic EOSs, i.e., using piecewise polytropic (Shibata, Taniguchi, and Uryu, 2005; Read *et al.*, 2009; O'Boyle *et al.*, 2020) or spectral models (Lindblom, 2010), augmented with an ideal-gas prescription to approximately include thermal effects (Bauswein, Janka, and Oechslin, 2010; Raithel, Özel, and Psaltis, 2019). Simulations aiming to model the postmerger evolution or the multimessenger signals from neutron-star mergers employ more sophisticated EOS models (Sekiguchi *et al.*, 2011). The numerical uncertainty in binary inspiral simulations is typically quantified in terms of phase errors at mergers. High-resolution simulations achieve subradian accuracy over approximately ten orbits (20 gravitational-wave cycles). Figure 17 shows a comparison of `BAM` and `THC`, two independently developed and commonly employed numerical relativity codes. The two codes are in excellent quantitative agreement. Moreover, the independently estimated uncertainty bands overlap, suggesting that simulations of tidally interacting binaries are reliable.

Despite the high PN term, $\tilde{\Lambda}$ is measurable at current sensitivity owing to both the large prefactor in Eq. (59) and the fact that nuclear EOSs predict $\tilde{\Lambda} \sim \mathcal{O}(10^2)$ in the relevant mass range. Figure 18 shows the marginal posterior for the mass ratio q and $\tilde{\Lambda}$ for GW170817 and for different assumptions about the neutron-star spin (Abbott *et al.*, 2019a). The two parameters are moderately correlated ($\tilde{\Lambda}$ has a much stronger correlation with the time of coalescence t_c that enters the phase at 4PN; see Eq. (50). Regardless of spin, the GW170817 data place an upper limit on the tidal deformation of $\lesssim 700$ at the 90% credible level (Abbott *et al.*, 2019a). Zero values of $\tilde{\Lambda}$ are disfavored, but they are not ruled out if spins are allowed to be large. Higher-order tidal terms, and hence Λ_1 and Λ_2 individually, were not measured. Consistent constraints were obtained with different waveform models, suggesting that they are robust against waveform systematics (Abbott *et al.*, 2019a).

No competitive tidal constraints were achieved for GW190425 or any of the observed neutron-star–black hole signals. Beyond their lower signal-to-noise ratio, this is also because the tidal imprint is much weaker for more massive neutron stars ($\Lambda \sim m^{-6}$) and more unequal-mass binaries ($\tilde{\Lambda} \sim q^4$). Overall, among sub-$3M_\odot$ gravitational-wave observations, only GW170817 resulted in informative constraints on tidal effects.

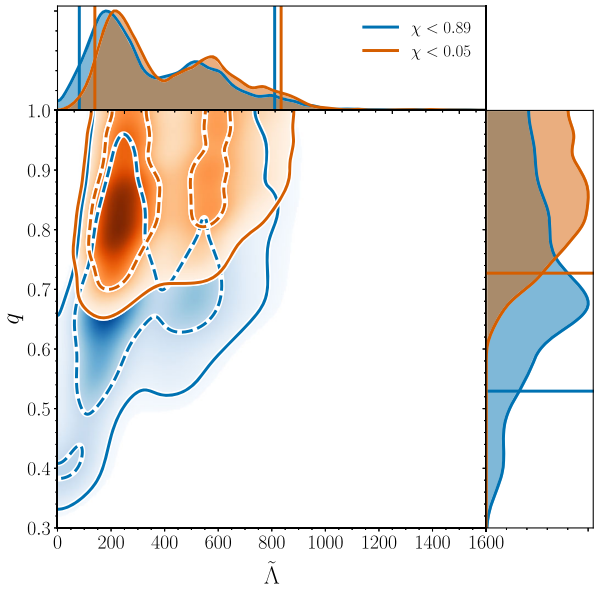

FIG. 18. Marginalized posterior for the mass ratio q and the tidal parameter $\tilde{\Lambda}$ of GW170817 showing the mild correlation between mass ratio and tides. The two posteriors correspond to the low and high spin assumptions of Fig. 13. From Abbott *et al.*, 2019a.

Translating the $\tilde{\Lambda}$ constraints of Fig. 18 to constraints on the neutron-star radius requires additional steps, such as the use of equation-of-state-independent relations (Maselli *et al.*, 2013; Yagi and Yunes, 2016, 2017; Annala *et al.*, 2018; Chatziioannou, Haster, and Zimmerman, 2018; De *et al.*, 2018; Raithel, Özel, and Psaltis, 2018; Zhao and Lattimer, 2018; Carson *et al.*, 2019; Chatziioannou and Han, 2020) and generic equation-of-state models (Read *et al.*, 2009; Lindblom, 2010; Steiner, Lattimer, and Brown, 2010; Lindblom and Indik, 2012, 2014; Alford, Han, and Prakash, 2013; Raithel, Özel, and Psaltis, 2016; Carney, Wade, and Irwin, 2018; Tews *et al.*, 2018; Landry and Essick, 2019; Dietrich *et al.*, 2020; Essick, Landry, and Holz, 2020; Landry, Essick, and Chatziioannou, 2020; O'Boyle *et al.*, 2020). Though these steps bring in their own uncertainties and model dependence (Greif *et al.*, 2019; Legred *et al.*, 2022), it is generally expected that tidal measurements achieved with gravitational-wave observations will constrain the nuclear EOS for densities $\sim 2n_0$–$3n_0$ (Legred *et al.*, 2021, 2024; Koehn *et al.*, 2024). Nonetheless, the $\tilde{\Lambda}$ upper limit for GW170817 implies that the radius of a $1.4M_\odot$ neutron star is $R_{1.4} \lesssim 13.5$ km (Abbott *et al.*, 2017b, 2018b, 2019a) at the 90% level; see Chatziioannou (2020) for a review.

Though current constraints on GW170817 are robust (Abbott *et al.*, 2019a), systematic uncertainties arising from incomplete knowledge of the two-body problem in general relativity might impact constraints for future detections with a higher signal-to-noise ratio (SNR). Numerical relativity simulation phase uncertainty grows rapidly in the last few gravitational-wave cycles, when the stars come into contact. Numerical errors from the numerical relativity simulations alone dominate over statistical uncertainty in the measurement of tidal parameters from observations for SNRs $\gtrsim 80$ (Gamba *et al.*, 2021; Read, 2023). Additional uncertainties arise for semianalytic waveform models that, as previously discussed, start to deviate from numerical relativity data and from each other shortly before merger. In other words, while current models are adequate for GW170817 (SNR $\simeq 32$), systematic uncertainties might dominate future events (Kunert *et al.*, 2022), particularly once next-generation detectors, such as Cosmic Explorer (Reitze *et al.*, 2019) and the Einstein Telescope (Punturo *et al.*, 2010a) come online. As such, the development of better simulations and waveform models is urgent. To this aim new numerical schemes, such as discontinuous Galerkin methods (Radice and Rezzolla, 2011; Bugner *et al.*, 2016; Hébert, Kidder, and Teukolsky, 2018; Dunham *et al.*, 2020; Tichy *et al.*, 2023; Dumbser *et al.*, 2024) are being explored. Discontinuous Galerkin methods are particularly interesting because they unify spectral and finite-volume methods. As such, they are able to achieve exponential convergence in regions where the solution is smooth while also being able to capture sharp features, such as shocks or the surfaces of the stars; see Hesthaven and Warburton (2007) for a general introduction on these methods. The first binary neutron-star merger simulations with discontinuous Galerkin methods were recently presented by Deppe *et al.* (2024).

D. Merger and postmerger

After a tidally accelerated late inspiral, the compact binary reaches gravitational-wave frequencies $\gtrsim$1000 Hz and the merger stage. Even though this stage is accompanied by a large emission of gravitational energy, its high frequency places it in a region where the sensitivity of ground-based detectors rapidly deteriorates (the power spectral densities in Fig. 12 increase as f^2 above 1000 Hz). No $\gtrsim$1000 Hz power has been unambiguously detected for any of the currently observed signals. However, as we later discuss, this phase of evolution is most consequential for the electromagnetic counterparts to mergers. Moreover, the detection of the postmerger kilohertz gravitational-wave signal for compact binaries is a key science goal for next-generation gravitational-wave experiments, such as Cosmic Explorer (Reitze *et al.*, 2019), the Einstein Telescope (Punturo *et al.*, 2010a), and NEMO (Ackley *et al.*, 2020); see Bernuzzi (2020) for a review of the postmerger GW signal from binary neutron-star systems). The merger morphology and subsequent system evolution is qualitatively different for neutron-star and mixed neutron-star–black hole binaries; we therefore discuss each separately in the review.

E. The outcome of neutron-star binary mergers

The outcome of a binary neutron-star merger changes qualitatively depending on the parameters of the binary, with the total binary mass giving the leading-order effect (Shibata, 2016; Shibata *et al.*, 2017; Radice, Bernuzzi, and Perego, 2020). Because general relativity has no intrinsic mass scale, it is the EOS that provides one. This is typically taken to be the maximum gravitational mass of nonrotating neutron stars supported by the EOS, $M_{\max}$, obtained by solving the TOV equations. In other words, the merger outcome depends, to

leading order, on $M_T/M_{\max}$, where $M_T = M_1 + M_2$ is the total binary mass at infinite separation. We emphasize that the fact that the reference mass is taken to be that of a nonrotating, cold neutron star does not mean that rotation and finite-temperature effects, which are included in the simulations, are unimportant. These dependencies are absorbed in dimensionless values of $M_T/M_{\max}$ that separate different merger outcomes.

- If $M_T/M_{\max} \gtrsim 1.4$, then the merger results in prompt black hole formation (Shibata, Taniguchi, and Uryu, 2005; Hotokezaka *et al.*, 2011; Bauswein, Baumgarte, and Janka, 2013). This scenario is the most likely for GW190425 owing to its high total mass (Abbott *et al.*, 2020a). Gravitational-wave emission is characterized in this case by the $\gtrsim$4 kHz ringdown radiation of the black hole, which is prohibitively high in frequency for current detectors but might be accessible with next-generation detectors (Dhani *et al.*, 2024). The resulting gravitational-wave sigal is depicted as a pink line in Fig. 12.
- If $1.2 \lesssim M_T/M_{\max} \lesssim 1.4$, then the merger remnant is said to be a *hypermassive neutron star* because it cannot be supported by uniform rotation, unlike *supramassive neutron stars*, which are discussed later. Hypermassive neutron stars are supported by differential rotation. They can collapse owing to the loss of angular momentum to gravitational waves early postmerger, when gravitational-wave losses are most intense, i.e., within ~20 ms (short-lived remnants) (Bernuzzi *et al.*, 2016; Zappa *et al.*, 2018). If this does not happen, the collapse can be triggered when turbulent viscosity erases the differential rotation. This is expected to occur on a longer timescale of a few hundred milliseconds (long-lived remnants). See Radice, Bernuzzi, and Perego (2020) for a detailed discussion. The mass threshold separating short- and long-lived hypermassive neutron stars is presently unknown.

  The typical gravitational-wave signals produced by such remnants are depicted in green, orange, and purple in Fig. 12. Even though this scenario is the most likely one for GW170817 (Margalit and Metzger, 2017), no signal was detected (Abbott *et al.*, 2017c, 2019a). Numerical simulations suggest that the detector sensitivity was a factor of $\gtrsim$3 too low, and such a signal could be detected once LIGO achieves sensitivities $\gtrsim$2 to 3 over its design sensitivity (Torres-Rivas *et al.*, 2019).
- If $1 \lesssim M_T/M_{\max} \lesssim 1.2$, then the merger remnant is called a supramassive neutron star. Supramassive neutron stars are supported against gravity by the combined effects of pressure and centrifugal forces. Binaries in this mass range are expected to produce long-lived remnants that can collapse only after having lost angular momentum because of gravitational waves and/or magnetized winds. The associated timescale for collapse is highly uncertain and could range from a few seconds to hours (Radice, Perego, Bernuzzi, and Zhang, 2018). Shorter survival times are expected for the more massive binaries. In addition to the gravitational waves produced shortly after merger by the deformed massive neutron-star remnant, very long-lived remnants might continue to emit low amplitude signals at frequencies $1\ \text{kHz} \lesssim f \lesssim 4\ \text{kHz}$ until they collapse. Such signals could be targeted with continuous-wave techniques (Riles, 2023). However, no detection was achieved for GW170817 or GW190425 (Abbott *et al.*, 2017c, 2019b; Grace, Wette, and Scott, 2024).
- If $M_T/M_{\max} \lesssim 1$, then the merger results in the formation of a stable neutron star. This case appears to be unlikely since the typical mass of neutron-star binaries is $2.7M_\odot$, so the EOS must be extremely stiff or the binary mass must be extremely small for this case to occur. However, it cannot be completely ruled out (Piro, Giacomazzo, and Perna, 2017).

The threshold masses separating the different regimes are affected to subleading order by the mass ratio and spin of the remnants (Papenfort *et al.*, 2022), as well as other parameters of the EOS besides $M_{\max}$ and $C_{\max}$, that is, those describing finite-temperature and compositional effects, as well as the detailed behavior of pressure as a function of density (Radice, Perego, Bernuzzi, and Zhang, 2018). They are also only approximately known because systematic exploration of the long-term outcome of neutron-star binary mergers is beyond the capability of current simulation codes. One exception is the case of prompt collapse, which can be studied with relatively short simulations and is now well understood. We discuss this in detail in Sec. VI.E.1.

The $\mathcal{O}(10)$ ms signal emitted by massive neutron-star remnants provides the best chance of postmerger detection owing to its high total emitted energy. Even though the signal is complicated and likely depends on unresolved simulation physics, it exhibits certain morphological features whose origin and interpretation are considered robust (Zappa *et al.*, 2023; Espino *et al.*, 2024). The main feature of the signal is that it is dominated by a single spectral peak (see Fig. 12) whose frequency depends on the EOS and the system mass (Baiotti, 2019; Bauswein and Stergioulas, 2019; Bernuzzi, 2020). Subdominant features such as further spectral peaks have also been identified and interpreted in terms of the remnant dynamics (Bauswein and Stergioulas, 2015; Rezzolla and Takami, 2016).

Measurement of the peak frequency from postmerger data combined with a measurement of the binary total mass from inspiral data would yield a $\mathcal{O}(10\text{–}100)$ m radius measurement (Chatziioannou *et al.*, 2017; Bose *et al.*, 2018; Breschi, Carullo, and Bernuzzi, 2023; Criswell *et al.*, 2023). Moreover, since the hypermassive remnant probes higher densities than the premerger neutron stars, comparison between the premerger and post-merger data would probe potential high-density phase transitions (Bauswein *et al.*, 2019; Most *et al.*, 2019; Liebling, Palenzuela, and Lehner, 2021; Prakash *et al.*, 2021, 2024; Huang *et al.*, 2022; Kedia *et al.*, 2022).

Searches and inference for the postmerger signal are hampered by the signal's complicated morphology, which, unlike the premerger signal, cannot be described from first principles and analytical calculations. However, its short duration makes it ideal for morphologically independent analyses (Clark *et al.*, 2014, 2016; Chatziioannou *et al.*, 2017; Wijngaarden *et al.*, 2022; Criswell *et al.*, 2023; Tringali *et al.*, 2023) and phenomenological models based on

combinations of damped sinusoids (Breschi *et al.*, 2019; Tsang, Dietrich, and Van Den Broeck, 2019; Easter *et al.*, 2020; Soultanis, Bauswein, and Stergioulas, 2022). Ultimately, detection of a postmerger signal would yield unprecedented constraints on the neutron-star EOS (see Fig. 12), where signals from different EOSs are more diverse during the postmerger than the premerger. However, the sharply decreasing high-frequency sensitivity of ground-based detectors makes detection of a postmerger signal with the current generation of detectors unlikely unless another exceptionally nearby signal is detected.

1. Prompt black hole formation

The threshold for prompt collapse in binary neutron-star mergers has been studied by many groups (Shibata, Taniguchi, and Uryu, 2005; Hotokezaka *et al.*, 2011; Bauswein, Baumgarte, and Janka, 2013; Bauswein *et al.*, 2017; 2020, 2021; Zappa *et al.*, 2018; Köppel, Bovard, and Rezzolla, 2019; Tootle *et al.*, 2021; Kashyap *et al.*, 2022; Kölsch *et al.*, 2022; Papenfort *et al.*, 2022; Perego *et al.*, 2022; Çokluk, Yakut, and Giacomazzo, 2024). However, different researchers have used inconsistent definitions for what is a prompt collapse. The most commonly adopted definition, which is also the one we endorse, is that the collapse is prompt if the stars do not exhibit any sign of a centrifugal bounce after merger; see Köppel, Bovard, and Rezzolla (2019) for an alternative definition based on the time to collapse. In this case the maximum rest-mass density grows monotonically with time until black hole formation. This definition has two key advantages over the alternatives. First, it is gauge and slicing independent, meaning that it does not depend on the gauge chosen for the simulations, so it is well defined. Second and most importantly, the bounce is related to the ejection of matter and the generation of an electromagnetic counterpart (Sec. VI.E.2). Indeed, for comparable mass-ratio binaries $q \gtrsim 0.75$, mass ejection occurs only as a result of the postmerger bounce of the remnant and its subsequent evolution (Bauswein, Goriely, and Janka, 2013; Hotokezaka *et al.*, 2013; Radice, Perego, Hotokezaka *et al.*, 2018; Shibata and Hotokezaka, 2019). In the absence of a bounce, there are little to no ejecta. Since the main electromagnetic counterpart to binary neutron-star mergers, the kilonova, is due to the radioactive decay of the expelled material, the absence of ejecta implies the absence of an electromagnetic counterpart. As such, whether or not prompt collapse has occurred for a particular binary can be determined observationally when this definition is used. For more asymmetric binaries ($q \lesssim 0.75$), the secondary star in the binary is tidally disrupted prior to merger (Dietrich *et al.*, 2017; Bernuzzi *et al.*, 2020), potentially resulting in massive outflows even under prompt collapse.

Simulations have shown that, for equal-mass binaries, prompt collapse occurs if (Bauswein, Baumgarte, and Janka, 2013; Bauswein *et al.*, 2017; Kashyap *et al.*, 2022)

$$M > M_{\rm th} = k_{\rm th} M_{\rm max}, \tag{61}$$

where $k_{\rm th} = 1.2$–1.7, depending on the EOS. A typical value of $k_{\rm th}$ (adopted here) is ~ 1.4. Moreover, $k_{\rm th}$ strongly correlates with the compactness of the maximum-mass nonrotating neutron star, $C_{\rm max} = GM_{\rm max}/c^2 R_{\rm max}$, and is well fitted by

$$k_{\rm th} = a C_{\rm max} + b, \tag{62}$$

with $a = -3.36 \pm 0.20$ and $b = 2.35 \pm 0.06$.[7] Figure 19 shows a compilation of $k_{\rm th}$ estimates from different works in the literature as a function of $C_{\rm max}$ (left panel) and the resulting constraints on $R_{\rm max}$ (right panel). Each point in the left panel of Fig. 19 corresponds to a different EOS and/or to simulations by different groups. Although there is good qualitative agreement, there is a systematic offset between simulations employing approximate general relativity (Bauswein, Baumgarte, and Janka, 2013; Bauswein *et al.*, 2021) and those employing full general relativity (Hotokezaka *et al.*, 2011; Kashyap *et al.*, 2022). GW170817 had an electromagnetic counterpart, suggesting that $M_{\rm th} > M_{\rm GW170817} \simeq 2.74 M_\odot$. Pulsar observations suggest that $M_{\rm max} > 2.01 M_\odot$; see Sec. VII.B. These lower limits on $M_{\rm th}$, $M_{\rm max}$, and Eq. (62) result in a constraint on the radius of the maximum-mass neutron star, $R_{\rm max} > 9.8$ km. Similarly, the coefficient $k_{\rm th}$ strongly correlates with the modified compactness of the $1.6 M_\odot$ neutron star,

$$k_{\rm th} = a' C^*_{1.6} + b', \qquad C^*_{1.6} = \frac{GM_{\rm max}}{c^2 R_{1.6}}, \tag{63}$$

from which it is possible to derive a lower limit on $R_{1.6}$ of 10.9 km (Kashyap *et al.*, 2022).

Constraints on $R_{\rm max}$ and $R_{1.6}$ both neglect corrections on $M_{\rm th}$ owing to the mass ratio. However, these are smaller than the systematic errors in Eqs. (62) and (63), when $q \gtrsim 0.75$, while $M_{\rm th}$ decreases with $q \lesssim 0.75$ (Bauswein *et al.*, 2021; Kölsch *et al.*, 2022; Perego *et al.*, 2022). As such, these lower limits are conservative.

The impact of the mass ratio on the threshold for prompt collapse has been investigated by several groups (Bauswein *et al.*, 2021; Kölsch *et al.*, 2022; Papenfort *et al.*, 2022; Perego *et al.*, 2022). Although early studies proposed that $M_{\rm th}(q)/M_{\rm th}$ could be independent of the EOS (Bauswein *et al.*, 2021; Tootle *et al.*, 2021), a more systematic exploration by Perego *et al.* (2022) showed that $M_{\rm th}(q)/M_{\rm th}$ depends on the EOS. For example, while for some EOSs $M_{\rm th}(q)$ decreases monotonically with q, for others $M_{\rm th}(q)$ can initially grow as q is reduced from 1 before declining as q is further reduced. Perego *et al.* (2022) suggested that the dynamics of prompt collapse binaries changes qualitatively when $q \lesssim 0.75$. For $0.75 \lesssim q \leq 1$ the dynamics is similar to the $q = 1$ case: as the stars are about to merge, a black hole is formed at their collisional interface. Shortly thereafter, both stars are swallowed by the horizon and little to no material is ejected. Within this range of q, $M_{\rm th}$ changes by less than 2% compared to the $q = 1$ case. If $q \lesssim 0.75$, then the less massive component is tidally disrupted before merger and black hole formation is the result of accretion of matter onto the primary

[7] These relations were first discovered by Bauswein, Baumgarte, and Janka (2013), but we report the more accurate values computed by Kashyap *et al.* (2022) here.

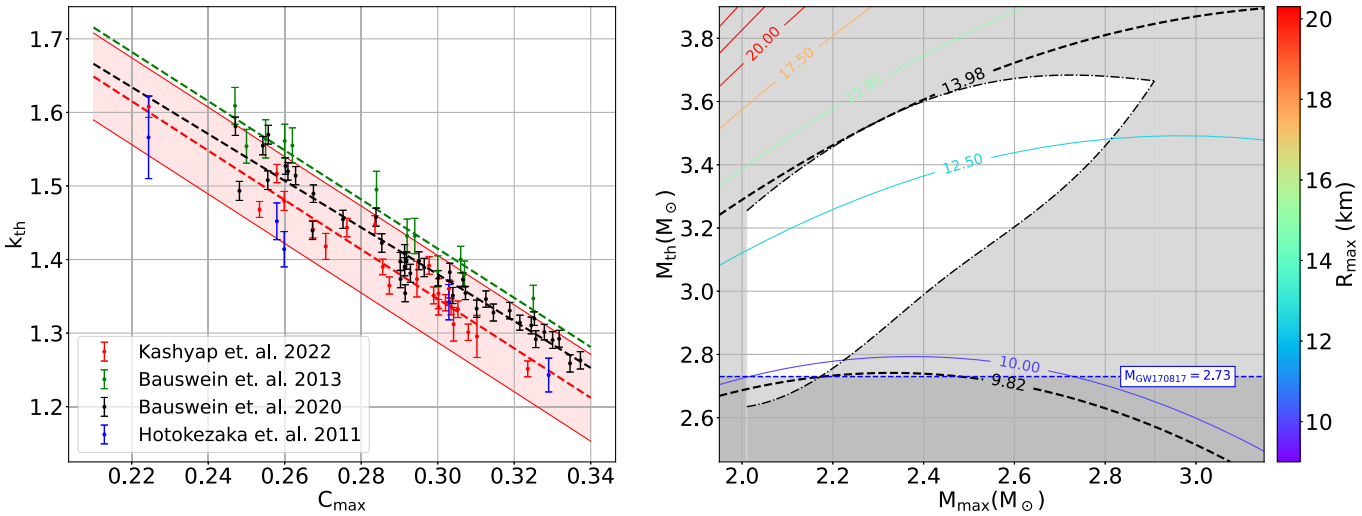

FIG. 19. Threshold for prompt collapse $k_{\rm th}$ as a function of the compactness of the maximum-mass neutron star (left panel) and the resulting constraints on $M_{\rm max}$ and $R_{\rm max}$. Left panel: $k_{\rm th}$ vs $C_{\rm max}$; see Eq. (61) for different EOSs. Different colors show the results from different groups. The dashed lines are fits to the data using Eq. (62), the red shaded area is the 90% uncertainty band for the intercept in the fit. Right panel: allowed region in the $M_{\rm th}$-$M_{\rm max}$ plane. Causality, the existence of a $2M_\odot$ neutron star, the upper limit on the tidal deformability of neutron stars from GW170817, and the lower limit on $M_{\rm th}$ from GW170817 (which corresponds to the lowest value in the 90% confidence interval for the total mass of the binary) determine the excluded regions. The different lines show curves with constant $R_{\rm max}$. The two values that are still marginally consistent with the current observations are shown as dashed black lines. Adapted from Kashyap *et al.*, 2022. Courtesy of R. Kashyap.

component. Such mergers are accompanied by significant mass ejection and are expected to be electromagnetically bright, despite the rapid black hole formation. In this regime $M_{\rm th}(q)$ is always smaller than $M_{\rm th}$ and decreases rapidly with q than for comparable mass-ratio systems. However, $M_{\rm th}(q)$ is still confined to be within 10% of the $q = 1$ value.

Perego *et al.* (2022) further reported that $\mathrm{d}M_{\rm th}/\mathrm{d}q$ is strongly correlated with the incompressibility parameter

$$K_{\rm max} = 9\frac{\partial p}{\partial n}\bigg|_{n=n_{\rm max}}, \tag{64}$$

where $n_{\rm max}$ is the central density in the maximum-mass neutron star and the derivative is computed for β-equilibrated matter. In particular, as $K_{\rm max}$ increases, $\mathrm{d}M_{\rm th}/\mathrm{d}q$ decreases. At a fixed q, higher $K_{\rm max}$ then results in an increase of the threshold mass for prompt collapse, which is reasonable since $K_{\rm max}$ measures the pressure response of the primary star to accretion of material from the secondary. This correlation implies that a measurement of $M_{\rm th}(q)$ for two or more q's would directly constrain $K_{\rm max}$.

2. Delayed collapse: Multimessenger constraints

The dynamics of binary neutron-star systems close to merger has a profound impact on the properties of their electromagnetic counterparts. However, while there is a sharp change in the dynamics with prompt collapse, the mass of the ejecta, as well as the mass of the bound accretion disk left after the merger, changes smoothly with the parameters of the binaries. As a result, the kilonova signal can be used to disfavor ranges of parameters in a continuous fashion, yielding more stringent constraints on the EOS.

For example, Fig. 20 shows the accretion disk mass measured for comparable mass-ratio $q \gtrsim 0.85$ binary neutron-star merger simulations as a function of the tidal parameter $\tilde{\Lambda}$ reported by Radice, Perego, Hotokezaka *et al.* (2018). Binaries with smaller $\tilde{\Lambda}$ are more compact and result in rapid formation of black holes with small ejecta mass and small accretion disks. As a result, their associated kilonova

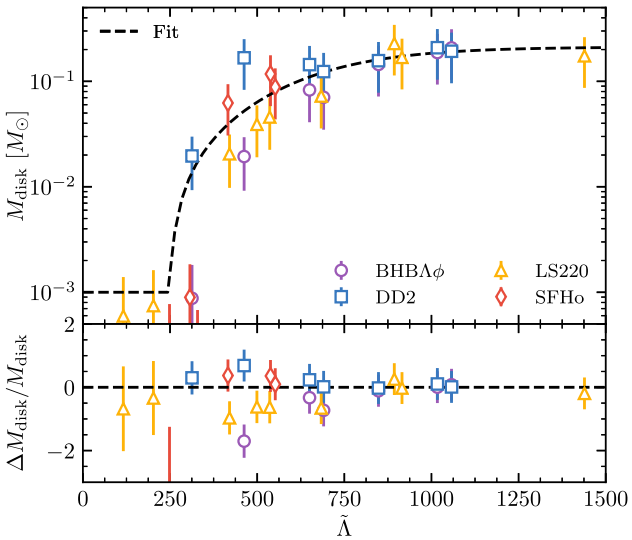

FIG. 20. Bound debris formed in comparable mass-ratio binary mergers as a function of the tidal parameter $\tilde{\Lambda}$. Top panel: the disk mass $M_{\rm disk}$ for binary simulations computed with different EOSs and having different masses and mass ratios. The dashed line is a fit to the data. Lower panel: the fit residual. From Radice, Perego, Hotokezaka *et al.*, 2018.

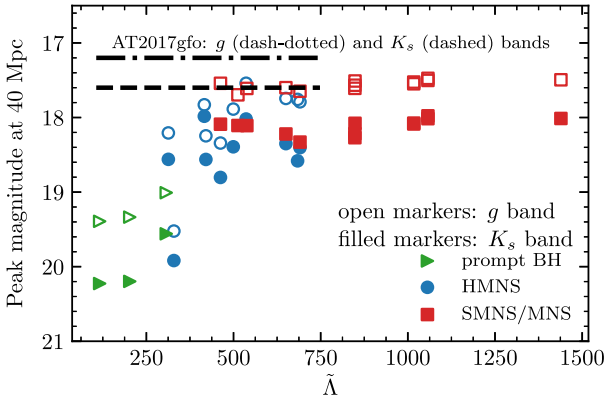

FIG. 21. Predicted peak kilonova luminosity measured in absolute magnitudes and in different photometric bands (K_s infrared, g optical) as a function of $\tilde{\Lambda}$ for a set of binary neutron-star merger simulations. The horizontal black lines show the magnitude of the kilonova associated with GW170817. Only models with relatively large $\tilde{\Lambda}$ that do not undergo prompt collapse are consistent with the data. Note, however, that this study considered only comparable mass-ratio binaries $q \gtrsim 0.8$; see the main text for a discussion of extensions of this work to smaller mass ratios. From Radice, Bernuzzi, and Perego, 2020.

signal is expected to be up to 2 orders of magnitude fainter and to evolve more rapidly, as shown in Fig. 21. This picture changes qualitatively for $q \lesssim 0.75$, when the tidal disruption of the secondary neutron star can lead to the formation of massive disks, even in conjunction with prompt black hole formation. Overall, scenarios with small tidal parameters and comparable mass ratios are disfavored by the presence of a kilonova in GW170817. This fact has been used to place more stringent constraints on the EOS with multimessenger data, as discussed later in the review.

Radice, Perego, Zappa, and Bernuzzi (2018) showed that the sum of disk and ejecta masses drops sharply for binaries with $\tilde{\Lambda} \lesssim 400$ and proposed a constraint on the tidal deformability of GW170817 from below. Kiuchi *et al.* (2019) warned against using the value of $\tilde{\Lambda} = 400$ as a strict lower limit and showed examples of binaries with $\tilde{\Lambda} < 400$ and significant mass ejection. Indeed, multimessenger analyses incorporating numerical relativity data and their systematic uncertainties find that the lower limit on $\tilde{\Lambda}$ is actually about 200 at the 90% confidence level (Radice and Dai, 2019), corresponding to a radius constraint of $R_{1.4} \gtrsim 11$ km. The disk mass data presented by Radice, Perego, Hotokezaka *et al.* (2018) and Radice, Perego, Zappa, and Bernuzzi (2018) were later refitted by Coughlin *et al.* (2019) in terms of the threshold mass to prompt collapse and used in several works (Capano *et al.*, 2020; Dietrich *et al.*, 2020; Huth *et al.*, 2022; Pang *et al.*, 2023). Fits using a larger set of simulation results, extending to much smaller mass ratios, and using simulations targeted to GW170817 were presented by Nedora *et al.* (2021, 2022) and used by Breschi *et al.* (2019) for a more careful reanalysis of GW170817 and the associated kilonova AT2017gfo. Overall, results from different groups are in broad agreement and suggest that $11\ \text{km} \lesssim R_{1.4} \lesssim 13\ \text{km}$ (Breschi *et al.*, 2019). Combined constraints from GW170817 and NICER (Raaijmakers *et al.*, 2020) and heavy-ion collisions (Tsang *et al.*, 2024), as well as studies combining GW170817, AT2017gfo, and NICER (Raaijmakers *et al.*, 2021; Pang *et al.*, 2023; Breschi *et al.*, 2024), favor slightly larger $R_{1.4}$ and provide better constraints for the EOS at densities beyond those probed in a $1.4M_\odot$ neutron star.

3. Long-lived merger remnants

Neutron-star binary systems with sufficiently low total mass can result in the formation of *long-lived remnants*, which avoid black hole formation for a timescale that is long (possibly infinite for absolutely stable remnants) compared to the postmerger gravitational-wave emission timescale of ∼10–20 ms. These remnants might collapse as a result of angular momentum loss to a magnetized wind and/or to residual gravitational-wave emission. The formation of a long-lived remnant is expected to be relatively common (Piro, Giacomazzo, and Perna, 2017; Radice, Perego, Bernuzzi, and Zhang, 2018) since there are low-mass neutron-star binary candidates in our Galaxy that would produce a long-lived remnant given the current lower limit on $M_{\max}$. Long-lived remnants have further been invoked to explain x-ray tails in short γ-ray bursts (Dai and Lu, 1998a, 1998b; Zhang and Meszaros, 2001; Dai *et al.*, 2006; Gao, 2006; Metzger, Quataert, and Thompson, 2008; Rowlinson *et al.*, 2013; Murase *et al.*, 2018; Dimple and Arun, 2023). The formation of a long-lived remnant is a possible explanation for a radio flare following GRB 201006A (Rowlinson *et al.*, 2024), although this interpretation is under debate (Sarin *et al.*, 2024). However, because long-lived remnants have a rotational energy of $\sim 10^{53}$ erg (Margalit and Metzger, 2017), if these remnants are formed and their energy is radiated in the form of wind, their formation should be accompanied by an extremely bright kilonova counterpart (Gao *et al.*, 2017; Sarin *et al.*, 2022; Wang, Beniamini, and Giannios, 2024) and the formation of a loud radio remnant (Nakar and Piran, 2011; Gao *et al.*, 2013). Neither signature has been observed (Schroeder *et al.*, 2020; Eddins *et al.*, 2023; Ghosh *et al.*, 2024).

The implications for the EOS are unclear and it is possible that even remnants believed to be long lived might collapse owing to effects that are currently not modeled in the simulations, such as the development of magnetic instabilities, a sudden softening of the EOS due to the appearance of new degrees of freedom, (Radice, Perego, Bernuzzi, and Zhang, 2018; Beniamini and Lu, 2021; Margalit *et al.*, 2022; Radice and Bernuzzi, 2023), or the fact that most of the rotational energy is lost to gravitational waves (Ai, Gao, and Zhang, 2020; Yuan, Fan, and Lü, 2023) and/or fails to thermalize the merger ejecta (Ai, Gao, and Zhang, 2024; Wang, Zhang, and Zhu, 2024). In the case of GW170817, the absence of a signature of a long-lived remnant has been broadly interpreted as placing an upper limit on the maximum mass of neutron stars of $2.17M_\odot$–$2.3M_\odot$, with more recent work generally favoring the more conservative upper limit in the light of the current uncertainties (Margalit and Metzger, 2017; Shibata *et al.*, 2017; Rezzolla, Most, and Weih, 2018; Ruiz, Shapiro, and Tsokaros, 2018; Shibata *et al.*, 2019; Khadkikar *et al.*, 2021; Margalit *et al.*, 2022). However, if long-lived remnants

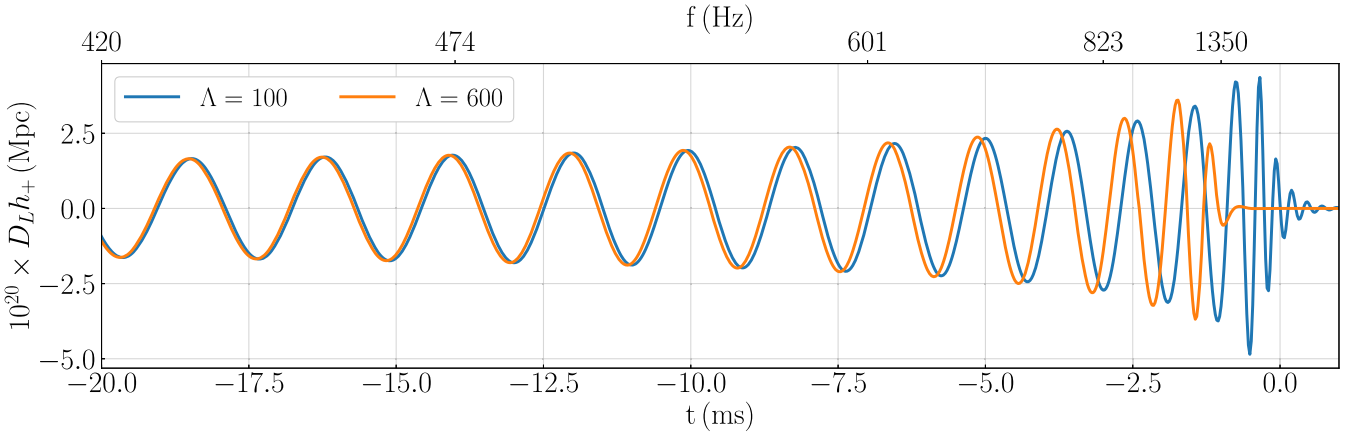

FIG. 22. Final inspiral and merger stages of a neutron-star–black hole binary for different values of the tidal deformability of the neutron star in the time domain. We plot the waveform using `IMRPhenomNSBH` (Thompson *et al.*, 2020) for a nonspinning $1.4M_\odot$ neutron star and a nonspinning $3M_\odot$ black hole. The upper x axis denotes the corresponding frequency for the $\Lambda = 100$ binary. Tidal deformation speeds up the binary evolution. The more deformable neutron star (orange curve) disrupts before merger, resulting in a rapid signal attenuation. The less deformable neutron star (blue curve) plunges into the black hole, leading to a ringdownlike signal.

are assumed to be required to produce γ-ray bursts with late-time activity, then about $1/4$ of the mergers need to form long-lived remnants. Given our current knowledge of the mass distribution of neutron-star binary mergers, this would translate in a lower limit on the maximum mass of neutron stars of $\sim 2.1 M_\odot$ (Fan, Wu, and Wei, 2013; Lasky *et al.*, 2014; Ai, Gao, and Zhang, 2020). Overall, a better theoretical understanding of the fate of such remnants and of the associated electromagnetic emission is needed to make such constraints robust.

F. Neutron-star–black hole binaries

Two qualitatively different merger scenarios are possible for mixed neutron-star–black hole binaries depending on the system properties; they are depicted in Fig. 22. In the first scenario (the orange curve in Fig. 22), the neutron star is severely deformed by the tidal field of the black hole to the point of complete disruption (Lackey *et al.*, 2014). The gravitational-wave signal then effectively turns off rapidly, as the system no longer comprises two compact objects and the overall orbital quadrupole moment (and its derivatives) are small. Disruption therefore strongly affects the gravitational-wave amplitude (Pannarale *et al.*, 2013,2015a; Lackey *et al.*, 2014; Matas *et al.*, 2020; Thompson *et al.*, 2020). In the second scenario (the blue curve in Fig. 22), the neutron star is more mildly deformed and plunges through the black hole horizon. The resulting merger gravitational-wave signal is then similar to that of a binary black hole, as the remnant black hole rings down to a steady state (Foucart *et al.*, 2013).

Which scenario is realized depends on the system properties (Foucart *et al.*, 2013,2019; Lackey *et al.*, 2014; Foucart, Hinderer, and Nissanke, 2018). Neutron-star disruption becomes more likely for systems with a low black hole mass (as the curvature and hence the tidal field strength is inversely proportional to the mass), large black hole spin aligned with the orbital angular momentum (as the black hole horizon is smaller for larger spins and thus the neutron-star can continue orbiting closer to the black hole before merger), and a neutron star that is less compact (as it is then more deformable). From the inspiral signal alone, the black hole mass and spin are correlated; see Sec. VI.B and the GW230529 discussion. Hence, detection of a disrupting signal would place strong constraints on these system properties that might otherwise be impossible. Indeed, since premerger tidal deformation (Kumar, Pürrer, and Pfeiffer, 2017) is generally expected to be small for neutron-star–black hole binaries as $\tilde{\Lambda} \sim q^4$, the merger conditions and the frequency at which the neutron star might disrupt (Pannarale *et al.*, 2015b) are complementary probes of the system properties and the EOS.

None of the currently detected neutron-star–black hole signals are informative for either scenario (Abbott *et al.*, 2021b; Abac *et al.*, 2024), owing to the high disruption frequency. Disruption is also generally expected to be more rare (Foucart, Hinderer, and Nissanke, 2018), especially since observationally most black holes in binaries have low spins and masses above $\sim 5 M_\odot$ (Abbott *et al.*, 2023b) and GW170817 places an upper limit on the neutron-star compactness (Abbott *et al.*, 2019a). The best candidate for disruption and an electromagnetic counterpart is GW230529 (Abac *et al.*, 2024) because of its low primary mass. However, even in this case there is no direct observational evidence in the gravitational-wave signal.

VII. ELECTROMAGNETIC OBSERVATIONS

We now present a review of recent pulsar mass measurements obtained with radio observations. Our primary focus is on measurements of extremely massive neutron stars obtained via the relativistic Shapiro delay (Demorest *et al.*, 2010; Fonseca *et al.*, 2021). Shapiro delay observations of a larger number of somewhat less massive neutron stars through pulsar timing arrays and other efforts are also discussed. We detail the relatively limited number of systematic uncertainties associated with this technique and discuss perceived trends in mass measurements (increasing or decreasing) as their uncertainties improve over time. We touch on recent extremely-high-mass results obtained from multiwavelength

studies of "spider" pulsars, some of which have been assisted by radio timing campaigns. Last, we discuss how upcoming and planned radio facilities will improve our efforts to more precisely measure additional neutron-star masses.

In this section we also describe constraints on the EOS from the predominantly thermal emission of isolated neutron stars, soft-x-ray transients, and quiescent low-mass x-ray binaries. Relativistic effects imprint information about neutron-star masses and radii in the emissions that we measure. By modeling these effects, we can recover information on neutron-star structure. We review constraints arising from spectral modeling of neutron stars exhibiting crust cooling or photospheric radius expansion bursts and those being delivered by pulse-profile modeling, a technique being pioneered by NICER. This section describes recent observations, their connections to the EOS, and the extent to which systematic uncertainties may impact those connections.

A. Radiation processes

Neutron stars emit across the electromagnetic spectrum, from low radio frequencies (van der Wateren *et al.*, 2023) to very-high-energy γ rays (Aharonian *et al.*, 2023). But there are two classes of electromagnetic emission that are particularly important for measurements that let us constrain the EOS.

Various forms of nonthermal emission may result in neutron stars manifesting as radio and/or γ-ray pulsars (Philippov and Kramer, 2022), enabling precision measurements of neutron-star spin. Long-term monitoring of spin and orbital evolution in relativistic binaries permits the measurement of neutron-star masses (discussed in more detail in Sec. VII.B).

The other involves thermal emission from the surface, typically due to the temperatures involved, in the x-ray. There are various physical processes that can heat the neutron-star surface to x-ray emitting temperatures: some internal (latent heat from birth or internal magnetic field decay, thermonuclear bursting due to unstable nuclear burning in accreted oceans, etc.) and some external (accretion, magnetospheric return current heating, etc.). Heating may be uniform or nonuniform: when it is nonuniform and x-ray emitting hot spots are misaligned with the rotational axis, the resulting emission will be pulsed at the spin rate of the neutron star.

As photons emitted from the surface layers propagate through the neutron-star spacetime toward the observer, relativistic effects encode information about the mass and radius[8] in the spectral and timing properties of the radiation. A rotating neutron star is not perfectly spherical, and its spacetime is not described by the Schwarzschild solution.

While ray tracing in a numerically computed spacetime (Stergioulas and Friedman, 1995; Vincent *et al.*, 2018) is possible, there are approximations that are computationally faster and sufficiently accurate for most current problems. For slowly rotating stars, the key effects to be modeled are gravitational redshift and light deflection, which leads to more of the stellar surface being visible (Thorne, 1977; Nättilä *et al.*, 2017). As rotation increases, one must also consider Doppler boosting, aberration, time delays, the effects of rotationally induced stellar oblateness, and perhaps the mass quadrupole moment, with the ray tracing being more complex if surface emission is not uniform. There is a large body of work developing computationally efficient spacetime approximations that take these effects into account (Pechenick, Ftaclas, and Cohen, 1983; Strohmayer, 1992; Miller and Lamb, 1998; Braje, Romani, and Rauch, 2000; Beloborodov, 2002; Poutanen and Gierliński, 2003; Cadeau *et al.*, 2007; Morsink *et al.*, 2007; Bauböck *et al.*, 2012; AlGendy and Morsink, 2014; Psaltis and Özel, 2014; Bauböck *et al.*, 2015; Nättilä and Pihajoki, 2018; Bogdanov *et al.*, 2019b; Oliva and Frutos-Alfaro, 2021; Silva *et al.*, 2021). The use of relativistic ray-tracing models to extract mass and radius from x-ray data is discussed in more detail in Secs. VII.C and VII.D.

B. Radio observations: Masses

Pulsars are a rapidly rotating, highly magnetized subset of the neutron-star population. Much like the rotation of a lighthouse, a pulsar's radiation beams appear to pulsate given a favorable orientation with Earth's line of sight. Roughly $1/10$ of these objects are millisecond pulsars that have been spun up to exceptional (roughly millisecond) rotational rates through the accretion of matter from a companion star (Bhattacharya and van den Heuvel, 1991). Owing to their fast rotation and slow spin-down rates, millisecond pulsars are ideal targets for pulsar timing, a process by which a pulsar's clocklike nature is exploited to create a model that will predict a pulse time of arrival accounting for each and every rotation —without losing count between observing sessions—over long time spans (Backer, Kulkarni, and Taylor, 1983). High-precision (roughly microsecond) pulsar timing facilitates a comparison between expected and measured times of arrival, indicating whether the pulses have been influenced by an unaccounted-for phenomenon. Millisecond pulsar timing has been used to great effect in efforts to test general relativity (Hulse and Taylor, 1975; Archibald *et al.*, 2018), detect low-frequency (nanohertz) gravitational waves (Agazie *et al.*, 2023b; Antoniadis *et al.*, 2023b; Reardon *et al.*, 2023; Xu *et al.*, 2023; Miles *et al.*, 2025), and constrain the neutron-star EOS; see Sec. VII.D.

The power of pulsar timing in directly constraining the neutron-star interior EOS is straightforward. Because each EOS dictates a maximum neutron-star mass, a well-constrained mass measurement for a sufficiently massive pulsar will rule out EOSs that predict a lower maximum mass. The main difficulty with this approach is that relatively few pulsar binaries allow for sufficiently high-precision mass measurements, as they generally require well-measured post-Keplerian timing parameters in suitably edge-on or frequently observed systems. However, in this subset of systems, radio pulsar timing offers a relatively model-independent (assuming the validity of general-relativity) and direct method for obtaining neutron-star masses.

For binary systems an adequate pulsar timing model requires five Keplerian orbital parameters: the projected semimajor axis $x \equiv a \sin(i)/c$ (where a is the semimajor

[8]The radius measured is the photosphere. How this relates to the radius as defined in the TOV equations and any subsequent EOS analysis will need to be considered.

axis and i is the orbital inclination), the longitude of periastron ω, the time of periastron passage T_0, the orbital period P_b, and the orbital eccentricity e. As these parameters are measured to notably high precision, all but the pulsar and companion masses (m_p and m_c, respectively) nearly complete the Keplerian mass function,

$$f(m_p, m_c) = \frac{4\pi^2}{G}\frac{(a \sin i)^3}{P_b^2} = \frac{(m_c \sin i)^3}{(m_p + m_c)^2}, \quad (65)$$

leaving only the component masses unknown. In a relatively small number of observed millisecond pulsar binaries, one is able to measure post-Keplerian general-relativistic parameters: the rate of periastron advance $\dot{\omega}$ (orbital precession), Einstein delay γ (which includes time dilation and gravitational redshift), orbital period decay $\dot{P}_b$, and the Shapiro delay "range" and "shape" parameters r and s (which describe the magnitude and extent of the pulse time of arrival delay due to the pulsar's position at superior conjunction). Assuming general relativity,

$$r = T_\odot m_c, \quad s = \sin(i) = x\left(\frac{P_b}{2\pi}\right)^{-2/3} T_\odot^{-1/3} M_T^{2/3} m_c^{-1}, \quad (66)$$

where M_T is the total mass and $T_\odot = GM_\odot/c^3 \approx 4.9$ μs. The post-Keplerian parameters provide additional measurements that depend on the orbital parameters and masses, so the observation of two post-Keplerian effects will break the degeneracy and isolate m_p and m_c; see Taylor *et al.* (1992), Stairs (2003), and Freire and Wex (2010) for more details. Any possibility of constraining post-Keplerian parameters depends on the system in question. For example, high-e orbits are favorable for $\dot{\omega}$ and γ, long timing baselines are required for $\dot{P}_b$, and nearly edge-on orbits with $\sin(i) \approx 1$ are required for Shapiro r and s; see Fig. 23.

Measuring the relativistic Shapiro delay in highly inclined millisecond pulsar binaries, which appears as a delay in pulse times of arrival as the pulsar passes behind its companion during superior conjunction, has been one of the most fruitful ways to constrain pulsar masses and, in turn, the EOS. Demorest *et al.* (2010) presented the first evidence for a $\sim 2M_\odot$ neutron star via pulsar timing measurements of PSR J1614–2230, measuring its mass to be $1.97 \pm 0.04M_\odot$ and challenging a number of softer EOSs. Further timing of this millisecond pulsar led to an improved constraint of $1.928 \pm 0.017M_\odot$ (Fonseca *et al.*, 2016). More recently but in a similar fashion, Cromartie *et al.* (2020) measured the mass of the millisecond pulsar PSR J0740+6620 to be $2.14^{+0.10}_{-0.09}M_\odot$ (68.3% credibility interval). Adding data from the Canadian Hydrogen Intensity Mapping Experiment (CHIME) to the updated Green Bank Telescope dataset, Fonseca *et al.* (2021) further constrained the mass to be $2.08 \pm 0.07M_\odot$. This radio-derived constraint on the mass of PSR J0740+6620 facilitated improved constraints on its radius; see Sec. VII.C.

Caution should be exercised in cases where the Shapiro delay cannot be precisely constrained, as is frequently the case in non-edge-on ($i \lessapprox 85°$) orbits where the induced timing delay is comparable to the achievable timing precision. If r and s cannot be measured to high precision, unmodeled delays induced by astrometry, intrinsic red noise, or chromatic red noise from interstellar medium dispersion can negatively impact the accuracy and precision of pulsar mass constraints. This is not a concern for most near-edge-on systems, especially if the pulsar has been timed for a duration that is sufficiently long to constrain slowly varying parameters. For example, Fonseca *et al.* (2021) showed that varying the dispersion measure modeling scheme changed the measured pulsar mass by only ∼1%. However, in cases such as the γ-ray bright millisecond pulsar PSR J1231–1411, with a measured inclination angle closer to 80°, choices in modeling the interstellar medium and solar wind dispersion measure, astrometry, and intrinsic red noise can have a more deleterious impact; see Salmi *et al.* (2024a) and references therein.

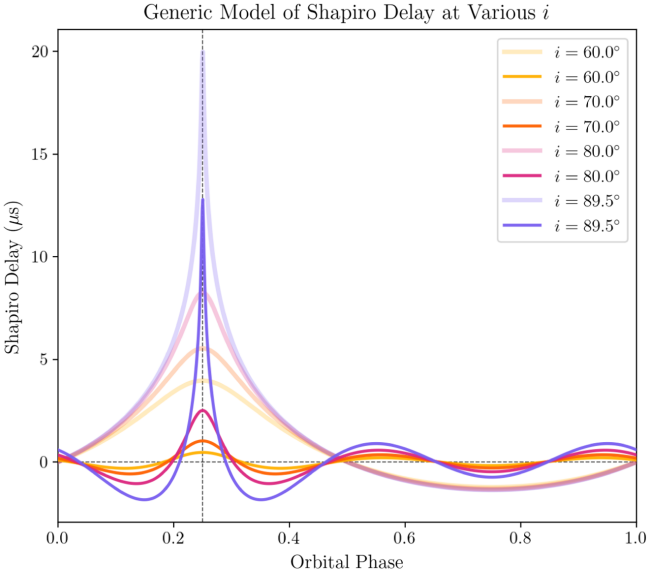

FIG. 23. Pulse arrival delay induced by the Shapiro time delay. Translucent curves represent the absolute Shapiro delay, while opaque curves indicate the measurable Shapiro delay (the amount of detectable Shapiro delay when one simultaneously fits for all orbital parameters).

Observations of systems where other post-Keplerian parameters can be measured have also yielded profound results. For example, Barr *et al.* (2024) significantly measured $\dot{\omega}$ in an eccentric millisecond pulsar located in a globular cluster (PSR J0514–4002E) using the MeerKAT telescope, implying that the total system mass is $3.8870 \pm 0.0045M_\odot$. Combining upper limits on r, s, and γ (none of which were significantly detected) with the mass function yields a pulsar mass $< 1.79M_\odot$ and a companion mass $> 2.09M_\odot$ (95% credible interval). Because the companion was not detected in optical or near-ultraviolet Hubble Space Telescope observations, it may be a black hole or massive neutron star existing in the mass gap between the maximum pulsar mass and minimum black hole mass.

Several massive millisecond pulsars have been measured using techniques that target m_c through optical spectroscopy and photometry, which are used to break the mass function degeneracy in cases where post-Keplerian parameters cannot

be measured. Antoniadis *et al.* (2013) reported the next $\sim 2M_\odot$ neutron star after that of Demorest *et al.* (2010), PSR J0348+0432. Radio pulsar timing measurements from the Robert C. Byrd Green Bank Telescope (GBT) provided a sufficiently precise position to optically identify the pulsar's companion in the Sloan Digital Sky Survey. Spectroscopy with the Apache Point Optical Telescope yielded deep, resolved hydrogen lines and confirmed the pulsar's association with its white dwarf companion. The mass ratio of the two objects was derived by combining measurements of the companion's velocity obtained with the Very Large Telescope's FORS2 spectrograph with pulsar velocity measurements from GBT radio timing. As no significant brightness variability or rotation-induced line broadening was detected, the effective temperature and surface gravity of the white dwarf companion were derived from Balmer line modeling using a high-signal-to-noise average spectrum. Using a conservative (thick envelope) finite-temperature mass-radius relationship for white dwarfs, the mass of PSR J0348+0432 was reported to be $2.01 \pm 0.04 M_\odot$. In this way the measurement of Antoniadis *et al.* (2013) is dependent on models of white dwarf cooling; however, the straightforward binary system and ample observations helped bolster the model selection.

PSR J0952-0607 was discovered in a search of Fermi-LAT unassociated sources using Low Frequency Array (LOFAR) (Bassa *et al.*, 2017) and boasts the fastest spin rate of any Galactic millisecond pulsar. However, this millisecond pulsar's companion is faint, pushing the limits of visibility even with 10-m-class telescopes. Romani *et al.* (2022) measured the mass of this highly accelerated "black widow" millisecond pulsar using the Keck I 10 m telescope and Low Resolution Imaging Spectrometer over two imaging and six spectroscopic observations. This binary presented several challenges owing to its faintness, and large brightness drops. Although this system does not suffer from effects that complicate models of other spider pulsars such as significant pulsar heating or high Roche lobe filling—neither of which is favored by their fits—several choices are required during the analysis that render the measurement model dependent. Among these are the choice of the light curve fitting model, determining weights for linewidths as a function of surface temperature, and the necessary inclusion of more poorly determined parameters, for example, extinction and photometric calibrations. The mass of PSR J0952-0607 is reported to be notably high, at $2.35 \pm 0.17 M_\odot$ (68% credible interval). The faint nature of the white dwarf companion implies that this measurement will improve as larger-class optical telescopes come online.

Pulsar timing array experiments aim to detect nanohertz gravitational waves of astrophysical or cosmological origin by searching for quadrupolar correlations in pulse time of arrival deviations. Seven pulsar timing array collaborations are currently active: the African Pulsar Timing collaboration, the Chinese Pulsar Timing Array (CPTA), the European Pulsar Timing Array (EPTA), the Indian Pulsar Timing Array, the MeerKAT Pulsar Timing Array, the North American Nanohertz Observatory for Gravitational Waves (NANOGrav), and the Parkes Pulsar Timing Array (PPTA). Recently, pulsar timing arrays have produced evidence for a stochastic background of nanohertz gravitational waves, likely produced by merging supermassive binary black holes (Agazie *et al.*, 2023b; Antoniadis *et al.*, 2023b; Reardon *et al.*, 2023; Xu *et al.*, 2023; Miles *et al.*, 2025).

Because sensitivity to gravitational waves increases as more pulsars are timed to better precision over longer periods of time, the resulting datasets are expansive and ripe for synergistic science pursuits. Both the second EPTA and third PPTA data releases, along with the NANOGrav 15-year dataset, contained newly constrained pulsar masses from measurements of post-Keplerian parameters (Agazie *et al.*, 2023a; Antoniadis *et al.*, 2023a; Zic *et al.*, 2023). The high-mass millisecond pulsars PSR J1614–2230 and PSR J0740+6620 are both included in the NANOGrav dataset. The pulsar timing array's high-cadence timing data, when combined with targeted observations over superior conjunction, made it possible to constrain these pulsar masses. Without a hint of Shapiro delay emerging in NANOGrav data, it is possible that these sources would have never been timed over sufficiently long periods to meaningfully constrain their masses. Of the 68 millisecond pulsars included in the NANOGrav 15-year data release (Agazie *et al.*, 2023a), 50 are in binaries. Seventeen of these systems show significant constraints on companion mass and inclination via the relativistic Shapiro delay.

Although the sample of well-constrained Shapiro-delay-derived masses is small, no evidence suggests that these measurements tend to either overestimate or underestimate masses. For example, the median mass for seven of the millisecond pulsars in the NANOGrav 15-year data release decreased, while seven either did not significantly change or increased. Selection bias may be at fault for any perceived overestimation of masses with this technique, as one will reasonably focus more on minute measurement improvements in the highest-mass neutron stars. The reported credible intervals for masses of millisecond pulsars such as PSRs J1614–2230 and J0740+6620 have stayed self-consistent with the addition of data. In the case of PSR J0740+6620, the 3σ lower limit on the measured mass is unchanged between Cromartie *et al.* (2020) and Fonseca *et al.* (2021). Because the mass distribution of neutron stars (not just the maximum mass) impacts theories of binary evolution and neutron-star formation, the value of constraining any neutron-star mass significantly, even if $m_p \ll 2M_\odot$, should not be overlooked.

C. X-ray spectroscopy

One method of determining mass and radius is to fit the x-ray spectrum emitted by the compact object to a model of the neutron-star atmosphere that describes the x-ray emission from the surface; see the pioneering work of Zavlin, Pavlov, and Shibanov (1996), Rutledge *et al.* (1999), Heinke *et al.* (2006), and Webb and Barret (2007). Atmosphere models must choose the composition of the atmosphere (typically H, He, or C) (Rajagopal and Romani, 1996; Ho and Heinke, 2009), the distribution of temperatures across the surface (often, one temperature is assumed), and the magnitude of the magnetic field; see the early work of Burwitz *et al.* (2001) and Ho *et al.* (2007). Atmosphere models also take into account

the relativistic effects that arise from spherically symmetric metrics. More sophisticated models may include more detailed effects, as described in Sec. VII.A. This technique has been applied most extensively to quiescent low-mass x-ray binaries, where the surface has been heated by accretion that has then stopped. The accretion process generates a significant x-ray luminosity that dominates over the surface emission, but when the accretion subsides, the surface is visible. In cases where the magnetic field can be estimated, low-mass x-ray binary (LMXB) magnetic fields are observed to be on the order of $10^{8–9}$ G. These smaller magnetic fields may be the result of a process whereby the accretion buries the magnetic field (Konar and Bhattacharya, 1997). Fitting the atmosphere model to the emergent x-ray spectrum leads to a determination of the neutron-star mass and radius and then to a constraint on the equation of state of dense matter.

To see how this works, for the moment we assume the simple case of a nonaccreting neutron star with no magnetic field that emits as a black body. In this case, if one has a measurement of the distance D to the neutron star, a measurement of the flux F, and a measurement of the effective temperature (as observed at infinity) T_∞, then a constraint on the mass and radius can be obtained from

$$F = \left(\frac{R}{D}\right)^2 \sigma T_\infty^4 (1-2\beta)^{-1}. \tag{67}$$

Equation (67) includes a correction from general relativity defining $\beta \equiv GM/(Rc^2)$. The local temperature of the fluid is $T = T_\infty(1-2\beta)^{-1/2}$. Thus, a measurement of the flux and the temperature gives a constraint on $R_\infty \equiv R(1-2\beta)^{-1/2}$. Atmosphere models also provide a separate weak constraint on the mass.

Mass and radius constraints have also been obtained from thermonuclear bursters using the emission during an x-ray burst that is triggered by unstable thermonuclear burning in the accreted ocean. Bursts that are particularly energetic may lift the photosphere off of the neutron-star surface (Ebisuzaki, Hanawa, and Sugimoto, 1983; Paczynski, 1983); they are named photospheric radius expansion bursts. These bursts create a unique opportunity to measure the neutron-star radius, as pioneered by Özel (2006).

Spectral modeling of these sources is complicated by a number of factors. Ideally, the distance must be known: while distances for quiescent LMXB in globular clusters may be known to better than 10%, this is not always the case for the bursters. A mass and radius determination depends on a model of the time evolution of the burst and the connection between the photosphere and the neutron-star radius. In addition to the previously described effects, the accretion process may create an additional uncertainty in modeling LMXBs. Pileup, when multiple photons hit the CCD at nearly equal times, is an issue for the brightest LMXBs because the event is recorded as a single photon with a higher energy. Rotational corrections may be significant even if the rotation rate cannot be measured, and surface emission may be nonuniform even if it is not detectable (for example, if a hot spot were centered on the rotational pole). This has led to a great deal of debate in the literature about these methods (Guillot *et al.*, 2013; Bauböck *et al.*, 2015; Elshamouty *et al.*, 2016; Nättilä *et al.*, 2017; Suleimanov, Poutanen, and Werner, 2020; Miller, 2021) and the latest modeling attempts to address these issues.

Mass and radius constraints from quiescent low-mass x-ray binaries and photospheric radius expansion x-ray bursts were used to predict the neutron-star tidal deformability (Steiner *et al.*, 2015), which was measured in GW170817 two years later (Abbott *et al.*, 2017b). Recent modeling of x-ray bursts fits bursting atmosphere models directly to spectra during the cooling tails of bursts, thereby avoiding some of the earlier issues (Nättilä *et al.*, 2017), and rotational corrections are now also being included (Suleimanov, Poutanen, and Werner, 2020). The latest modeling of quiescent LMXB takes into account uncertainties in the distance, atmosphere composition, and the possible presence of undetected asymmetries in the emission (Steiner *et al.*, 2018). The more recent analyses also directly couple in information from current EOS models (Baillot d'Etivaux *et al.*, 2019). Al-Mamun *et al.* (2021) attempted to detect systematic uncertainties in quiescent LMXB and x-ray burst constraints on neutron-star masses and radii via a Bayesian inference with observations from GW170817 and found that no additional systematic uncertainties were required to explain the data.

Other types of neutron stars that have led to equation-of-state constraints are isolated neutron stars (Pons *et al.*, 2002), x-ray bursting sources that do not show photospheric radius expansion (Meisel, 2018), soft x-ray transients [pioneered by Heinke *et al.* (2009)], and "crust cooling" sources (Brown and Cumming, 2009; Ootes *et al.*, 2016).

D. X-ray pulse-profile modeling

Pulse profile modeling [see Watts *et al.* (2016), Bogdanov *et al.* (2019b), and references therein], like the techniques described in Sec. VII.C, exploits the fact that general and special relativity leave mass- and radius-dependent imprints on thermal x-rays emitted from the neutron-star surface. However, it involves rotational-phase-resolved spectral modeling applied to stars whose x-ray emission varies as the star rotates because of nonuniformities—often called hot spots—in the surface temperature distribution. The emission from these sources is as a consequence pulsed at the spin frequency of the neutron star.

The properties of the pulsations—the flux and spectrum as a function of rotational phase—are determined in part by the various effects described in Sec. VII.A. Higher compactness (mass and radius), for example, suppresses amplitude, while Doppler boosting (which depends primarily on the line of sight velocity of the surface elements, and hence the radius) increases harmonic content (Lo *et al.*, 2013; Psaltis, Özel, and Chakrabarty, 2014). These complementary effects enable us, in principle, to disentangle mass and radius (Bogdanov *et al.*, 2021).

Since effects like Doppler boosting are stronger for more rapid spin, pulse profile modeling is most typically discussed in the context of rapidly spinning neutron stars: rotation-powered millisecond pulsars, accretion-powered millisecond

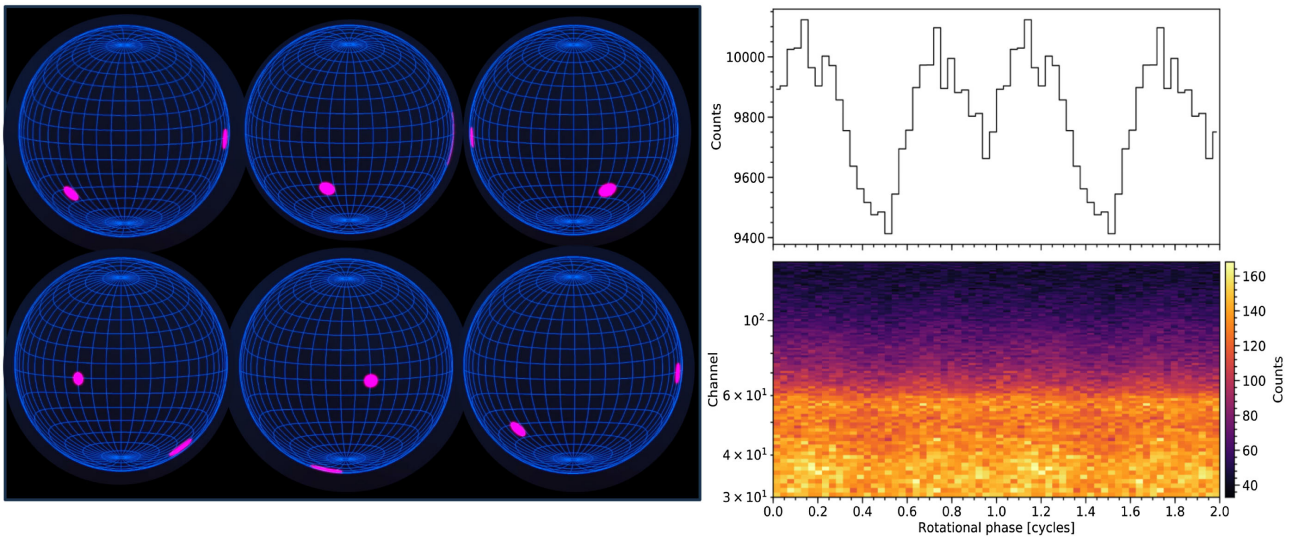

FIG. 24. The formation of a pulse profile. Left image: snapshots at various points of the star's spin cycle as a star with two hot spots rotates. The effects of gravitational lensing on spot visibility are clear. Courtesy of NASA and Sharon Morsink. Top right panel: the resulting bolometric pulse profile (summed over energy channels). Bottom right image: energy-resolved pulse profile as recorded by the NICER telescope. Counts denote the number of events (x-ray photons and background due to, for example, charged particles) recorded. From Riley *et al.*, 2021.

x-ray pulsars (Patruno and Watts, 2021), and thermonuclear burst oscillation sources (Watts, 2012).

As photons arrive at the x-ray telescope, two things must be recorded: the time of arrival and the energy channel. The former can be mapped to a rotational-phase bin using a spin ephemeris for the neutron star, while the latter depends on the incident photon energy and the instrumental response matrix. Over time a pulse profile is built up, as shown in Fig. 24. Good time and energy resolution[9] are essential for mapping out the pulse profile in as much detail as possible, with constraints also improving as the number of photons in the profile increases (Lo *et al.*, 2013; Psaltis, Özel, and Chakrabarty, 2014).

To determine the mass and the radius we need a physical model of how the pulse profile is formed. The main ingredient is the relativistic ray-tracing model itself: the ability to propagate photons from the emitting surface to the detector through a spacetime defined by the mass, radius, and spin. Here we build on decades of work that have formed a good understanding of the spacetime of rapidly rotating neutron stars (Sec. VII.A). Current modeling relies primarily on the oblate Schwarzschild spacetime model (Morsink *et al.*, 2007). This includes the most important previously described general and special relativistic effects plus modifications due to rotation-induced stellar oblateness, making use of an approximation for the oblate shape of the neutron star that is largely EOS independent (AlGendy and Morsink, 2014). Other factors that affect the pulse profile and that must be modeled include the atmospheric beaming function (the energy and emission angle dependence of the escaping radiation), the instrument response, the source distance, the observer inclination, the interstellar absorption, and the properties (size, shape, location, and temperature) of the hot spots. With these in place, one can simulate pulse profiles for comparison to data.

Early efforts to model pulse profiles, using datasets from the Rossi X-Ray Timing Explorer and XMM-Newton, involved χ-squared fitting for pulse profiles with a limited number of energy bands (Poutanen and Gierliński, 2003; Bhattacharyya *et al.*, 2005; Bogdanov, 2013). A step change has been enabled by NICER (Gendreau *et al.*, 2016), an instrument specifically designed to collect large high-quality pulse-profile datasets for millisecond pulsars. The millisecond pulsars observed by NICER are also radio pulsars that can be timed precisely. This provides the spin ephemeris that is used to form the pulse profile (assigning photons to phase bins[10]) but can also—if the pulsar is in a binary, sometimes provide priors on mass, distance, and orbital inclination; see Sec. VII.B. The posterior distributions for all of the model parameters, including the mass and radius, are now fully sampled (Bogdanov *et al.*, 2019b, 2021).

NICER was launched in 2017 and, since that time, has been building up pulse-profile datasets for seven x-ray bright millisecond pulsars [the faintest, PSR J0740+6620, was added to the target list after launch following the measurement of its mass by Cromartie *et al.* (2020) and the discovery of its x-ray

[9]The millisecond pulsars being studied with NICER data, for example, have spin frequencies in the range of ∼200–350 Hz. Studies to date have used pulse profiles with 32 phase bins per rotational cycle (Bogdanov *et al.*, 2019a), facilitated by the submicrosecond time resolution. The energy resolution for NICER is high enough that pulse profiles are constructed using over 100 energy channels. This time and energy resolution allows fine mapping of phase- and energy-dependent features such as hot spot edges.

[10]The millisecond pulsars are highly stable, and there are timing solutions available that either cover the full NICER date range or are so precise that they can be extrapolated safely, allowing phase connection over long periods of time.

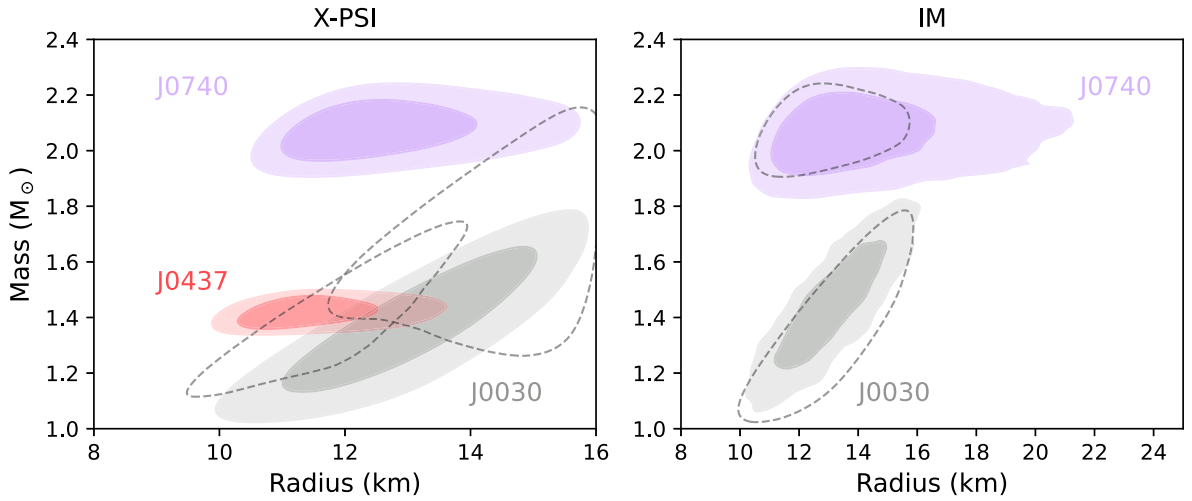

FIG. 25. Credible regions for mass and radius (68% and 95% regions, where shaded) reported from pulse profile modeling analyses of NICER data. Left panel: results derived using the x-ray pulse simulation and inference (X-PSI) pipeline (Riley *et al.*, 2023) for PSR J0740+6620 (Salmi *et al.*, 2024a), PSR J0437+4715 (Choudhury *et al.*, 2024), and PSR J0030+0451 (Vinciguerra *et al.*, 2024). The shaded regions for PSR J0030 + 0451 are for the preferred model when only the NICER data are analyzed. The dashed black lines show the 95% credible regions for two solutions (different models) identified in a joint analysis of NICER and XMM-Newton data for this source; see the text. A fourth source, PSR J1231-1411 (Salmi *et al.*, 2024b), has thus far proven more challenging to analyze and is not shown. Right panel: results derived using the Illinois-Maryland (IM) pipeline for PSR J0740+6620 (Dittmann *et al.*, 2024) and PSR J0030+0451 (Miller *et al.*, 2019). The dashed black lines show the corresponding 95% X-PSI contours for comparison. The upper bounds on the x axes reflect the different radius priors used by the various pipelines (bear this in mind when comparing the results).

pulsations by NICER (Wolff *et al.*, 2021)]. The inferred masses and radii to date for three of the pulsars reported are summarized in Fig. 25.

One of the more complex challenges with the NICER modeling is how to describe the properties of the hot spots. For the millisecond pulsars, the x-rays are thought to be thermal emission due to return current heating of the magnetic poles. The expected shape of the heated regions depends on the physics of the magnetosphere and the field geometry, and various shapes are possible (Harding and Muslimov, 2001; Lockhart *et al.*, 2019), including spots, rings, and arcs. To date, studies have used parametrized models that encompass a wide range of possibilities, constructed, for example, from overlapping circles or ovals. Along with the inferred mass and radius, there is also an inferred hot spot geometry that is sensitive to this modeling choice.

The first source for which results were reported, PSR J0030+0451, is a 205 Hz isolated millisecond pulsar at a distance of 329 pc. Since it is isolated, there is no mass measurement from radio timing; a prior range of $1–3M_\odot$ was assumed. Analyses of NICER data from July 2017 to December 2018 [∼1.9 Ms in total (Bogdanov *et al.*, 2019b)] by two independent pipelines yielded similar results. Riley *et al.* (2019), using the X-PSI code (Riley *et al.*, 2023), obtained a mass of $1.34^{+0.15}_{-0.16}M_\odot$ and a radius of $12.71^{+1.14}_{-1.19}$ km (68% credible intervals), while Miller *et al.* (2019) found a mass and radius of $1.44^{+0.15}_{-0.14}M_\odot$ and $13.02^{+1.24}_{-1.06}$ km, respectively. The inferred hot spot properties were similar despite different parametrizations: a small spot and a long extended emitting region in the same hemisphere, thus pointing to a complex magnetic field geometry (Bilous *et al.*, 2019; Chen, Yuan, and Vasilopoulos, 2020; Kalapotharakos *et al.*, 2021; Pétri *et al.*, 2023).

Subsequent simulations (Vinciguerra *et al.*, 2023) and a more detailed analysis of this dataset using the X-PSI pipeline (Vinciguerra *et al.*, 2024) paint a more complex picture. Analyzing only the NICER dataset with the same hot spot models gives results that are highly consistent with the earlier results of Riley *et al.* (2019). However, the likelihood surface is multimodal, which becomes important once background constraints are included via joint modeling with XMM-Newton data for this source; see the forthcoming discussion. Subject to some caveats, the analysis finds inferred masses and radii $\sim[1.4M_\odot, 11.5$ km] or $\sim[1.7M_\odot, 14.5$ km], depending on the assumed spot model (credible intervals are similar to the analysis without background constraints). The two hot spots no longer need to be in the same hemisphere and may have temperature gradients rather than being elongated. This source also appears to be sensitive to different choices regarding the atmosphere model (Salmi *et al.*, 2023), although evolutionary models and evidence favor the fully ionized hydrogen atmosphere model used to generate the previously cited results. Ongoing studies using larger datasets may resolve some of these ambiguities, but in the meantime EOS studies should consider the impact of the possible multimodality when using mass-radius posteriors from this source (Christian, Schaffner-Bielich, and Rosswog, 2024; Rutherford *et al.*, 2024).

The second source for which NICER pulse-profile modeling analysis has been done is the $2.1M_\odot$ millisecond pulsar PSR J0740+6620; for the mass measurements from radio timing, see Cromartie *et al.* (2020), Fonseca *et al.* (2021), and VII.B. This source was the first for which background

constraints were included in the analysis, via joint modeling with XMM-Newton data. In this context *background* means emission from anything other than the hot spots, astrophysical or instrumental, and is assumed to be unpulsed (a phase-invariant spectral component in pulse profile). Pulsed emission must come from the hot spots, but they can also contribute an unpulsed component: for example, if a spot overlaps the rotational pole or the star is highly compact such that the spots stay in view even when rotated to the far side of the star. Putting limits on the NICER background is challenging (Remillard *et al.* (2022)). For XMM-Newton datasets, it is easier to get a good estimate of background since XMM-Newton is an imaging telescope, whereas NICER is not. Modeling the high-quality spectral-timing NICER data simultaneously with even phase-averaged XMM-Newton data, with a background estimate for the latter, puts indirect constraints on the NICER background by helping to determine the total phase-averaged (pulsed and unpulsed) flux from the pulsar.

Using data from September 2018 to April 2020 (1.6 Ms in total) (Wolff *et al.*, 2021), Riley *et al.* (2021) reported a radius of $12.39^{+1.30}_{-0.98}$ km, while Miller *et al.* (2021) found a radius of $13.7^{+2.6}_{-1.5}$ km. The inferred mass is essentially unchanged from the radio prior, at $2.08 \pm 0.07 M_\odot$. The reasons behind the differences in the inferred radii from the two pipelines were discussed in depth by Miller *et al.* (2021) and Riley *et al.* (2021), but the main factors are differences in priors (mainly the choice of the upper limit for radius; see Fig. 25), assumptions about NICER/XMM-Newton cross-calibration uncertainty, treatment of the XMM-Newton background information, and sampler choice. However, both analyses disfavor lower radii. A subsequent analysis using NICER background models (Salmi *et al.*, 2022) delivered consistent results compared to the joint analysis with XMM-Newton. The hot spot properties for this source appear to be simpler than for PSR J0030+0451, although once again the two hot spots are not antipodal, pointing to a magnetic field that is not a simple centered dipole. The results for this source are less sensitive to variations in atmosphere model, perhaps because of the highly constrained geometry, mass, and distance (Salmi *et al.*, 2023). More recent analyses using NICER data through April 2022 produced consistent but slightly tighter results on the radius (Dittmann *et al.*, 2024; Salmi *et al.*, 2024a; Hoogkamer *et al.*, 2025). The fact that the credible intervals for PSR J0740+6620 are similar to those of PSR J0030+0451, despite the good mass prior on the former, reflects the difference in dataset quality: PSR J0740+6620 is farther away, at ∼1.2 kpc, and hence has a lower signal-to-noise ratio.

The third source for which analysis has been done is the closest and brightest x-ray millisecond pulsar PSR J0437-4715, which is at a distance of only 157 pc (Reardon *et al.*, 2024). This source is in a binary with a favorable inclination for measurement of the Shapiro delay, enabling a tight mass measurement (used as a prior in the pulse profile modeling) of $1.418 \pm 0.044 M_\odot$. This source must be observed off axis owing to the presence of a bright active galactic nucleus (AGN) in NICER's field of view. Despite this, the AGN still contributes to the NICER background, and this must therefore be taken into account when modeling the source. Using NICER data from July 2017 to July 2021 and NICER background estimates, Choudhury *et al.* (2024) reported an inferred mass of $1.418 \pm 0.037 M_\odot$ and a radius of $11.36^{+0.95}_{-0.63}$ km. Once again, the hot spot geometry for the models studied was inconsistent with a simple centered dipole magnetic field.

VIII. FUTURE THEORETICAL AND EXPERIMENTAL AND OBSERVATIONAL CHALLENGES AND OPPORTUNITIES

In this final section, we give a summary of future challenges and directions about constraints on the nuclear EOS, matter at high densities, and future neutron-star observations. Observations of neutron stars will provide exciting, high-precision constraints on dense matter in the coming decades. To analyze these data, it is crucial that constraints from nuclear theory and experiments keep up with this. For theoretical calculations of the EOS, at low densities uncertainties can be improved by pushing nuclear interactions from chiral EFT to higher orders. In addition, it is important to study open issues in chiral EFT, such as the dependence of results on the regulator scale, the power-counting scheme, or new approaches to constructing chiral interactions (Tews *et al.*, 2020). Similarly, constraints at asymptotically high densities can be obtained from perturbative QCD (Kurkela *et al.*, 2014; Gorda, Komoltsev, and Kurkela, 2023; Somasundaram, Tews, and Margueron, 2023; Komoltsev *et al.*, 2024). Improvements in these calculations might enable them to provide valuable constraints on the EOS (Koehn *et al.*, 2024; Komoltsev *et al.*, 2024). Aside from these approaches, there are no systematic order-by-order approaches at intermediate densities. At these densities we are only able to compare different models of dense matter, some of which include phase transitions to forms of quark matter, to astrophysical data.

In addition to these modeling advances, it is key that all theoretical predictions provide meaningful uncertainties. Recently, several approaches have been explored (Epelbaum, Krebs, and Meißner, 2015a; Drischler *et al.*, 2020; Keller, Hebeler, and Schwenk, 2023), some of which used Gaussian processes to provide a statistical interpretation of the error bands. The shape of the assumed uncertainty band impacts the inference results for the dense matter EOS (Koehn *et al.*, 2024). Additional work is necessary to investigate and quantify the systematic error of these *ad hoc* choices. Ideally, one should propagate uncertainties directly from distributions of low-energy couplings to the desired observables instead of estimating uncertainties *a posteriori*.

Finally, future experimental constraints on the EOS will provide valuable opportunities. The recent measurement of the neutron-skin thickness by the PREX Collaboration (Adhikari *et al.*, 2021) and the CREX Collaboration (Adhikari *et al.*, 2022) have provided constraints on the symmetry energy and its slope, albeit with large uncertainties. A similar future experiment by the Mainz Radius Experiment Mammei *et al.*, 2024) might improve on the current situation and provide valuable constraints. Similarly, heavy-ion collision experiments provide an excellent way of constraining the EOS at intermediate densities (Huth *et al.*, 2022; Tsang *et al.*, 2024). Analyses of these experiments suffer from larger systematic uncertainties, but improved theoretical analysis tools, such as transport models, will enable HIC experiments to

bridge the gap between constraints from nuclear physics and astrophysics.

Beyond the current (fourth) observing run of the ground-based gravitational-wave detector network (Abbott *et al.*, 2018a), the next (fifth) observing run is expected around 2027 with $\mathcal{O}(1–10)$ anticipated detections of binaries containing neutron stars. The information yielded by these detections will depend sensitively on their properties, primarily on the system mass and the signal strength. Further proposed detectors include Voyager (Adhikari *et al.*, 2020), A# (Gupta *et al.*, 2023), NEMO (Ackley *et al.*, 2020), and the third-generation detectors Cosmic Explorer (Reitze *et al.*, 2019) and Einstein Telescope (Punturo *et al.*, 2010b), which will be sensitive to edge of the observable Universe.

The third-generation detectors are expected to observe tens of thousands of signals containing neutron stars (Sachdev, Regimbau, and Sathyaprakash, 2020; Borhanian and Sathyaprakash, 2024; Johnson, Chatziioannou, and Farr, 2024), including binaries originating from cosmological distances (Haster *et al.*, 2020). This wealth of information can lead to uncertainties of $\mathcal{O}(10–100)$ m in the radius measurement (Chatziioannou, 2022; Iacovelli *et al.*, 2023; Puecher, Samajdar, and Dietrich, 2023; Rose *et al.*, 2023; Huxford *et al.*, 2024) from gravitational-wave data alone and enable novel studies that are inaccessible to current-generation detectors. For example, louder signals allow us to place constraints on the tidal properties of increasingly massive neutron stars (Chen *et al.*, 2020) and gain access to the postmerger emission and the complementary information it includes (Torres-Rivas *et al.*, 2019; Breschi, Carullo, and Bernuzzi, 2023; Prakash *et al.*, 2024). Detections across the mass spectrum will also enable a detailed exploration of the EOS across masses and the possibility of deviations from the hadronic expectation of almost-constant radius that could signal a phase transition (Chatziioannou *et al.*, 2015; Han and Steiner, 2019; Chatziioannou and Han, 2020; Pang *et al.*, 2020; Essick *et al.*, 2023).

With an increased measurement precision, either from a few loud sources or by combining thousands of quieter sources, a number of challenges emerge. Inferring the neutron-star masses and tidal parameter hinges on accurate waveform models that can coherently track the signal phase evolution through the late inspiral stages and merger. Currently available waveform models are robust for the signal-to-noise ratio of GW170817, but systematics in modeling both the point particle and the tidal sector need to be continuously addressed as the sensitivity improves (Dudi *et al.*, 2018; Samajdar and Dietrich, 2018, 2019; Pürrer and Haster, 2020; Gamba *et al.*, 2021; Chatziioannou, 2022; Kunert *et al.*, 2022; Nagar *et al.*, 2023). This will necessitate improvements in both analytical waveform models and numerical relativity simulations. Moreover, neutron-star binaries will be observed for minutes to hours and multiple sources will coincide in the detector data stream (Relton and Raymond, 2021; Samajdar *et al.*, 2021; Pizzati *et al.*, 2022). Data analysis techniques that simultaneously analyze multiple signals (and other data components such as the detector noise) will need to be developed (Pizzati *et al.*, 2022; Alvey *et al.*, 2023; Janquart *et al.*, 2023). The time-frequency density of signals is not expected to be high enough to lead to Gaussian confusion noise (Johnson, Chatziioannou, and Farr, 2024), suggesting that techniques being developed to address much worse confusion noise can be adopted (Littenberg and Cornish, 2023).

The systematic uncertainties that complicate the determination of the relationship between pressure and energy density are unlikely to be easily resolved. If GW mergers cover a sufficiently large range of neutron-star masses, then enough merger events loud enough to permit measurement of the tidal deformability will lead to a determination of the pressure–energy density relation. In that case a combination of GW observations and x-ray observations will lead to a better understanding of neutron-star structure and the neutron-star population. X-ray spectroscopy is also critical for determining other aspects of dense matter, including the nature of the neutron-star crust and the composition of the core.

Future multimessenger observations of compact binary mergers have the potential to provide stringent constraints on the equation of state. However, these constraints are currently dominated by systematic uncertainties arising both from the incomplete coverage of the binary parameter space with simulations (Breschi *et al.*, 2019; Henkel *et al.*, 2023) and from the intrinsic uncertainties in the simulations (Zappa *et al.*, 2023; Foucart *et al.*, 2024). On the one hand, simulations with accurate neutrino transport (Foucart, 2023) accounting for neutrino quantum-kinetic effects (Li and Siegel, 2021; Just *et al.*, 2022; Grohs *et al.*, 2023) and magnetohydrodynamical turbulence and dynamo action (Palenzuela, Liebling, and Miñano, 2022; Kiuchi *et al.*, 2024; Radice and Hawke, 2024) are urgently needed. On the other hand, extensive campaigns of simulations are needed (Radice, Perego, Hotokezaka *et al.*, 2018; Nedora *et al.*, 2021; Camilletti *et al.*, 2022; Dudi *et al.*, 2022; Martineau *et al.*, 2024).

Though only upper limits have been placed on the gravitational-wave emission of isolated pulsars, those upper limits are reaching the level of 10^{-8} in ellipticity (Abbott *et al.*, 2022) and are becoming competitive with proposed theoretical upper limits that depend on the equation of state and the properties of the crust (Krastev, Li, and Worley, 2008; Johnson-McDaniel and Owen, 2013). See Haskell and Bejger (2023) and Riles (2023) for comprehensive reviews that discuss how tighter upper limits and any eventual detections would be able to constrain the equation of state.

Direct mass constraints from radio observations will improve with the development of new instrumentation. Future facilities such as ngVLA, SKA, and DSA-2000 will provide opportunities for more frequent and more precise timing observations, both of which are critical for constraining post-Keplerian orbital parameters. New facilities will also allow for deeper searches for new millisecond pulsars during which many high-mass neutron stars might be discovered. New "ultrawideband" receivers such as those developed for the Parkes and Green Bank radio telescopes will also improve timing precision. As pulsar timing array datasets grow, slowly varying orbital parameters will become increasingly well measured, meaning that post-Keplerian effects will be measured more precisely. Future observations will also provide improved inputs for parameters used as priors for pulse-profile modeling—and possibly even for isolated pulsars [where radio polarimetry with the rotating-vector model

may help determine the pulsar inclination (Desvignes *et al.*, 2019)].

There are also good prospects for measuring the neutron-star moment of inertia, another EOS-dependent quantity (Lattimer and Schutz, 2005). The periastron advance of compact relativistic binary pulsars is affected by a Lense-Thirring contribution that depends on pulsar geometry and the moment of inertia (Damour and Schafer, 1988). First limits have now been placed on this quantity (Kramer *et al.*, 2021), and future facilities like SKA are expected to deliver much tighter measurements (Hu *et al.*, 2020).

NICER has built up more data for pulse profile modeling on the brightest rotation-powered millisecond x-ray pulsars. This will lead to improved constraints on the sources for which results have already been published, and analysis will also be completed for several new sources, including the $1.9M_{\odot}$ source PSR J1614–2230 (Agazie *et al.*, 2023a). One challenge that is emerging is how to handle multimodality and how to select between two good but different solutions. One option may be to rely more heavily on the sources with mass priors from radio timing and to seek consistent solutions for the other sources. The large-area x-ray telescope NewAthena (Cruise *et al.*, 2025), due for launch in the 2030s, will enable us to study fainter rotation-powered millisecond pulsars, including several with mass priors already known from radio timing, and offer the prospect of new sources with mass priors being identified by facilities such as the SKA. Background for a mission like NewAthena will be much lower than for NICER and will be measurable directly from the observations since NewAthena is an x-ray imaging instrument, which will help to improve the constraints. The largest challenge for pulse-profile modeling is probably the surface pattern uncertainty. Better coupling to magnetosphere and multiwavelength pulsar emission models may help to reduce this (Chen, Yuan, and Vasilopoulos, 2020; Kalapotharakos *et al.*, 2021; Pétri *et al.*, 2023).

Pulse-profile modeling is also being extended to other classes of rapidly rotating neutron stars with nonuniform surface emission: thermonuclear burst oscillation sources (Lo *et al.*, 2013; Miller and Lamb, 2015; Kini *et al.*, 2023, 2024; Kini, Salmi *et al.*, 2024) and accretion-powered millisecond pulsars, where data from x-ray polarimetry missions such as IXPE can help to reduce uncertainties relating to geometry (Salmi, Nättilä, and Poutanen, 2018; Salmi *et al.*, 2021, 2025; Dorsman *et al.*, 2025; Papitto *et al.*, 2025). While these sources tend to spin faster than the rotation-powered millisecond pulsars being studied by NICER (enhancing the relativistic effects that pulse-profile modeling exploits), there are complicating factors such as hot spot variability and additional sources of x-ray emission such as the accretion disk that need to be included in the model. One benefit of accreting neutron stars is that one can apply different mass-radius inference techniques to the same star (for example, there are stars that have both accretion-powered pulsations and thermonuclear burst oscillations), which will help uncover systematic errors. And with a sufficiently large population of sources, one can compare the results from pulse-profile modeling for the accreting stars to those from the rotation-powered millisecond pulsars, and the EOS constraints from pulse-profile modeling could be compared to those derived from gravitational waves. All of these things will further reduce systematic errors.

ACKNOWLEDGMENTS

K. C. acknowledges support from the U.S. Department of Energy under Award No. DE-SC0023101 and the Sloan Foundation. A. L. W. acknowledges support from ERC Consolidator Grant No. 865768 AEONS and NWO ENW-XL Grant No. OCENW.XL21.XL21.038, "Probing the phase diagram of quantum chromodynamics." D. R. acknowledges funding from the U.S. Department of Energy, Office of Science, Division of Nuclear Physics, under Awards No. DE-SC0021177 and No. DE-SC0024388; from the National Science Foundation under Grants No. PHY-2011725, No. PHY-2020275, No. PHY-2116686, and No. AST-2108467; and from the Sloan Foundation. The work of S. G. and I. T. is supported by the U.S. Department of Energy, Office of Nuclear Physics, under Contract No. DE-AC52-06NA25396, and by the Office of Advanced Scientific Computing Research, Scientific Discovery, through the Advanced Computing (SciDAC) NUCLEI program. S. G. is also supported by the Network for Neutrinos, Nuclear Astrophysics and Symmetries (N3AS), through National Science Foundation Physics Frontier Center Award No. PHY-2020275. H. T. C. acknowledges support from the U.S. Naval Research Laboratory, where basic research in pulsar astronomy is supported by ONR 6.1 funding. A. W. S. acknowledges support from NSF Grants No. PHY-2116686 and No. AST 22-06322 and the U.S. DOE, Office of Nuclear Physics.

REFERENCES

Aasi, J., *et al.* (LIGO Scientific Collaboration), 2015, Classical Quantum Gravity **32**, 074001.

Abac, A., T. Dietrich, A. Buonanno, J. Steinhoff, and M. Ujevic, 2024, Phys. Rev. D **109**, 024062.

Abac, A. G., *et al.* (LIGO Scientific, Virgo, KAGRA, and VIRGO Collaborations), 2024, Astrophys. J. Lett. **970**, L34.

Abbott, B. P., *et al.* (LIGO Scientific and Virgo Collaborations), 2016, Phys. Rev. Lett. **116**, 061102.

Abbott, B. P., *et al.* (LIGO Scientific and Virgo Collaborations), 2017a, Phys. Rev. Lett. **119**, 161101.

Abbott, B. P., *et al.* (LIGO Scientific and Virgo Collaborations), 2017b, Phys. Rev. Lett. **119**, 161101.

Abbott, B. P., *et al.* (LIGO Scientific and Virgo Collaborations), 2017c, Astrophys. J. Lett. **851**, L16.

Abbott, B. P., *et al.* [LIGO Scientific Collaboration, Virgo Collaboration, Fermi GBM Collaboration, INTEGRAL Collaboration, IceCube Collaboration, AstroSat Cadmium Zinc Telluride Imager Team, IPN Collaboration, Insight-Hxmt Collaboration, ANTARES Collaboration, Swift Collaboration, AGILE Team, 1M2H Team, Dark Energy Camera GW-EM Collaboration, DES Collaboration, DLT40 Collaboration, GRAWITA Collaboration, Fermi-LAT Collaboration, ATCA Collaboration, ASKAP Collaboration, Las Cumbres Observatory Group, OzGrav Collaboration, DWF Collaboration (Deeper Wider Faster Program), AST3 Collaboration, CAASTRO Collaboration, VINROUGE Collaboration, MASTER Collaboration, J-GEM Collaboration, GROWTH Collaboration, JAGWAR Collaboration, CaltechNRAO Collaboration, TTU-NRAO

Collaboration, NuSTAR Collaboration, Pan-STARRS Collaboration, MAXI Team, TZAC Consortium, KU, Nordic Optical Telescope Collaboration, ePESSTO Collaboration, GROND Collaboration, Texas Tech University, SALT Group, TOROS Collaboration, BOOTES Collaboration, MWA Collaboration, CALET Collaboration, IKI-GW Follow-up Collaboration, H.E.S.S. Collaboration, LOFAR Collaboration, LWA Collaboration, HAWC Collaboration, Pierre Auger Collaboration, ALMA Collaboration, Euro VLBI Team, Pi of Sky Collaboration, Chandra Team at McGill University, DFN Collaboration, ATLAS Telescope Collaboration, High Time Resolution Universe Survey, RIMAS Collaboration, RATIR Collaboration, and SKA South Africa/MeerKAT Collaboration], 2017d, Astrophys. J. Lett. **848**, L12.

Abbott, B. P., *et al.* (LIGO Scientific, Virgo, Fermi-GBM, and INTEGRAL Collaborations), 2017e, Astrophys. J. Lett. **848**, L13.

Abbott, B. P., *et al.* (KAGRA, LIGO Scientific, Virgo, and VIRGO Collaborations), 2018a, Living Rev. Relativity **21**, 3.

Abbott, B. P., *et al.* (LIGO Scientific and Virgo Collaborations), 2018b, Phys. Rev. Lett. **121**, 161101.

Abbott, B. P., *et al.* (LIGO Scientific and Virgo Collaborations), 2019a, Phys. Rev. X **9**, 011001.

Abbott, B. P., *et al.* (LIGO Scientific and Virgo Collaborations), 2019b, Astrophys. J. **875**, 160.

Abbott, B. P., *et al.* (LIGO Scientific and Virgo Collaborations), 2019c, Phys. Rev. Lett. **123**, 161102.

Abbott, B. P., *et al.* (LIGO Scientific and Virgo Collaborations), 2020a, Astrophys. J. Lett. **892**, L3.

Abbott, R., *et al.* (LIGO Scientific and Virgo Collaborations), 2020b, Astrophys. J. Lett. **896**, L44.

Abbott, R., *et al.* (LIGO Scientific and Virgo Collaborations), 2021a, SoftwareX **13**, 100658.

Abbott, R., *et al.* (LIGO Scientific, KAGRA, and VIRGO Collaborations), 2021b, Astrophys. J. Lett. **915**, L5.

Abbott, R., *et al.* (LIGO Scientific, VIRGO, and KAGRA Collaborations), 2022, Astrophys. J. **935**, 1.

Abbott, R., *et al.* (KAGRA, VIRGO, and LIGO Scientific Collaborations), 2023a, Phys. Rev. X **13**, 041039.

Abbott, R., *et al.* (KAGRA, VIRGO, and LIGO Scientific Collaborations), 2023b, Phys. Rev. X **13**, 011048.

Abbott, R., *et al.* (LIGO Scientific, VIRGO, and KAGRA Collaborations), 2023c, Mon. Not. R. Astron. Soc. **524**, 5984; **526**, 6234 (E) (2023).

Abdelsalhin, T., L. Gualtieri, and P. Pani, 2018, Phys. Rev. D **98**, 104046.

Acernese, F., *et al.* (VIRGO Collaboration), 2015, Classical Quantum Gravity **32**, 024001.

Ackley, K., *et al.*, 2020, Publ. Astron. Soc. Aust. **37**, e047.

Adhikari, D., *et al.* (PREX Collaboration), 2021, Phys. Rev. Lett. **126**, 172502.

Adhikari, D., *et al.* (CREX Collaboration), 2022, Phys. Rev. Lett. **129**, 042501.

Adhikari, R. X., *et al.* (LIGO Collaboration), 2020, Classical Quantum Gravity **37**, 165003.

Agazie, G., *et al.* (Nanograv Collaboration), 2023a, Astrophys. J. Lett. **951**, L9.

Agazie, G., *et al.* (Nanograv Collaboration), 2023b, Astrophys. J. Lett. **951**, L8.

Aharonian, F., *et al.* (H.E.S.S. Collaboration), 2023, Nat. Astron. **7**, 1341.

Ai, S., H. Gao, and B. Zhang, 2020, Astrophys. J. **893**, 146.

Ai, S., H. Gao, and B. Zhang, 2024, arXiv:2405.00638.

Aichelin, J., A. Rosenhauer, G. Peilert, H. Stoecker, and W. Greiner, 1987, Phys. Rev. Lett. **58**, 1926.

Akmal, A., V. R. Pandharipande, and D. G. Ravenhall, 1998, Phys. Rev. C **58**, 1804.

Alford, M. G., S. Han, and M. Prakash, 2013, Phys. Rev. D **88**, 083013.

Alford, M. G., A. Schmitt, K. Rajagopal, and T. Schäfer, 2008, Rev. Mod. Phys. **80**, 1455.

AlGendy, M., and S. M. Morsink, 2014, Astrophys. J. **791**, 78.

Alizai, K., *et al.*, 2023, Mon. Not. R. Astron. Soc. **521**, 3608.

Al-Mamun, M., A. W. Steiner, J. Nättilä, J. Lange, R. O'Shaughnessy, I. Tews, S. Gandolfi, C. Heinke, and S. Han, 2021, Phys. Rev. Lett. **126**, 061101.

Alsing, J., H. O. Silva, and E. Berti, 2018, Mon. Not. R. Astron. Soc. **478**, 1377.

Alvey, J., U. Bhardwaj, S. Nissanke, and C. Weniger, 2023, arXiv:2308.06318.

Andersson, N., 2021, Universe **7**, 17.

Annala, E., T. Gorda, A. Kurkela, J. Nättilä, and A. Vuorinen, 2020, Nat. Phys. **16**, 907.

Annala, E., T. Gorda, A. Kurkela, and A. Vuorinen, 2018, Phys. Rev. Lett. **120**, 172703.

Antoniadis, J., T. M. Tauris, F. Ozel, E. Barr, D. J. Champion, and P. C. C. Freire, 2016, arXiv:1605.01665.

Antoniadis, J., *et al.*, 2013, Science **340**, 1233232.

Antoniadis, J., *et al.* (EPTA Collaboration), 2023a, Astron. Astrophys. **678**, A48.

Antoniadis, J., *et al.* (EPTA and InPTA Collaborations), 2023b, Astron. Astrophys. **678**, A50.

Archibald, A. M., N. V. Gusinskaia, J. W. T. Hessels, A. T. Deller, D. L. Kaplan, D. R. Lorimer, R. S. Lynch, S. M. Ransom, and I. H. Stairs, 2018, Nature (London) **559**, 73.

Baade, W., and F. Zwicky, 1934, Proc. Natl. Acad. Sci. U.S.A. **20**, 259.

Baardsen, G., A. Ekström, G. Hagen, and M. Hjorth-Jensen, 2013, Phys. Rev. C **88**, 054312.

Backer, D. C., S. R. Kulkarni, and J. H. Taylor, 1983, Nature (London) **301**, 314.

Baillot d'Etivaux, N., S. Guillot, J. Margueron, N. Webb, M. Catelan, and A. Reisenegger, 2019, Astrophys. J. **887**, 48.

Baiotti, L., 2019, Prog. Part. Nucl. Phys. **109**, 103714.

Baiotti, L., and L. Rezzolla, 2017, Rep. Prog. Phys. **80**, 096901.

Baldo, M., A. Polls, A. Rios, H.-J. Schulze, and I. Vidaña, 2012, Phys. Rev. C **86**, 064001.

Baroni, A., *et al.*, 2018, Phys. Rev. C **98**, 044003.

Barr, E. D., *et al.*, 2024, Science **383**, 275.

Bassa, C. G., *et al.*, 2017, Astrophys. J. Lett. **846**, L20.

Bauböck, M., F. Özel, D. Psaltis, and S. M. Morsink, 2015, Astrophys. J. **799**, 22.

Bauböck, M., D. Psaltis, F. Özel, and T. Johannsen, 2012, Astrophys. J. **753**, 175.

Baumgarte, T. W., and S. L. Shapiro, 2021, *Numerical Relativity: Starting from Scratch* (Cambridge University Press, Cambridge, England).

Bauswein, A., N.-U. F. Bastian, D. B. Blaschke, K. Chatziioannou, J. A. Clark, T. Fischer, and M. Oertel, 2019, Phys. Rev. Lett. **122**, 061102.

Bauswein, A., T. W. Baumgarte, and H. T. Janka, 2013, Phys. Rev. Lett. **111**, 131101.

Bauswein, A., S. Blacker, G. Lioutas, T. Soultanis, V. Vijayan, and N. Stergioulas, 2021, Phys. Rev. D **103**, 123004.

Bauswein, A., S. Blacker, V. Vijayan, N. Stergioulas, K. Chatziioannou, J. A. Clark, N.-U. F. Bastian, D. B. Blaschke, M. Cierniak, and T. Fischer, 2020, Phys. Rev. Lett. **125**, 141103.

Bauswein, A., S. Goriely, and H. T. Janka, 2013, Astrophys. J. **773**, 78.

Bauswein, A., H. T. Janka, and R. Oechslin, 2010, Phys. Rev. D **82**, 084043.

Bauswein, A., O. Just, H.-T. Janka, and N. Stergioulas, 2017, Astrophys. J. Lett. **850**, L34.

Bauswein, A., and N. Stergioulas, 2015, Phys. Rev. D **91**, 124056.

Bauswein, A., and N. Stergioulas, 2019, J. Phys. G **46**, 113002.

Baym, G., T. Hatsuda, T. Kojo, P. D. Powell, Y. Song, and T. Takatsuka, 2018, Rep. Prog. Phys. **81**, 056902.

Beane, S. R., P. F. Bedaque, T. C. Luu, K. Orginos, E. Pallante, A. Parreno, and M. J. Savage (NPLQCD Collaboration), 2007, Nucl. Phys. **794A**, 62.

Becker, W., and J. Trümper, 1993, Nature (London) **365**, 528.

Belian, R. D., J. P. Conner, and W. D. Evans, 1976, Astrophys. J. Lett. **206**, L135.

Beloborodov, A. M., 2002, Astrophys. J. Lett. **566**, L85.

Bender, M., P.-H. Heenen, and P.-G. Reinhard, 2003, Rev. Mod. Phys. **75**, 121.

Beniamini, P., and W. Lu, 2021, Astrophys. J. **920**, 109.

Bernard, V., E. Epelbaum, H. Krebs, and U. G. Meissner, 2011, Phys. Rev. C **84**, 054001.

Bernard, V., E. Epelbaum, H. Krebs, and U.-G. Meissner, 2008, Phys. Rev. C **77**, 064004.

Bernuzzi, S., 2020, Gen. Relativ. Gravit. **52**, 108.

Bernuzzi, S., and T. Dietrich, 2016, Phys. Rev. D **94**, 064062.

Bernuzzi, S., A. Nagar, T. Dietrich, and T. Damour, 2015, Phys. Rev. Lett. **114**, 161103.

Bernuzzi, S., A. Nagar, M. Thierfelder, and B. Brugmann, 2012, Phys. Rev. D **86**, 044030.

Bernuzzi, S., D. Radice, C. D. Ott, L. F. Roberts, P. Moesta, and F. Galeazzi, 2016, Phys. Rev. D **94**, 024023.

Bernuzzi, S., *et al.*, 2020, Mon. Not. R. Astron. Soc. **497**, 1488.

Bhattacharya, D., and E. P. J. van den Heuvel, 1991, Phys. Rep. **203**, 1.

Bhattacharyya, S., T. E. Strohmayer, M. C. Miller, and C. B. Markwardt, 2005, Astrophys. J. **619**, 483.

Bildsten, L., *et al.*, 1997, Astrophys. J. Suppl. Ser. **113**, 367.

Bilous, A. V., *et al.*, 2019, Astrophys. J. Lett. **887**, L23.

Binnington, T., and E. Poisson, 2009, Phys. Rev. D **80**, 084018.

Birkhan, J., *et al.*, 2017, Phys. Rev. Lett. **118**, 252501.

Blanchet, L., 2014, Living Rev. Relativity **17**, 2.

Bogdanov, S., 2013, Astrophys. J. **762**, 96.

Bogdanov, S., *et al.*, 2019a, Astrophys. J. Lett. **887**, L25.

Bogdanov, S., *et al.*, 2019b, Astrophys. J. Lett. **887**, L26.

Bogdanov, S., *et al.*, 2021, Astrophys. J. Lett. **914**, L15.

Bogner, S. K., R. J. Furnstahl, and R. J. Perry, 2007, Phys. Rev. C **75**, 061001.

Bogner, S. K., T. T. S. Kuo, and A. Schwenk, 2003, Phys. Rep. **386**, 1.

Bohé, A., G. Faye, S. Marsat, and E. K. Porter, 2015, Classical Quantum Gravity **32**, 195010.

Bombaci, I., A. Drago, D. Logoteta, G. Pagliara, and I. Vidaña, 2021, Phys. Rev. Lett. **126**, 162702.

Borhanian, S., and B. S. Sathyaprakash, 2024, Phys. Rev. D **110**, 083040.

Bose, S., K. Chakravarti, L. Rezzolla, B. S. Sathyaprakash, and K. Takami, 2018, Phys. Rev. Lett. **120**, 031102.

Boyle, M., *et al.*, 2019, Classical Quantum Gravity **36**, 195006.

Braje, T. M., R. W. Romani, and K. P. Rauch, 2000, Astrophys. J. **531**, 447.

Breschi, M., S. Bernuzzi, F. Zappa, M. Agathos, A. Perego, D. Radice, and A. Nagar, 2019, Phys. Rev. D **100**, 104029.

Breschi, M., G. Carullo, and S. Bernuzzi, 2023, Particles **6**, 731.

Breschi, M., R. Gamba, G. Carullo, D. Godzieba, S. Bernuzzi, A. Perego, and D. Radice, 2024, Astron. Astrophys. **689**, A51.

Brown, E. F., L. Bildsten, and R. E. Rutledge, 1998, Astrophys. J. **504**, L95.

Brown, E. F., and A. Cumming, 2009, Astrophys. J. **698**, 1020.

Brown, S. M., C. D. Capano, and B. Krishnan, 2022, Astrophys. J. **941**, 98.

Bugner, M., T. Dietrich, S. Bernuzzi, A. Weyhausen, and B. Brügmann, 2016, Phys. Rev. D **94**, 084004.

Bulgac, A., J. E. Drut, and P. Magierski, 2006, Phys. Rev. Lett. **96**, 090404.

Buonanno, A., B. Iyer, E. Ochsner, Y. Pan, and B. S. Sathyaprakash, 2009, Phys. Rev. D **80**, 084043.

Burgio, G. F., H. J. Schulze, I. Vidaña, and J. B. Wei, 2021, Prog. Part. Nucl. Phys. **120**, 103879.

Burwitz, V., V. E. Zavlin, R. Neuhäuser, P. Predehl, J. Trümper, and A. C. Brinkman, 2001, Astron. Astrophys. **379**, L35.

Cadeau, C., S. M. Morsink, D. Leahy, and S. S. Campbell, 2007, Astrophys. J. **654**, 458.

Camilletti, A., L. Chiesa, G. Ricigliano, A. Perego, L. C. Lippold, S. Padamata, S. Bernuzzi, D. Radice, D. Logoteta, and F. M. Guercilena, 2022, Mon. Not. R. Astron. Soc. **516**, 4760.

Capano, C. D., I. Tews, S. M. Brown, B. Margalit, S. De, S. Kumar, D. A. Brown, B. Krishnan, and S. Reddy, 2020, Nat. Astron. **4**, 625.

Caplan, M. E., and C. J. Horowitz, 2017, Rev. Mod. Phys. **89**, 041002.

Carbone, A., A. Cipollone, C. Barbieri, A. Rios, and A. Polls, 2013, Phys. Rev. C **88**, 054326.

Carbone, A., A. Polls, and A. Rios, 2013, Phys. Rev. C **88**, 044302.

Carbone, A., A. Rios, and A. Polls, 2014, Phys. Rev. C **90**, 054322.

Carlson, J., S.-Y. Chang, V. R. Pandharipande, and K. E. Schmidt, 2003, Phys. Rev. Lett. **91**, 050401.

Carlson, J., S. Gandolfi, and A. Gezerlis, 2012, Prog. Theor. Exp. Phys. 01A209.

Carlson, J., S. Gandolfi, F. Pederiva, S. C. Pieper, R. Schiavilla, K. E. Schmidt, and R. B. Wiringa, 2015, Rev. Mod. Phys. **87**, 1067.

Carlson, J., S. Gandolfi, K. E. Schmidt, and S. Zhang, 2011, Phys. Rev. A **84**, 061602.

Carlson, J., and S. Reddy, 2005, Phys. Rev. Lett. **95**, 060401.

Carney, M. F., L. E. Wade, and B. S. Irwin, 2018, Phys. Rev. D **98**, 063004.

Carr, B. J., and S. W. Hawking, 1974, Mon. Not. R. Astron. Soc. **168**, 399.

Carriere, J., C. J. Horowitz, and J. Piekarewicz, 2003, Astrophys. J. **593**, 463.

Carson, Z., K. Chatziioannou, C.-J. Haster, K. Yagi, and N. Yunes, 2019, Phys. Rev. D **99**, 083016.

Chatterjee, D., and I. Vidaña, 2016, Eur. Phys. J. A **52**, 29.

Chatziioannou, K., 2020, Gen. Relativ. Gravit. **52**, 109.

Chatziioannou, K., 2022, Phys. Rev. D **105**, 084021.

Chatziioannou, K., J. A. Clark, A. Bauswein, M. Millhouse, T. B. Littenberg, and N. Cornish, 2017, Phys. Rev. D **96**, 124035.

Chatziioannou, K., and W. M. Farr, 2020, Phys. Rev. D **102**, 064063.

Chatziioannou, K., and S. Han, 2020, Phys. Rev. D **101**, 044019.

Chatziioannou, K., C.-J. Haster, and A. Zimmerman, 2018, Phys. Rev. D **97**, 104036.

Chatziioannou, K., K. Yagi, A. Klein, N. Cornish, and N. Yunes, 2015, Phys. Rev. D **92**, 104008.

Chen, A., N. K. Johnson-McDaniel, T. Dietrich, and R. Dudi, 2020, Phys. Rev. D **101**, 103008.

Chen, A. Y., Y. Yuan, and G. Vasilopoulos, 2020, Astrophys. J. Lett. **893**, L38.

Chen, H.-Y., and K. Chatziioannou, 2020, Astrophys. J. Lett. **893**, L41.

Chia, H. S., 2021, Phys. Rev. D **104**, 024013.

Choudhury, D., *et al.*, 2024, Astrophys. J. Lett. **971**, L20.

Christian, J.-E., J. Schaffner-Bielich, and S. Rosswog, 2024, Phys. Rev. D **109**, 063035.

Clark, J., A. Bauswein, L. Cadonati, H. T. Janka, C. Pankow, and N. Stergioulas, 2014, Phys. Rev. D **90**, 062004.

Clark, J. A., A. Bauswein, N. Stergioulas, and D. Shoemaker, 2016, Classical Quantum Gravity **33**, 085003.

Çokluk, K. A., K. Yakut, and B. Giacomazzo, 2024, Mon. Not. R. Astron. Soc. **527**, 8043.

Coughlin, M. W., T. Dietrich, B. Margalit, and B. D. Metzger, 2019, Mon. Not. R. Astron. Soc. **489**, L91.

Criswell, A. W., J. Miller, N. Woldemariam, T. Soultanis, A. Bauswein, K. Chatziioannou, M. W. Coughlin, G. Jones, and V. Mandic, 2023, Phys. Rev. D **107**, 043021.

Cromartie, H. T., *et al.*, 2020, Nat. Astron. **4**, 72.

Cruise, M., *et al.*, 2025, arXiv:2501.03100.

Dai, Z. G., and T. Lu, 1998a, Astron. Astrophys. **333**, L87, https://inspirehep.net/literature/490763.

Dai, Z. G., and T. Lu, 1998b, Phys. Rev. Lett. **81**, 4301.

Dai, Z.-G., X. Y. Wang, X. F. Wu, and B. Zhang, 2006, Science **311**, 1127.

Damour, T., and A. Nagar, 2009, Phys. Rev. D **80**, 084035.

Damour, T., A. Nagar, and L. Villain, 2012, Phys. Rev. D **85**, 123007.

Damour, T., and G. Schafer, 1988, Nuovo Cimento Soc. Ital. Fis. **101B**, 127.

Danielewicz, P., and G. Bertsch, 1991, Nucl. Phys. **A533**, 712.

Danielewicz, P., R. Lacey, and W. G. Lynch, 2002, Science **298**, 1592.

Day, B. D., and R. B. Wiringa, 1985, Phys. Rev. C **32**, 1057.

De, S., D. Finstad, J. M. Lattimer, D. A. Brown, E. Berger, and C. M. Biwer, 2018, Phys. Rev. Lett. **121**, 091102; **121**, 259902(E) (2018).

Demorest, P. B., T. Pennucci, S. M. Ransom, M. S. E. Roberts, and J. W. T. Hessels, 2010, Nature (London) **467**, 1081.

Deppe, N., *et al.*, 2024, arXiv:2406.19038.

Desvignes, G., M. Kramer, K. Lee, J. van Leeuwen, I. Stairs, A. Jessner, I. Cognard, L. Kasian, A. Lyne, and B. W. Stappers, 2019, Science **365**, 1013.

Dexheimer, V., R. O. Gomes, T. Klähn, S. Han, and M. Salinas, 2021, Phys. Rev. C **103**, 025808.

Dhani, A., D. Radice, J. Schütte-Engel, S. Gardner, B. Sathyaprakash, D. Logoteta, A. Perego, and R. Kashyap, 2024, Phys. Rev. D **109**, 044071.

Dietrich, T., S. Bernuzzi, and W. Tichy, 2017, Phys. Rev. D **96**, 121501.

Dietrich, T., M. W. Coughlin, P. T. H. Pang, M. Bulla, J. Heinzel, L. Issa, I. Tews, and S. Antier, 2020, Science **370**, 1450.

Dietrich, T., T. Hinderer, and A. Samajdar, 2021, Gen. Relativ. Gravit. **53**, 27.

Dietrich, T., A. Samajdar, S. Khan, N. K. Johnson-McDaniel, R. Dudi, and W. Tichy, 2019, Phys. Rev. D **100**, 044003.

Dietrich, T., M. Ujevic, W. Tichy, S. Bernuzzi, and B. Bruegmann, 2017, Phys. Rev. D **95**, 024029.

Dietrich, T., *et al.*, 2019, Phys. Rev. D **99**, 024029.

Dimple, K. Misra, and K. G. Arun, 2023, Astrophys. J. Lett. **949**, L22.

Dittmann, A. J., *et al.*, 2024, Astrophys. J. **974**, 295.

Dorsman, B., *et al.*, 2025, Mon. Not. R. Astron. Soc. **538**, 2853.

Doulis, G., F. Atteneder, S. Bernuzzi, and B. Brügmann, 2022, Phys. Rev. D **106**, 024001.

Drischler, C., R. J. Furnstahl, J. A. Melendez, and D. R. Phillips, 2020, Phys. Rev. Lett. **125**, 202702.

Drischler, C., K. Hebeler, and A. Schwenk, 2019, Phys. Rev. Lett. **122**, 042501.

Drischler, C., J. W. Holt, and C. Wellenhofer, 2021, Annu. Rev. Nucl. Part. Sci. **71**, 403.

Droz, S., D. J. Knapp, E. Poisson, and B. J. Owen, 1999, Phys. Rev. D **59**, 124016.

Dudi, R., A. Adhikari, B. Brügmann, T. Dietrich, K. Hayashi, K. Kawaguchi, K. Kiuchi, K. Kyutoku, M. Shibata, and W. Tichy, 2022, Phys. Rev. D **106**, 084039.

Dudi, R., F. Pannarale, T. Dietrich, M. Hannam, S. Bernuzzi, F. Ohme, and B. Brügmann, 2018, Phys. Rev. D **98**, 084061.

Dumbser, M., O. Zanotti, E. Gaburro, and I. Peshkov, 2024, J. Comput. Phys. **504**, 112875.

Dunham, S. J., E. Endeve, A. Mezzacappa, J. Buffaloe, and K. Holley-Bockelmann, 2020, J. Phys. Conf. Ser. **1623**, 012012.

Dyhdalo, A., R. J. Furnstahl, K. Hebeler, and I. Tews, 2016, Phys. Rev. C **94**, 034001.

Easter, P. J., S. Ghonge, P. D. Lasky, A. R. Casey, J. A. Clark, F. H. Vivanco, and K. Chatziioannou, 2020, Phys. Rev. D **102**, 043011.

Ebisuzaki, T., T. Hanawa, and D. Sugimoto, 1983, Publ. Astron. Soc. Jpn. **35**, 17.

Eddins, A., K.-H. Lee, A. Corsi, I. Bartos, Z. Márka, and S. Márka, 2023, Astrophys. J. **948**, 125.

Ekström, A., G. Hagen, T. D. Morris, T. Papenbrock, and P. D. Schwartz, 2018, Phys. Rev. C **97**, 024332.

Ekström, A., G. R. Jansen, K. A. Wendt, G. Hagen, T. Papenbrock, B. D. Carlsson, C. Forssén, M. Hjorth-Jensen, P. Navrátil, and W. Nazarewicz, 2015, Phys. Rev. C **91**, 051301.

Ekström, A., *et al.*, 2013, Phys. Rev. Lett. **110**, 192502.

Elshamouty, K. G., C. O. Heinke, S. M. Morsink, S. Bogdanov, and A. L. Stevens, 2016, Astrophys. J. **826**, 162.

Entem, D. R., and R. Machleidt, 2003, Phys. Rev. C **68**, 041001.

Entem, D. R., R. Machleidt, and Y. Nosyk, 2017, Phys. Rev. C **96**, 024004.

Epelbaum, E., W. Glockle, and U.-G. Meissner, 2005, Nucl. Phys. **A747**, 362.

Epelbaum, E., H.-W. Hammer, and U.-G. Meißner, 2009, Rev. Mod. Phys. **81**, 1773.

Epelbaum, E., H. Krebs, and U.-G. Meißner, 2015a, Phys. Rev. Lett. **115**, 122301.

Epelbaum, E., H. Krebs, and U. G. Meißner, 2015b, Eur. Phys. J. A **51**, 53.

Espino, P. L., P. Hammond, D. Radice, S. Bernuzzi, R. Gamba, F. Zappa, L. F. L. Micchi, and A. Perego, 2024, Phys. Rev. Lett. **132**, 211001.

Essick, R., and P. Landry, 2020, Astrophys. J. **904**, 80.

Essick, R., P. Landry, and D. E. Holz, 2020, Phys. Rev. D **101**, 063007.

Essick, R., P. Landry, A. Schwenk, and I. Tews, 2021, Phys. Rev. C **104**, 065804.

Essick, R., I. Legred, K. Chatziioannou, S. Han, and P. Landry, 2023, Phys. Rev. D **108**, 043013.

Essick, R., I. Tews, P. Landry, and A. Schwenk, 2021, Phys. Rev. Lett. **127**, 192701.

Fan, Y.-Z., X.-F. Wu, and D.-M. Wei, 2013, Phys. Rev. D **88**, 067304.

Farah, A. M., M. Fishbach, R. Essick, D. E. Holz, and S. Galaudage, 2022, Astrophys. J. **931**, 108.

Farr, W. M., and K. Chatziioannou, 2020, Res. Notes Am. Astron. Soc. **4**, 65.

Fattoyev, F. J., C. J. Horowitz, J. Piekarewicz, and B. Reed, 2020, Phys. Rev. C **102**, 065805.

Favata, M., 2014, Phys. Rev. Lett. **112**, 101101.
Fishbach, M., R. Essick, and D. E. Holz, 2020, Astrophys. J. Lett. **899**, L8.
Flanagan, E. E., and T. Hinderer, 2008, Phys. Rev. D **77**, 021502.
Fonseca, E., *et al.*, 2016, Astrophys. J. **832**, 167.
Fonseca, E., *et al.*, 2021, Astrophys. J. Lett. **915**, L12.
Forbes, M. M., S. Gandolfi, and A. Gezerlis, 2011, Phys. Rev. Lett. **106**, 235303.
Forbes, M. M., S. Gandolfi, and A. Gezerlis, 2012, Phys. Rev. A **86**, 053603.
Fore, B., and S. Reddy, 2020, Phys. Rev. C **101**, 035809.
Foucart, F., 2023, Living Rev. Comput. Astrophys. **9**, 1.
Foucart, F., L. Buchman, M. D. Duez, M. Grudich, L. E. Kidder, I. MacDonald, A. Mroue, H. P. Pfeiffer, M. A. Scheel, and B. Szilagyi, 2013, Phys. Rev. D **88**, 064017.
Foucart, F., P. C.-K. Cheong, M. D. Duez, L. E. Kidder, H. P. Pfeiffer, and M. A. Scheel, 2024, Phys. Rev. D **110**, 083028.
Foucart, F., M. D. Duez, A. Gudinas, F. Hebert, L. E. Kidder, H. P. Pfeiffer, and M. A. Scheel, 2019, Phys. Rev. D **100**, 104048.
Foucart, F., T. Hinderer, and S. Nissanke, 2018, Phys. Rev. D **98**, 081501.
Foucart, F., *et al.*, 2019, Phys. Rev. D **99**, 044008.
Freire, P. C. C., and N. Wex, 2010, Mon. Not. R. Astron. Soc. **409**, 199.
Fukushima, K., and C. Sasaki, 2013, Prog. Part. Nucl. Phys. **72**, 99.
Galloway, D. K., J. in 't Zand, J. Chenevez, H. Wörpel, L. Keek, L. Ootes, A. L. Watts, L. Gisler, C. Sanchez-Fernandez, and E. Kuulkers, 2020, Astrophys. J. Suppl. Ser. **249**, 32.
Gamba, R., and S. Bernuzzi, 2023, Phys. Rev. D **107**, 044014.
Gamba, R., S. Bernuzzi, and A. Nagar, 2021, Phys. Rev. D **104**, 084058.
Gamba, R., M. Breschi, S. Bernuzzi, M. Agathos, and A. Nagar, 2021, Phys. Rev. D **103**, 124015.
Gamba, R., *et al.*, 2023, arXiv:2307.15125.
Gandolfi, S., J. Carlson, and S. Reddy, 2012, Phys. Rev. C **85**, 032801.
Gandolfi, S., J. Carlson, S. Reddy, A. W. Steiner, and R. B. Wiringa, 2014, Eur. Phys. J. A **50**, 10.
Gandolfi, S., A. Gezerlis, and J. Carlson, 2015, Annu. Rev. Nucl. Part. Sci. **65**, 303.
Gandolfi, S., J. Lippuner, A. W. Steiner, I. Tews, X. Du, and M. Al-Mamun, 2019, J. Phys. G **46**, 103001.
Gandolfi, S., A. Lovato, J. Carlson, and K. E. Schmidt, 2014, Phys. Rev. C **90**, 061306(R).
Gandolfi, S., G. Palkanoglou, J. Carlson, A. Gezerlis, and K. E. Schmidt, 2022, Condens. Matter **7**, 19.
Gandolfi, S., K. E. Schmidt, and J. Carlson, 2011, Phys. Rev. A **83**, 041601.
Gao, H., X. Ding, X.-F. Wu, B. Zhang, and Z.-G. Dai, 2013, Astrophys. J. **771**, 86.
Gao, H., B. Zhang, H.-J. Lü, and Y. Li, 2017, Astrophys. J. **837**, 50.
Gao, W.-H., 2006, Chin. J. Astron. Astrophys. **6**, 513.
Gazit, D., S. Quaglioni, and P. Navratil, 2009, Phys. Rev. Lett. **103**, 102502; **122**, 029901(E) (2019).
Gendreau, K. C., *et al.*, 2016, in *Space Telescopes and Instrumentation 2016: Ultraviolet to Gamma Ray*, edited by J.-W. A. den Herder, T. Takahashi, and M. Bautz, SPIE Proceedings Vol. 9905 (SPIE—International Society for Optical Engineering, Bellingham, WA), p. 99051H.
Gezerlis, A., and J. Carlson, 2008, Phys. Rev. C **77**, 032801.
Gezerlis, A., and J. Carlson, 2010, Phys. Rev. C **81**, 025803.
Gezerlis, A., I. Tews, E. Epelbaum, M. Freunek, S. Gandolfi, K. Hebeler, A. Nogga, and A. Schwenk, 2014, Phys. Rev. C **90**, 054323.
Gezerlis, A., I. Tews, E. Epelbaum, S. Gandolfi, K. Hebeler, A. Nogga, and A. Schwenk, 2013, Phys. Rev. Lett. **111**, 032501.
Ghosh, A., C. S. Vaishnava, L. Resmi, K. Misra, K. G. Arun, A. Omar, and N. K. Chakradhari, 2024, Mon. Not. R. Astron. Soc. **527**, 8068.
Giacconi, R., H. Gursky, E. Kellogg, E. Schreier, and H. Tananbaum, 1971, Astrophys. J. Lett. **167**, L67.
Giorgini, S., L. P. Pitaevskii, and S. Stringari, 2008, Rev. Mod. Phys. **80**, 1215.
Glendenning, N. K., and S. A. Moszkowski, 1991, Phys. Rev. Lett. **67**, 2414.
Golomb, J., I. Legred, K. Chatziioannou, A. Abac, and T. Dietrich, 2024, Phys. Rev. D **110**, 063014.
Gonzalez, A., R. Gamba, M. Breschi, F. Zappa, G. Carullo, S. Bernuzzi, and A. Nagar, 2023, Phys. Rev. D **107**, 084026.
Gorda, T., O. Komoltsev, and A. Kurkela, 2023, Astrophys. J. **950**, 107.
Grace, B., K. Wette, and S. M. Scott, 2024, Phys. Rev. D **110**, 083016.
Greif, S. K., G. Raaijmakers, K. Hebeler, A. Schwenk, and A. L. Watts, 2019, Mon. Not. R. Astron. Soc. **485**, 5363.
Grindlay, J., H. Gursky, H. Schnopper, D. R. Parsignault, J. Heise, A. C. Brinkman, and J. Schrijver, 1976, Astrophys. J. Lett. **205**, L127.
Grohs, E., S. Richers, S. M. Couch, F. Foucart, J. P. Kneller, and G. C. McLaughlin, 2023, Phys. Lett. B **846**, 138210.
Guerra Chaves, A., and T. Hinderer, 2019, J. Phys. G **46**, 123002.
Guillot, S., M. Servillat, N. A. Webb, and R. E. Rutledge, 2013, Astrophys. J. **772**, 7.
Gupta, I., *et al.*, 2023, arXiv:2307.10421.
Haensel, P., and J. L. Zdunik, 2003, Astron. Astrophys. **404**, L33.
Hagen, G., T. Papenbrock, A. Ekström, K. A. Wendt, G. Baardsen, S. Gandolfi, M. Hjorth-Jensen, and C. J. Horowitz, 2014, Phys. Rev. C **89**, 014319.
Hammer, H.-W., A. Nogga, and A. Schwenk, 2013, Rev. Mod. Phys. **85**, 197.
Han, S., and A. W. Steiner, 2019, Phys. Rev. D **99**, 083014.
Harding, A. K., and A. G. Muslimov, 2001, Astrophys. J. **556**, 987.
Harry, I., and T. Hinderer, 2018, Classical Quantum Gravity **35**, 145010.
Haskell, B., and M. Bejger, 2023, Nat. Astron. **7**, 1160.
Haster, C.-J., K. Chatziioannou, A. Bauswein, and J. A. Clark, 2020, Phys. Rev. Lett. **125**, 261101.
Hatsuda, T., and T. Kunihiro, 1994, Phys. Rep. **247**, 221.
Hebeler, K., S. K. Bogner, R. J. Furnstahl, A. Nogga, and A. Schwenk, 2011, Phys. Rev. C **83**, 031301.
Hebeler, K., J. D. Holt, J. Menendez, and A. Schwenk, 2015, Annu. Rev. Nucl. Part. Sci. **65**, 457.
Hebeler, K., and A. Schwenk, 2010, Phys. Rev. C **82**, 014314.
Hébert, F., L. E. Kidder, and S. A. Teukolsky, 2018, Phys. Rev. D **98**, 044041.
Heinke, C. O., P. G. Jonker, R. Wijnands, C. J. Deloye, and R. E. Taam, 2009, Astrophys. J. **691**, 1035.
Heinke, C. O., G. B. Rybicki, R. Narayan, and J. E. Grindlay, 2006, Astrophys. J. **644**, 1090.
Henkel, A., F. Foucart, G. Raaijmakers, and S. Nissanke, 2023, Phys. Rev. D **107**, 063028.
Hesthaven, J., and T. Warburton, 2007, *Nodal Discontinuous Galerkin Methods: Algorithms, Analysis, and Applications, Texts in Applied Mathematics* (Springer, New York).
Hewish, A., S. J. Bell, J. D. H. Pilkington, P. F. Scott, and R. A. Collins, 1968, Nature (London) **217**, 709.
Hinderer, T., 2008, Astrophys. J. **677**, 1216; **697**, 964(E) (2009).

Hinderer, T., B. D. Lackey, R. N. Lang, and J. S. Read, 2010, Phys. Rev. D **81**, 123016.
Hinderer, T., *et al.*, 2016, Phys. Rev. Lett. **116**, 181101.
Ho, W. C. G., and C. O. Heinke, 2009, Nature (London) **462**, 71.
Ho, W. C. G., D. L. Kaplan, P. Chang, M. Van Adelsberg, and A. Y. Potekhin, 2007, Mon. Not. R. Astron. Soc. **375**, 821.
Hoferichter, M., J. Ruiz de Elvira, B. Kubis, and U.-G. Meißner, 2016, Phys. Rep. **625**, 1.
Hong, D. K., 2000, Phys. Lett. B **473**, 118.
Hoogkamer, M., Y. Kini, T. Salmi, A. L. Watts, and J. Buchner, 2025, Phys. Rev. D **112**, 023008.
Hoppe, J., C. Drischler, R. J. Furnstahl, K. Hebeler, and A. Schwenk, 2017, Phys. Rev. C **96**, 054002.
Horowitz, C., and B. D. Serot, 1981, Nucl. Phys. **A368**, 503.
Horowitz, C. J., M. A. Perez-Garcia, and J. Piekarewicz, 2004, Phys. Rev. C **69**, 045804.
Horowitz, C. J., and J. Piekarewicz, 2001, Phys. Rev. Lett. **86**, 5647.
Hotokezaka, K., K. Kiuchi, K. Kyutoku, H. Okawa, Y.-i. Sekiguchi, M. Shibata, and K. Taniguchi, 2013, Phys. Rev. D **87**, 024001.
Hotokezaka, K., K. Kyutoku, H. Okawa, M. Shibata, and K. Kiuchi, 2011, Phys. Rev. D **83**, 124008.
Hotokezaka, K., K. Kyutoku, Y.-i. Sekiguchi, and M. Shibata, 2016, Phys. Rev. D **93**, 064082.
Hu, B., *et al.*, 2022, Nat. Phys. **18**, 1196.
Hu, H., M. Kramer, N. Wex, D. J. Champion, and M. S. Kehl, 2020, Mon. Not. R. Astron. Soc. **497**, 3118.
Huang, Y.-J., L. Baiotti, T. Kojo, K. Takami, H. Sotani, H. Togashi, T. Hatsuda, S. Nagataki, and Y.-Z. Fan, 2022, Phys. Rev. Lett. **129**, 181101.
Hulse, R. A., and J. H. Taylor, 1975, Astrophys. J. Lett. **195**, L51.
Huth, L., I. Tews, J. E. Lynn, and A. Schwenk, 2017, Phys. Rev. C **96**, 054003.
Huth, S., C. Wellenhofer, and A. Schwenk, 2021, Phys. Rev. C **103**, 025803.
Huth, S., *et al.*, 2022, Nature (London) **606**, 276.
Huxford, R., R. Kashyap, S. Borhanian, A. Dhani, I. Gupta, and B. S. Sathyaprakash, 2024, Phys. Rev. D **109**, 103035.
Iacovelli, F., M. Mancarella, C. Mondal, A. Puecher, T. Dietrich, F. Gulminelli, M. Maggiore, and M. Oertel, 2023, Phys. Rev. D **108**, 122006.
Janquart, J., T. Baka, A. Samajdar, T. Dietrich, and C. Van Den Broeck, 2023, Mon. Not. R. Astron. Soc. **523**, 1699.
Jeong, K. S., L. McLerran, and S. Sen, 2020, Phys. Rev. C **101**, 035201.
Jiang, W. G., A. Ekström, C. Forssén, G. Hagen, G. R. Jansen, and T. Papenbrock, 2020, Phys. Rev. C **102**, 054301.
Johnson, A. D., K. Chatziioannou, and W. M. Farr, 2024, Phys. Rev. D **109**, 084015.
Johnson-McDaniel, N. K., and B. J. Owen, 2013, Phys. Rev. D **88**, 044004.
Just, O., S. Abbar, M.-R. Wu, I. Tamborra, H.-T. Janka, and F. Capozzi, 2022, Phys. Rev. D **105**, 083024.
Kalapotharakos, C., Z. Wadiasingh, A. K. Harding, and D. Kazanas, 2021, Astrophys. J. **907**, 63.
Kalogera, V., and G. Baym, 1996, Astrophys. J. Lett. **470**, L61.
Kaplan, D., and A. Nelson, 1986, Phys. Lett. B **175**, 57.
Kaplan, D. B., M. J. Savage, and M. B. Wise, 1998a, Phys. Lett. B **424**, 390.
Kaplan, D. B., M. J. Savage, and M. B. Wise, 1998b, Nucl. Phys. **B534**, 329.
Kashyap, R., *et al.*, 2022, Phys. Rev. D **105**, 103022.
Kedia, A., H. I. Kim, I.-S. Suh, and G. J. Mathews, 2022, Phys. Rev. D **106**, 103027.
Kedia, A., R. O'Shaughnessy, L. Wade, and A. Yelikar, 2024, arXiv:2405.17326.
Keller, J., K. Hebeler, and A. Schwenk, 2023, Phys. Rev. Lett. **130**, 072701.
Khadkikar, S., A. R. Raduta, M. Oertel, and A. Sedrakian, 2021, Phys. Rev. C **103**, 055811.
Kini, Y., T. Salmi, S. Vinciguerra, A. L. Watts, D. Choudhury, S. Bogdanov, J. Buchner, Z. Meisel, and V. Suleimanov, 2024, Mon. Not. R. Astron. Soc. **527**, 8118.
Kini, Y., T. Salmi, A. L. Watts, S. Vinciguerra, D. Choudhury, S. Fenne, S. Bogdanov, Z. Meisel, and V. Suleimanov, 2023, Mon. Not. R. Astron. Soc. **522**, 3389.
Kini, Y., *et al.*, 2024, Mon. Not. R. Astron. Soc. **535**, 1507.
Kiuchi, K., K. Kawaguchi, K. Kyutoku, Y. Sekiguchi, M. Shibata, and K. Taniguchi, 2017, Phys. Rev. D **96**, 084060.
Kiuchi, K., K. Kyutoku, M. Shibata, and K. Taniguchi, 2019, Astrophys. J. Lett. **876**, L31.
Kiuchi, K., A. Reboul-Salze, M. Shibata, and Y. Sekiguchi, 2024, Nat. Astron. **8**, 298.
Klevansky, S. P., 1992, Rev. Mod. Phys. **64**, 649.
Klüpfel, P., P. G. Reinhard, T. J. Bürvenich, and J. A. Maruhn, 2009, Phys. Rev. C **79**, 034310.
Knight, A., F. Foucart, M. D. Duez, M. Boyle, L. E. Kidder, H. P. Pfeiffer, and M. A. Scheel, 2024, Phys. Rev. D **110**, 023034.
Koehn, H., *et al.*, 2024, arXiv:2402.04172.
Kölsch, M., T. Dietrich, M. Ujevic, and B. Bruegmann, 2022, Phys. Rev. D **106**, 044026.
Komoltsev, O., and A. Kurkela, 2022, Phys. Rev. Lett. **128**, 202701.
Komoltsev, O., R. Somasundaram, T. Gorda, A. Kurkela, J. Margueron, and I. Tews, 2024, Phys. Rev. D **109**, 094030.
Konar, S., and D. Bhattacharya, 1997, Mon. Not. R. Astron. Soc. **284**, 311.
Köppel, S., L. Bovard, and L. Rezzolla, 2019, Astrophys. J. Lett. **872**, L16.
Kortelainen, M., *et al.*, 2014, Phys. Rev. C **89**, 054314.
Kramer, M., *et al.*, 2021, Phys. Rev. X **11**, 041050.
Krastev, P. G., B.-A. Li, and A. Worley, 2008, Phys. Lett. B **668**, 1.
Krüger, T., I. Tews, K. Hebeler, and A. Schwenk, 2013, Phys. Rev. C **88**, 025802.
Ku, M. J. H., A. T. Sommer, L. W. Cheuk, and M. W. Zwierlein, 2012, Science **335**, 563.
Kuan, H.-J., and K. D. Kokkotas, 2023, Phys. Rev. D **108**, 063026.
Kumar, P., M. Pürrer, and H. P. Pfeiffer, 2017, Phys. Rev. D **95**, 044039.
Kunert, N., P. T. H. Pang, I. Tews, M. W. Coughlin, and T. Dietrich, 2022, Phys. Rev. D **105**, L061301.
Kurkela, A., E. S. Fraga, J. Schaffner-Bielich, and A. Vuorinen, 2014, Astrophys. J. **789**, 127.
Kyutoku, K., M. Shibata, and K. Taniguchi, 2021, Living Rev. Relativity **24**, 5.
Lackey, B. D., K. Kyutoku, M. Shibata, P. R. Brady, and J. L. Friedman, 2014, Phys. Rev. D **89**, 043009.
Lai, D., 1994, Mon. Not. R. Astron. Soc. **270**, 611.
Landry, P., 2017, Phys. Rev. D **95**, 124058.
Landry, P., and R. Essick, 2019, Phys. Rev. D **99**, 084049.
Landry, P., R. Essick, and K. Chatziioannou, 2020, Phys. Rev. D **101**, 123007.
Landry, P., and E. Poisson, 2015, Phys. Rev. D **91**, 104018.
Landry, P., and J. S. Read, 2021, Astrophys. J. Lett. **921**, L25.
Lasky, P. D., B. Haskell, V. Ravi, E. J. Howell, and D. M. Coward, 2014, Phys. Rev. D **89**, 047302.
Lattimer, J. M., 2023, Particles **6**, 30.
Lattimer, J. M., and Y. Lim, 2013, Astrophys. J. **771**, 51.

Lattimer, J. M., and M. Prakash, 2001, Astrophys. J. **550**, 426.
Lattimer, J. M., and M. Prakash, 2004, Science **304**, 536.
Lattimer, J. M., and B. F. Schutz, 2005, Astrophys. J. **629**, 979.
Lee, T. D., and C. N. Yang, 1957, Phys. Rev. **105**, 1119.
Le Fèvre, A., Y. Leifels, W. Reisdorf, J. Aichelin, and C. Hartnack, 2016, Nucl. Phys. **A945**, 112.
Legred, I., K. Chatziioannou, R. Essick, S. Han, and P. Landry, 2021, Phys. Rev. D **104**, 063003.
Legred, I., K. Chatziioannou, R. Essick, and P. Landry, 2022, Phys. Rev. D **105**, 043016.
Legred, I., B. O. Sy-Garcia, K. Chatziioannou, and R. Essick, 2024, Phys. Rev. D **109**, 023020.
Lenz, W., 1929, Z. Phys. **56**, 778.
Li, B.-A., L.-W. Chen, and C. M. Ko, 2008, Phys. Rep. **464**, 113.
Li, B.-A., and D. Gross, 1993, Nucl. Phys. **A554**, 257.
Li, J. J., A. Sedrakian, and F. Weber, 2020, Phys. Lett. B **810**, 135812.
Li, X., and D. M. Siegel, 2021, Phys. Rev. Lett. **126**, 251101.
Liebling, S. L., C. Palenzuela, and L. Lehner, 2021, Classical Quantum Gravity **38**, 115007.
Lindblom, L., 1992, Astrophys. J. **398**, 569.
Lindblom, L., 2010, Phys. Rev. D **82**, 103011.
Lindblom, L., and N. M. Indik, 2012, Phys. Rev. D **86**, 084003.
Lindblom, L., and N. M. Indik, 2014, Phys. Rev. D **89**, 064003; **93**, 129903(E) (2016).
Littenberg, T. B., and N. J. Cornish, 2023, Phys. Rev. D **107**, 063004.
Lo, K. H., M. C. Miller, S. Bhattacharyya, and F. K. Lamb, 2013, Astrophys. J. **776**, 19.
Lockhart, W., S. E. Gralla, F. Özel, and D. Psaltis, 2019, Mon. Not. R. Astron. Soc. **490**, 1774.
Lonardoni, D., J. Carlson, S. Gandolfi, J. E. Lynn, K. E. Schmidt, A. Schwenk, and X. B. Wang, 2018, Phys. Rev. Lett. **120**, 122502.
Lonardoni, D., S. Gandolfi, J. E. Lynn, C. Petrie, J. Carlson, K. E. Schmidt, and A. Schwenk, 2018, Phys. Rev. C **97**, 044318.
Lonardoni, D., S. Gandolfi, and F. Pederiva, 2013, Phys. Rev. C **87**, 041303(R).
Lonardoni, D., F. Pederiva, and S. Gandolfi, 2014, Phys. Rev. C **89**, 014314.
Lonardoni, D., I. Tews, S. Gandolfi, and J. Carlson, 2020, Phys. Rev. Res. **2**, 022033(R).
Long, B., and C. J. Yang, 2012, Phys. Rev. C **85**, 034002.
Lorimer, D. R., 2008, Living Rev. Relativity **11**, 8.
Lynn, J. E., I. Tews, J. Carlson, S. Gandolfi, A. Gezerlis, K. E. Schmidt, and A. Schwenk, 2016, Phys. Rev. Lett. **116**, 062501.
Machleidt, R., 2001, Phys. Rev. C **63**, 024001.
Machleidt, R., and D. R. Entem, 2011, Phys. Rep. **503**, 1.
Mammei, J. M., C. J. Horowitz, J. Piekarewicz, B. T. Reed, and C. Sfienti, 2024, Annu. Rev. Nucl. Part. Sci. **74**, 321.
Manchester, R. N., G. B. Hobbs, A. Teoh, and M. Hobbs, 2005, Astron. J. **129**, 1993.
Marcucci, L. E., A. Kievsky, S. Rosati, R. Schiavilla, and M. Viviani, 2012, Phys. Rev. Lett. **108**, 052502.
Margalit, B., A. S. Jermyn, B. D. Metzger, L. F. Roberts, and E. Quataert, 2022, Astrophys. J. **939**, 51.
Margalit, B., and B. D. Metzger, 2017, Astrophys. J. Lett. **850**, L19.
Margueron, J., R. Hoffmann Casali, and F. Gulminelli, 2018, Phys. Rev. C **97**, 025805.
Maris, P., J. P. Vary, S. Gandolfi, J. Carlson, and S. C. Pieper, 2013, Phys. Rev. C **87**, 054318.
Martineau, T., F. Foucart, M. Scheel, M. Duez, L. Kidder, and H. Pfeiffer, 2024, arXiv:2405.06819.
Maselli, A., V. Cardoso, V. Ferrari, L. Gualtieri, and P. Pani, 2013, Phys. Rev. D **88**, 023007.
Matas, A., *et al.*, 2020, Phys. Rev. D **102**, 043023.
Mayer, M. G., 1964, Science **145**, 999.
McLerran, L., and S. Reddy, 2019, Phys. Rev. Lett. **122**, 122701.
Meisel, Z., 2018, Astrophys. J. **860**, 147.
Metzger, B. D., E. Quataert, and T. A. Thompson, 2008, Mon. Not. R. Astron. Soc. **385**, 1455.
Miles, M. T., *et al.*, 2025, Mon. Not. R. Astron. Soc. **536**, 1489.
Miller, M. C., 2021, in *Timing Neutron Stars: Pulsations, Oscillations and Explosions*, Astrophysics and Space Science Library Vol. 461, edited by T. M. Belloni, M. Méndez, and C. Zhang (Springer, New York), pp. 1–51.
Miller, M. C., and F. K. Lamb, 1998, Astrophys. J. Lett. **499**, L37.
Miller, M. C., and F. K. Lamb, 2015, Astrophys. J. **808**, 31.
Miller, M. C., *et al.*, 2019, Astrophys. J. Lett. **887**, L24.
Miller, M. C., *et al.*, 2021, Astrophys. J. Lett. **918**, L28.
Miyatsu, T., M.-K. Cheoun, K. Kim, and K. Saito, 2023, Phys. Lett. B **843**, 138013.
Mondal, C., B. K. Agrawal, M. Centelles, G. Colò, X. Roca-Maza, N. Paar, X. Viñas, S. K. Singh, and S. K. Patra, 2016, Phys. Rev. C **93**, 064303.
Morsink, S. M., D. A. Leahy, C. Cadeau, and J. Braga, 2007, Astrophys. J. **663**, 1244.
Most, E. R., L. J. Papenfort, V. Dexheimer, M. Hanauske, S. Schramm, H. Stöcker, and L. Rezzolla, 2019, Phys. Rev. Lett. **122**, 061101.
Murase, K., M. W. Toomey, K. Fang, F. Oikonomou, S. S. Kimura, K. Hotokezaka, K. Kashiyama, K. Ioka, and P. Mészáros, 2018, Astrophys. J. **854**, 60.
Nagar, A., P. Rettegno, R. Gamba, S. Albanesi, A. Albertini, and S. Bernuzzi, 2023, Phys. Rev. D **108**, 124018.
Nagar, A., *et al.*, 2018, Phys. Rev. D **98**, 104052.
Nakar, E., and T. Piran, 2011, Nature (London) **478**, 82.
Nättilä, J., M. C. Miller, A. W. Steiner, J. J. E. Kajava, V. F. Suleimanov, and J. Poutanen, 2017, Astron. Astrophys. **608**, A31.
Nättilä, J., and P. Pihajoki, 2018, Astron. Astrophys. **615**, A50.
Navratil, P., 2007, Few-Body Syst. **41**, 117.
Navratil, P., V. G. Gueorguiev, J. P. Vary, W. E. Ormand, and A. Nogga, 2007, Phys. Rev. Lett. **99**, 042501.
Nedora, V., S. Bernuzzi, D. Radice, B. Daszuta, A. Endrizzi, A. Perego, A. Prakash, M. Safarzadeh, F. Schianchi, and D. Logoteta, 2021, Astrophys. J. **906**, 98.
Nedora, V., F. Schianchi, S. Bernuzzi, D. Radice, B. Daszuta, A. Endrizzi, A. Perego, A. Prakash, and F. Zappa, 2022, Classical Quantum Gravity **39**, 015008.
Negele, J. W., and D. Vautherin, 1973, Nucl. Phys. **A207**, 298.
Newton, W. G., and J. R. Stone, 2009, Phys. Rev. C **79**, 055801.
Nitz, A. H., and Y.-F. Wang, 2022, Phys. Rev. D **106**, 023024.
O'Boyle, M. F., C. Markakis, N. Stergioulas, and J. S. Read, 2020, Phys. Rev. D **102**, 083027.
Oertel, M., M. Hempel, T. Klähn, and S. Typel, 2017, Rev. Mod. Phys. **89**, 015007.
Oliva, G. A., and F. Frutos-Alfaro, 2021, Mon. Not. R. Astron. Soc. **505**, 2870.
Ootes, L. S., D. Page, R. Wijnands, and N. Degenaar, 2016, Mon. Not. R. Astron. Soc. **461**, 4400.
Oppenheimer, J. R., and G. M. Volkoff, 1939, Phys. Rev. **55**, 374.
Oyamatsu, K., and K. Iida, 2007, Phys. Rev. C **75**, 015801.
Özel, F., 2006, Nature (London) **441**, 1115.
Paczynski, B., 1983, Astrophys. J. **267**, 315.
Page, D., J. M. Lattimer, M. Prakash, and A. W. Steiner, 2014, arXiv:1302.6626.
Page, D., M. Prakash, J. M. Lattimer, and A. W. Steiner, 2011, Phys. Rev. Lett. **106**, 081101.

Palenzuela, C., S. Liebling, and B. Miñano, 2022, Phys. Rev. D **105**, 103020.
Pandharipande, V. R., and R. B. Wiringa, 1979, Rev. Mod. Phys. **51**, 821.
Pang, P. T. H., T. Dietrich, I. Tews, and C. Van Den Broeck, 2020, Phys. Rev. Res. **2**, 033514.
Pang, P. T. H., *et al.*, 2023, Nat. Commun. **14**, 8352.
Pani, P., L. Gualtieri, and V. Ferrari, 2015, Phys. Rev. D **92**, 124003.
Pani, P., L. Gualtieri, A. Maselli, and V. Ferrari, 2015, Phys. Rev. D **92**, 024010.
Pannarale, F., E. Berti, K. Kyutoku, B. D. Lackey, and M. Shibata, 2015a, Phys. Rev. D **92**, 084050.
Pannarale, F., E. Berti, K. Kyutoku, B. D. Lackey, and M. Shibata, 2015b, Phys. Rev. D **92**, 081504.
Pannarale, F., E. Berti, K. Kyutoku, and M. Shibata, 2013, Phys. Rev. D **88**, 084011.
Papenfort, L. J., E. R. Most, S. Tootle, and L. Rezzolla, 2022, Mon. Not. R. Astron. Soc. **513**, 3646.
Papitto, A., *et al.*, 2025, Astron. Astrophys. **694**, A37.
Patruno, A., and A. L. Watts, 2021, in *Timing Neutron Stars: Pulsations, Oscillations and Explosions*, Astrophysics and Space Science Library Vol. 461, edited by T. M. Belloni, M. Méndez, and C. Zhang (Springer, New York), pp. 143–208.
Pavlov, G. G., and V. E. Zavlin, 1997, Astrophys. J. Lett. **490**, L91.
Pechenick, K. R., C. Ftaclas, and J. M. Cohen, 1983, Astrophys. J. **274**, 846.
Perego, A., D. Logoteta, D. Radice, S. Bernuzzi, R. Kashyap, A. Das, S. Padamata, and A. Prakash, 2022, Phys. Rev. Lett. **129**, 032701.
Peters, P. C., 1964, Phys. Rev. **136**, B1224.
Peters, P. C., and J. Mathews, 1963, Phys. Rev. **131**, 435.
Pétri, J., *et al.*, 2023, Astron. Astrophys. **680**, A93.
Philippov, A., and M. Kramer, 2022, Annu. Rev. Astron. Astrophys. **60**, 495.
Piarulli, M., L. Girlanda, R. Schiavilla, R. Navarro Pérez, J. E. Amaro, and E. Ruiz Arriola, 2015, Phys. Rev. C **91**, 024003.
Piarulli, M., and I. Tews, 2020, Front. Phys. **7**, 245.
Piekarewicz, J., and F. J. Fattoyev, 2019, Phys. Rev. C **99**, 045802.
Pieper, S. C., V. R. Pandharipande, R. B. Wiringa, and J. Carlson, 2001, Phys. Rev. C **64**, 014001.
Piro, A. L., B. Giacomazzo, and R. Perna, 2017, Astrophys. J. Lett. **844**, L19.
Pitkin, M., S. Reid, S. Rowan, and J. Hough, 2011, Living Rev. Relativity **14**, 5.
Pizzati, E., S. Sachdev, A. Gupta, and B. Sathyaprakash, 2022, Phys. Rev. D **105**, 104016.
Poisson, E., 1998, Phys. Rev. D **57**, 5287.
Poisson, E., and C. M. Will, 2014, *Gravity: Newtonian, Post-Newtonian, Relativistic* (Cambridge University Press, Cambridge, England).
Pons, J. A., F. M. Walter, J. M. Lattimer, M. Prakash, R. Neuhauser, and P.-h. An, 2002, Astrophys. J. **564**, 981.
Potekhin, A. Y., J. A. Pons, and D. Page, 2015, Space Sci. Rev. **191**, 239.
Poutanen, J., and M. Gierliński, 2003, Mon. Not. R. Astron. Soc. **343**, 1301.
Prakash, A., I. Gupta, M. Breschi, R. Kashyap, D. Radice, S. Bernuzzi, D. Logoteta, and B. S. Sathyaprakash, 2024, Phys. Rev. D **109**, 103008.
Prakash, A., D. Radice, D. Logoteta, A. Perego, V. Nedora, I. Bombaci, R. Kashyap, S. Bernuzzi, and A. Endrizzi, 2021, Phys. Rev. D **104**, 083029.
Pratten, G., P. Schmidt, and T. Hinderer, 2020, Nat. Commun. **11**, 2553.
Psaltis, D., and F. Özel, 2014, Astrophys. J. **792**, 87.
Psaltis, D., F. Özel, and D. Chakrabarty, 2014, Astrophys. J. **787**, 136.
Pudliner, B. S., V. R. Pandharipande, J. Carlson, S. C. Pieper, and R. B. Wiringa, 1997, Phys. Rev. C **56**, 1720.
Pudliner, B. S., V. R. Pandharipande, J. Carlson, and R. B. Wiringa, 1995, Phys. Rev. Lett. **74**, 4396.
Puecher, A., A. Samajdar, and T. Dietrich, 2023, Phys. Rev. D **108**, 023018.
Punturo, M., *et al.*, 2010a, Classical Quantum Gravity **27**, 194002.
Punturo, M., *et al.*, 2010b, Classical Quantum Gravity **27**, 084007.
Pürrer, M., and C.-J. Haster, 2020, Phys. Rev. Res. **2**, 023151.
Raaijmakers, G., S. K. Greif, K. Hebeler, T. Hinderer, S. Nissanke, A. Schwenk, T. E. Riley, A. L. Watts, J. M. Lattimer, and W. C. G. Ho, 2021, Astrophys. J. Lett. **918**, L29.
Raaijmakers, G., *et al.*, 2020, Astrophys. J. Lett. **893**, L21.
Racine, E., 2008, Phys. Rev. D **78**, 044021.
Radice, D., and S. Bernuzzi, 2023, Astrophys. J. **959**, 46.
Radice, D., S. Bernuzzi, and A. Perego, 2020, Annu. Rev. Nucl. Part. Sci. **70**, 95.
Radice, D., and L. Dai, 2019, Eur. Phys. J. A **55**, 50.
Radice, D., and I. Hawke, 2024, Living Rev. Comput. Astrophys. **10**, 1.
Radice, D., A. Perego, S. Bernuzzi, and B. Zhang, 2018, Mon. Not. R. Astron. Soc. **481**, 3670.
Radice, D., A. Perego, K. Hotokezaka, S. A. Fromm, S. Bernuzzi, and L. F. Roberts, 2018, Astrophys. J. **869**, 130.
Radice, D., A. Perego, F. Zappa, and S. Bernuzzi, 2018, Astrophys. J. Lett. **852**, L29.
Radice, D., and L. Rezzolla, 2011, Phys. Rev. D **84**, 024010.
Radice, D., L. Rezzolla, and F. Galeazzi, 2014, Mon. Not. R. Astron. Soc. **437**, L46.
Raithel, C. A., F. Özel, and D. Psaltis, 2016, Astrophys. J. **831**, 44.
Raithel, C., F. Özel, and D. Psaltis, 2018, Astrophys. J. Lett. **857**, L23.
Raithel, C. A., F. Özel, and D. Psaltis, 2019, Astrophys. J. **875**, 12.
Rajagopal, M., and R. W. Romani, 1996, Astrophys. J. **461**, 327.
Ravenhall, D. G., C. J. Pethick, and J. R. Wilson, 1983, Phys. Rev. Lett. **50**, 2066.
Read, J. S., 2023, Classical Quantum Gravity **40**, 135002.
Read, J. S., B. D. Lackey, B. J. Owen, and J. L. Friedman, 2009, Phys. Rev. D **79**, 124032.
Reardon, D. J., *et al.*, 2023, Astrophys. J. Lett. **951**, L6.
Reardon, D. J., *et al.*, 2024, Astrophys. J. Lett. **971**, L18.
Reed, B. T., F. J. Fattoyev, C. J. Horowitz, and J. Piekarewicz, 2021, Phys. Rev. Lett. **126**, 172503.
Reed, B. T., F. J. Fattoyev, C. J. Horowitz, and J. Piekarewicz, 2024, Phys. Rev. C **109**, 035803.
Reinert, P., H. Krebs, and E. Epelbaum, 2018, Eur. Phys. J. A **54**, 86.
Reinhard, P. G., 1989, Rep. Prog. Phys. **52**, 439.
Reinhard, P. G., and W. Nazarewicz, 2016, Phys. Rev. C **93**, 051303.
Reinhard, P.-G., X. Roca-Maza, and W. Nazarewicz, 2021, Phys. Rev. Lett. **127**, 232501.
Reitze, D., *et al.*, 2019, Bull. Am. Astron. Soc. **51**, 035, https://ui.adsabs.harvard.edu/abs/2019BAAS...51g..35R/abstract.
Relton, P., and V. Raymond, 2021, Phys. Rev. D **104**, 084039.
Remillard, R. A., *et al.*, 2022, Astron. J. **163**, 130.
Rezzolla, L., E. R. Most, and L. R. Weih, 2018, Astrophys. J. Lett. **852**, L25.
Rezzolla, L., and K. Takami, 2016, Phys. Rev. D **93**, 124051.
Rhoades, C. E., and R. Ruffini, 1974, Phys. Rev. Lett. **32**, 324.
Riles, K., 2023, Living Rev. Relativity **26**, 3.

Riley, T. E., D. Choudhury, T. Salmi, S. Vinciguerra, Y. Kini, B. Dorsman, A. L. Watts, D. Huppenkothen, and S. Guillot, 2023, J. Open Source Software **8**, 4977.
Riley, T. E., *et al.*, 2019, Astrophys. J. Lett. **887**, L21.
Riley, T. E., *et al.*, 2021, Astrophys. J. Lett. **918**, L27.
Roca-Maza, X., M. Brenna, G. Colò, M. Centelles, X. Viñas, B. K. Agrawal, N. Paar, D. Vretenar, and J. Piekarewicz, 2013, Phys. Rev. C **88**, 024316.
Roca-Maza, X., and J. Piekarewicz, 2008, Phys. Rev. C **78**, 025807.
Roca-Maza, X., X. Viñas, M. Centelles, B. K. Agrawal, G. Colò, N. Paar, J. Piekarewicz, and D. Vretenar, 2015, Phys. Rev. C **92**, 064304.
Romani, R. W., D. Kandel, A. V. Filippenko, T. G. Brink, and W. Zheng, 2022, Astrophys. J. Lett. **934**, L17.
Rose, H., N. Kunert, T. Dietrich, P. T. H. Pang, R. Smith, C. Van Den Broeck, S. Gandolfi, and I. Tews, 2023, Phys. Rev. C **108**, 025811.
Rowlinson, A., P. T. O'Brien, B. D. Metzger, N. R. Tanvir, and A. J. Levan, 2013, Mon. Not. R. Astron. Soc. **430**, 1061.
Rowlinson, A., *et al.*, 2024, Mon. Not. R. Astron. Soc. **534**, 2592.
Ruiz, M., S. L. Shapiro, and A. Tsokaros, 2018, Phys. Rev. D **97**, 021501.
Rutherford, N., *et al.*, 2024, Astrophys. J. Lett. **971**, L19.
Rutledge, R. E., L. Bildsten, E. F. Brown, G. G. Pavlov, and V. E. Zavlin, 1999, Astrophys. J. **514**, 945.
Sachdev, S., T. Regimbau, and B. S. Sathyaprakash, 2020, Phys. Rev. D **102**, 024051.
Salmi, T., B. Dorsman, A. L. Watts, A. Bobrikova, A. D. Marco, V. Loktev, A. Papitto, M. Pilia, J. Poutanen, and J. Rankin, 2025, Mon. Not. R. Astron. Soc. **538**, 2562.
Salmi, T., V. Loktev, K. Korsman, L. Baldini, S. S. Tsygankov, and J. Poutanen, 2021, Astron. Astrophys. **646**, A23.
Salmi, T., J. Nättilä, and J. Poutanen, 2018, Astron. Astrophys. **618**, A161.
Salmi, T., S. Vinciguerra, D. Choudhury, A. L. Watts, W. C. G. Ho, S. Guillot, Y. Kini, B. Dorsman, S. M. Morsink, and S. Bogdanov, 2023, Astrophys. J. **956**, 138.
Salmi, T., *et al.*, 2022, Astrophys. J. **941**, 150.
Salmi, T., *et al.*, 2024a, Astrophys. J. **974**, 294.
Salmi, T., *et al.*, 2024b, Astrophys. J. **976**, 58.
Samajdar, A., and T. Dietrich, 2018, Phys. Rev. D **98**, 124030.
Samajdar, A., and T. Dietrich, 2019, Phys. Rev. D **100**, 024046.
Samajdar, A., and T. Dietrich, 2020, Phys. Rev. D **101**, 124014.
Samajdar, A., J. Janquart, C. Van Den Broeck, and T. Dietrich, 2021, Phys. Rev. D **104**, 044003.
Sarin, N., T. A. Clarke, S. J. Magnall, P. D. Lasky, B. D. Metzger, E. Berger, and N. Sridhar, 2024, Astrophys. J. Lett. **973**, L20.
Sarin, N., C. M. B. Omand, B. Margalit, and D. I. Jones, 2022, Mon. Not. R. Astron. Soc. **516**, 4949.
Sarsa, A., S. Fantoni, K. E. Schmidt, and F. Pederiva, 2003, Phys. Rev. C **68**, 024308.
Schatz, H., A. Aprahamian, V. Barnard, L. Bildsten, A. Cumming, M. Ouellette, T. Rauscher, F.-K. Thielemann, and M. Wiescher, 2001, Phys. Rev. Lett. **86**, 3471.
Schmidt, K. E., and S. Fantoni, 1999, Phys. Lett. B **446**, 99.
Schmidt, P., and T. Hinderer, 2019, Phys. Rev. D **100**, 021501.
Schneider, A. S., C. J. Horowitz, J. Hughto, and D. K. Berry, 2013, Phys. Rev. C **88**, 065807.
Schroeder, G., B. Margalit, W.-f. Fong, B. D. Metzger, P. K. G. Williams, K. Paterson, K. D. Alexander, T. Laskar, A. V. Goyal, and E. Berger, 2020, Astrophys. J. **902**, 82.
Schwenk, A., G. E. Brown, and B. Friman, 2002, Nucl. Phys. **A703**, 745.
Schwenk, A., B. Friman, and G. E. Brown, 2003, Nucl. Phys. **A713**, 191.
Sedrakian, A., and J. W. Clark, 2019, Eur. Phys. J. A **55**, 167.
Sedrakian, A., F. Weber, and J. J. Li, 2020, Phys. Rev. D **102**, 041301 (R).
Sekiguchi, Y., K. Kiuchi, K. Kyutoku, and M. Shibata, 2011, Phys. Rev. Lett. **107**, 051102.
Shibata, M., 2016, *Numerical Relativity*, 100 Years of General Relativity Vol. 1 (World Scientific, Singapore).
Shibata, M., S. Fujibayashi, K. Hotokezaka, K. Kiuchi, K. Kyutoku, Y. Sekiguchi, and M. Tanaka, 2017, Phys. Rev. D **96**, 123012.
Shibata, M., and K. Hotokezaka, 2019, Annu. Rev. Nucl. Part. Sci. **69**, 41.
Shibata, M., K. Taniguchi, and K. Uryu, 2005, Phys. Rev. D **71**, 084021.
Shibata, M., E. Zhou, K. Kiuchi, and S. Fujibayashi, 2019, Phys. Rev. D **100**, 023015.
Silbar, R. R., and S. Reddy, 2004, Am. J. Phys. **72**, 892; **73**, 286(E) (2005).
Silva, H. O., G. Pappas, N. Yunes, and K. Yagi, 2021, Phys. Rev. D **103**, 063038.
Skyrme, T., 1958, Nucl. Phys. **9**, 615.
Smith, D. A., *et al.*, 2023, Astrophys. J. **958**, 191.
Somà, V., P. Navrátil, F. Raimondi, C. Barbieri, and T. Duguet, 2020, Phys. Rev. C **101**, 014318.
Somasundaram, R., C. Drischler, I. Tews, and J. Margueron, 2021, Phys. Rev. C **103**, 045803.
Somasundaram, R., J. E. Lynn, L. Huth, A. Schwenk, and I. Tews, 2024, Phys. Rev. C **109**, 034005.
Somasundaram, R., I. Tews, and J. Margueron, 2023, Phys. Rev. C **107**, L052801.
Song, H. Q., M. Baldo, G. Giansiracusa, and U. Lombardo, 1998, Phys. Rev. Lett. **81**, 1584.
Sorensen, A., *et al.*, 2024, Prog. Part. Nucl. Phys. **134**, 104080.
Sotani, H., K. Iida, and K. Oyamatsu, 2019, Mon. Not. R. Astron. Soc. **489**, 3022.
Soultanis, T., A. Bauswein, and N. Stergioulas, 2022, Phys. Rev. D **105**, 043020.
Stairs, I. H., 2003, Living Rev. Relativity **6**, 5.
Steiner, A. W., 2006, Phys. Rev. C **74**, 045808.
Steiner, A. W., 2012, Phys. Rev. C **85**, 055804.
Steiner, A. W., and S. Gandolfi, 2012, Phys. Rev. Lett. **108**, 081102.
Steiner, A. W., S. Gandolfi, F. J. Fattoyev, and W. G. Newton, 2015, Phys. Rev. C **91**, 015804.
Steiner, A. W., C. O. Heinke, S. Bogdanov, C. Li, W. C. G. Ho, A. Bahramian, and S. Han, 2018, Mon. Not. R. Astron. Soc. **476**, 421.
Steiner, A. W., J. M. Lattimer, and E. F. Brown, 2010, Astrophys. J. **722**, 33.
Steiner, A. W., M. Prakash, J. M. Lattimer, and P. J. Ellis, 2005, Phys. Rep. **411**, 325.
Steinhoff, J., T. Hinderer, A. Buonanno, and A. Taracchini, 2016, Phys. Rev. D **94**, 104028.
Steinhoff, J., T. Hinderer, T. Dietrich, and F. Foucart, 2021, Phys. Rev. Res. **3**, 033129.
Stergioulas, N., and J. L. Friedman, 1995, Astrophys. J. **444**, 306.
Stoks, V. G. J., R. A. M. Klomp, M. C. M. Rentmeester, and J. J. de Swart, 1993, Phys. Rev. C **48**, 792.
Stoks, V. G. J., R. A. M. Klomp, C. P. F. Terheggen, and J. J. de Swart, 1994, Phys. Rev. C **49**, 2950.
Strohmayer, T. E., 1992, Astrophys. J. **388**, 138.
Suleiman, L., M. Fortin, J. L. Zdunik, and P. Haensel, 2021, Phys. Rev. C **104**, 015801.

Suleiman, L., J.-L. Zdunik, and P. Haensel, 2024, Astron. Astrophys. **690**, A301.
Suleimanov, V. F., J. Poutanen, and K. Werner, 2020, Astron. Astrophys. **639**, A33.
Tamii, A., *et al.*, 2011, Phys. Rev. Lett. **107**, 062502.
Tan, H., J. Noronha-Hostler, and N. Yunes, 2020, Phys. Rev. Lett. **125**, 261104.
Tauris, T. M., *et al.*, 2017, Astrophys. J. **846**, 170.
Taylor, J. H., R. D. Blandford, A. Hewish, A. G. Lyne, and L. Mestel, 1992, Phil. Trans. R. Soc. A **341**, 117.
Tews, I., J. Carlson, S. Gandolfi, and S. Reddy, 2018, Astrophys. J. **860**, 149.
Tews, I., Z. Davoudi, A. Ekström, J. D. Holt, and J. E. Lynn, 2020, J. Phys. G **47**, 103001.
Tews, I., T. Krüger, K. Hebeler, and A. Schwenk, 2013, Phys. Rev. Lett. **110**, 032504.
Tews, I., J. M. Lattimer, A. Ohnishi, and E. E. Kolomeitsev, 2017, Astrophys. J. **848**, 105.
Tews, I., P. T. H. Pang, T. Dietrich, M. W. Coughlin, S. Antier, M. Bulla, J. Heinzel, and L. Issa, 2021, Astrophys. J. Lett. **908**, L1.
Tews, I., R. Somasundaram, D. Lonardoni, H. Göttling, R. Seutin, J. Carlson, S. Gandolfi, K. Hebeler, and A. Schwenk, 2024, arXiv:2407.08979.
Thiel, M., C. Sfienti, J. Piekarewicz, C. J. Horowitz, and M. Vanderhaeghen, 2019, J. Phys. G **46**, 093003.
Thompson, J. E., E. Fauchon-Jones, S. Khan, E. Nitoglia, F. Pannarale, T. Dietrich, and M. Hannam, 2020, Phys. Rev. D **101**, 124059.
Thorne, K. S., 1977, Astrophys. J. **212**, 825.
Thorne, K. S., 1980, Rev. Mod. Phys. **52**, 299.
Thorne, K. S., 1998, Phys. Rev. D **58**, 124031.
Thorne, K. S., and A. Campolattaro, 1967, Astrophys. J. **149**, 591.
Tichy, W., L. Ji, A. Adhikari, A. Rashti, and M. Pirog, 2023, Classical Quantum Gravity **40**, 025004.
Tolman, R. C., 1939, Phys. Rev. **55**, 364.
Tolos, L., and L. Fabbietti, 2020, Prog. Part. Nucl. Phys. **112**, 103770.
Tootle, S. D., L. J. Papenfort, E. R. Most, and L. Rezzolla, 2021, Astrophys. J. Lett. **922**, L19.
Torres-Rivas, A., K. Chatziioannou, A. Bauswein, and J. A. Clark, 2019, Phys. Rev. D **99**, 044014.
Tringali, M. C., A. Puecher, C. Lazzaro, R. Ciolfi, M. Drago, B. Giacomazzo, G. Vedovato, and G. A. Prodi, 2023, Classical Quantum Gravity **40**, 225008.
Tsang, C. Y., M. B. Tsang, W. G. Lynch, R. Kumar, and C. J. Horowitz, 2024, Nat. Astron. **8**, 328.
Tsang, K. W., T. Dietrich, and C. Van Den Broeck, 2019, Phys. Rev. D **100**, 044047.
Tsang, M. B., Y. Zhang, P. Danielewicz, M. Famiano, Z. Li, W. G. Lynch, and A. W. Steiner, 2009, Phys. Rev. Lett. **102**, 122701.
Typel, S., and B. A. Brown, 2001, Phys. Rev. C **64**, 027302.
van der Wateren, E., *et al.*, 2023, Astron. Astrophys. **669**, A160.
van Kolck, U., 1994, Phys. Rev. C **49**, 2932.
Vidaña, I., J. Margueron, and H.-J. Schulze, 2024, Universe **10**, 226.
Vidaña, I., A. Polls, A. Ramos, M. Hjorth-Jensen, and V. G. J. Stoks, 2000, Phys. Rev. C **61**, 025802.
Viñas, X., M. Centelles, X. Roca-Maza, and M. Warda, 2014, Eur. Phys. J. A **50**, 27.
Vincent, F. H., *et al.*, 2018, Astrophys. J. **855**, 116.
Vinciguerra, S., T. Salmi, A. L. Watts, D. Choudhury, Y. Kini, and T. E. Riley, 2023, Astrophys. J. **959**, 55.
Vinciguerra, S., *et al.*, 2024, Astrophys. J. **961**, 62.
Vines, J., E. E. Flanagan, and T. Hinderer, 2011, Phys. Rev. D **83**, 084051.
Walter, F. M., S. J. Wolk, and R. Neuhäuser, 1996, Nature (London) **379**, 233.
Wang, H., P. Beniamini, and D. Giannios, 2024, Mon. Not. R. Astron. Soc. **527**, 5166.
Wang, Y., B. Zhang, and Z. Zhu, 2024, Mon. Not. R. Astron. Soc. **528**, 3705.
Watanabe, G., K. Iida, and K. Sato, 2000, Nucl. Phys. **A676**, 455; **A726**, 357(E) (2003).
Watanabe, G., H. Sonoda, T. Maruyama, K. Sato, K. Yasuoka, and T. Ebisuzaki, 2009, Phys. Rev. Lett. **103**, 121101.
Watts, A. L., 2012, Annu. Rev. Astron. Astrophys. **50**, 609.
Watts, A. L., *et al.*, 2016, Rev. Mod. Phys. **88**, 021001.
Webb, N. A., and D. Barret, 2007, Astrophys. J. **671**, 727.
Weinberg, S., 1990, Phys. Lett. B **251**, 288.
Weinberg, S., 1991, Nucl. Phys. **B363**, 3.
Wellenhofer, C., J. W. Holt, and N. Kaiser, 2015, Phys. Rev. C **92**, 015801.
Wigner, E., and F. Seitz, 1933, Phys. Rev. **43**, 804.
Wijngaarden, M., K. Chatziioannou, A. Bauswein, J. A. Clark, and N. J. Cornish, 2022, Phys. Rev. D **105**, 104019.
Wiringa, R. B., V. Fiks, and A. Fabrocini, 1988, Phys. Rev. C **38**, 1010.
Wiringa, R. B., and S. C. Pieper, 2002, Phys. Rev. Lett. **89**, 182501.
Wiringa, R. B., V. G. J. Stoks, and R. Schiavilla, 1995, Phys. Rev. C **51**, 38.
Wolff, M. T., *et al.*, 2021, Astrophys. J. Lett. **918**, L26.
Xu, H., *et al.*, 2023, Res. Astron. Astrophys. **23**, 075024.
Xu, J., *et al.*, 2016, Phys. Rev. C **93**, 044609.
Yagi, K., and N. Yunes, 2013, Phys. Rev. D **88**, 023009.
Yagi, K., and N. Yunes, 2016, Classical Quantum Gravity **33**, 13LT01.
Yagi, K., and N. Yunes, 2017, Phys. Rep. **681**, 1.
Yang, H., W. E. East, and L. Lehner, 2018, Astrophys. J. **856**, 110; **870**, 139(E) (2019).
Youngblood, D. H., H. L. Clark, and Y. W. Lui, 1999, Phys. Rev. Lett. **82**, 691.
Yuan, Y., X.-L. Fan, and H.-J. Lü, 2023, Mon. Not. R. Astron. Soc. **522**, 4294.
Zappa, F., S. Bernuzzi, D. Radice, and A. Perego, 2023, Mon. Not. R. Astron. Soc. **520**, 1481.
Zappa, F., S. Bernuzzi, D. Radice, A. Perego, and T. Dietrich, 2018, Phys. Rev. Lett. **120**, 111101.
Zavlin, V. E., G. G. Pavlov, and Y. A. Shibanov, 1996, Astron. Astrophys. **315**, 141, https://ui.adsabs.harvard.edu/abs/1996A%26A...315..141Z/abstract.
Zhang, B., and P. Meszaros, 2001, Astrophys. J. Lett. **552**, L35.
Zhang, Y., and Z. Li, 2006, Phys. Rev. C **74**, 014602.
Zhao, T., and J. M. Lattimer, 2018, Phys. Rev. D **98**, 063020.
Zic, A., *et al.*, 2023, Publ. Astron. Soc. Aust. **40**, e049.